IJCOE
INTERNATIONAL JOURNAL OF
COASTAL, OFFSHORE AND
ENVIRONMENTAL ENGINEERING

volume 9| Issue 4| Nov 2024

www.ijcoe.org

International Journal of Coastal, Offshore and Environmental Engineering (IJCOE) Vol. 9| Issue 4| Nov 2024

International Journal of
Coastal, Offshore
Environmental
Engineering
Since 2015
ISSN: 2980-8731 (online)

Volume 9 | Issue 4| Nov 2024
IJCOE
Editor-in-Chief: Prof. Hamid S.Bahai

International Journal of Coastal, Offshore & Environmental Engineering
Since 2015
ISSN: 2980-8721 (online)

In The Name of God

Message from the Editor-in-Chief

The IJCOE journal office was established in 2015,and its first issue was published in 2016. TheIJCOE covers a wide range of research in thefields of oceanography & ocean technology, aswell as marine industries & marine engineering.The editorial board of IJCOE consists of nearly130 of the greatest scientists and researchersfrom over 30 countries worldwide, and thejournal's review board comprises 1,000 membersfrom all five continents. The membership andapplication process for joining the editorial andreview boards of this journal is ongoing. IJCOE isa research-academic quarterly journal that haspublication and distribution permissions fromthe Press Organization and permission topublish scientific-research articles from theMinistry of Science, Research, and Technology(MSRT) with an "A" rating. It also holds a "Q1"rating from the ISC institute with an impactfactor (IF) of approximately 0.43 and isconsidered a "core journal" (prestigious andoutstanding journal). IJCOE is an open-accessjournal and allows the download and receipt ofaccepted articles in full text for free. It respectsand adheres to copyright and COPE regulations.The journal's office operates 24/7, providingservices to researchers. In addition to publishinga regular quarterly journal, IJCOE has 16 specialissues on specific topics in preparation. It alsoprovides conditions for publishing specializedbooks, references, and handbooks. Moreover, itis ready to cooperate with the secretariats ofreputable international conferences to publishtheir selected and outstanding articles. IJCOEevaluates, appraises, and publishes books,articles, and the scientific achievements andfindings of esteemed researchers and scientistsworldwide who are innovating and conductingin-depth research in the "important and strategicfield of the maritime technology & Oceanengineering." It welcomes any form of jointcooperation with universities, research institutes,and related research centers at the national,regional, and international levels, and extends ahand for collaboration.

Classification of Editorial Board in IJCOE

Editor-in-Chief

Director-in-Chief

Deputy Editor

Executive Managers

English Text Editor

Technical Editor

International Editorial Board

National Editorial Board

Editorial Board Associate

Editorial Board Assistant

Guest Editorial Board

Advisory Board

Administrative Coordinator

Honorary Board Member

Methodology Advisor

Author Benefits

- Open Access
- Rapid Publication
- Thorough Peer-Review
- No Copyright Constraints
- Coverage by Leading Indexing Services
- Discounts On Article Processing Charges (APC)
- No Space Constraints, No restriction on the maximum length of the papers, number of figures or colors

INTERNATIONAL JOURNAL OF IJCOE COASTAL, OFFSHORE & ENVIRONMENTAL ENGINEERING

Aims of IJCOE

Hydrodynamics

Marine equipment

Structural mechanics

Ocean environmental predictions

Stochastic calculations Experimental

Automatic Control of Marine Systems

Scope of IJCOE

Marine Hazards

Ocean Acoustics

Naval Architecture

Ocean Engineering

Coastal Engineering

Marine Meteorology

Marine Earth Sciences

Underwater Technology

Marine Renewable Energy

Polar & Arctic Engineering

Marine Renewable Energy

Marine Geography & Geodesy

Marine Environmental Engineering

Automatic Control of Marine Systems

Hydro Physics & Physical Oceanography

Type of papers

- Case Studies
- Book Reviews
- Review Article
- Letters to the Editor
- Methodology Papers
- Editorials and Commentaries
- Response or Rejoinder Papers
- Perspective or Opinion Papers
- Conceptual or Theoretical Papers
- Meta-Analysis and Systematic Reviews
- Short Communications or Brief Reports
- Research Articles (Original Research Papers)

Scientific Research Journal

Ministry of Science, Research And Technology (MSRT)

Jurnal Ranking 2023: A

Ministry Of Science, Research And Technology (ISC)

Citation Impact 2022: 0.429

Quartile 2022 : Q1

Core Collection

IJCOE is a Member of

Cantact Us

Office 1 | Research Institute of Meteorology and Atmospheric Science

Address | Tehran, Shahid Kharrazi Highway, Pajoohesh Blvd, Research Institute of Meteorology and Atmospheric Science, Sand and Dust Storm International Research Center (SDS-IRC), No. 13, 1st floor.

Phone | +982144787652

Postal code | 13611-14977

website | www.rimac.ac.ir

Office 2 | Iranian National Institute for Oceanography and Atmospheric Science

Address | Tehran, Dr. Fatemi Gharbi St., Shahid Etemadzade St., No. 3, third floor.

Phone | +982166944873

Postal code | 13389 – 14118

website | www.inio.ac.ir

Email | Info@ijcoe.org

Website | www.ijcoe.org

Follow Us

www.ijcoe.org

INTERNATIONAL JOURNAL OF IJCOE COASTAL, OFFSHORE & ENVIRONMENTAL ENGINEERING

Volume & Issue:

Volume 9, Issue 4, November 2024

Number of Articles: 6

Content

INTERNATIONAL JOURNAL OF
COASTAL, OFFSHORE & ENVIRONMENTAL ENGINEERING IJCOE Vol.9/No. 4/Autumn 2024 (1-19)

Available online at: www. Ijcoe.org

Study of Adsorption of Micro Plastics (MPs) using PSF/MIL-100(Fe) Membrane in 3D printed column from seawater

Reza Alizadeh[1*] , Hamed Ghorbani [2], Arash Alizadeh[3]

[1] Assistant Professor, Civil Engineering Department, Faculty of Engineering, Qom University of Technology, Qom, Iran, alizadeh_environment@yahoo.com*

[2] Assistant Professor, Department of Chemical and materials and polymer Engineering, Buein Zahra Technical University, Buein Zahra, Qazvin, Iran, hamed.ghorbani@bzte.ac.ir

[3] School of Chemical Engineering, College of Engineering, University of Tehran, Tehran, Iran, arash.alizadeh@ut.ac.ir

ARTICLE INFO

Article History:
Received: 1 Aug 2024
Accepted: 9 Oct 2024

Keywords:
Nanocomposite
Metal-organic framework
Micro plastics
Removal
Adsorbent

ABSTRACT

In this research, Micro Plastics were separated using a combination of an PSF/MIL-100(Fe) created by layering the polymers such as Polysulfone onto the metal organometallic compound. The effect of MIL-100 (Fe) incorporation on PSF matrix was studied, including the porosity, pore size, morphology, separation performance. In this regard, thirty experiments were designed and implemented using the surface response method and central design software. More recently, polymers such as poly sulfon (PSF), polyamide, poly vinylidene fluoride, and polyether sulfone have become the leading raw materials for the fabrication of membranes. Factors influencing absorption include the amount of absorbent, concentration of MPs, and the duration of exposure, each assessed at three different levels. In each experiment, a quantity of absorbent was placed in ten milliliters of water mixed with MPs, and the amount of MPs removal was measured. Meanwhile, there is a need for more research to investigate the long-term stability of MOFs in aqueous environments and developing efficient regeneration methods for their repeated use. The prepared absorbent had a specific surface area of 1000 g/m2**.** Instrumental methods were used to investigate the physical properties of the prepared MOF nanoparticles. The test conditions included contact times of 1-5 minutes, absorbent amounts ranging from 1-25 mg, MPs concentrations of 1-25 mg/L. The 100% removal of MPs was achieved using 10 mg of nano absorbent for a contact time of 5 minutes. In this research, The fabricated PSF/MIL-100(Fe) composite membrane displayed excellent rejection of MPs

1. Introduction

In 2021 year, 390.7 million tons of plastics are manufactured from which, about 13 million tons were entered into rivers. Consumption and Production of plastics has increased dramatically and reached 0.3 billion tons/year, of which half is for single-use. It is estimated that over Five Gt of plastic waste is globally scattered in the environment. By the end of 2025, it is estimated that 250 million tons of plastics will be released to waters (Figure 1). There are 15,000 variants with 25,000 trade names for plastics. They are obtained from coal and oil and consist of one or more long chains of carbon as their molecular structure which is bonded with elements such as oxygen, nitrogen, hydrogen, chlorine and sulfur. Polystyrene (PS), High-density polyethylene, polyvinyl chloride, polypropylene and polyether sulfone are the widest use plastics, accounting for about 75% of plastics production. They are mainly used in packaging, electronic Industries, automotive manufacturing and construction. In the environment, factors such as physical abrasion, sunlight, weathering, and biological degradation can fragment plastics to smaller particles, in part into hazardous Micro Plastics are identified as plastic fragments with a size of several millimeters, typically less than five mm . Micro Plastics has a range of sizes and variety in shapes with different compositions and include aromatic or aliphatic structures with various functional groups and may contain dyes, blends and copolymers. Wind Energy transfers Micro Plastics for hundreds miles and they can also be transported over great distances via ocean currents. They can also be carried out from land into waterways through rainfall and sink in oceans. Besides industries which manufacture them, direct throwing out disposable plastics, laundering of synthetic clothes, microbeads from cosmetic products, scrape of automobile tires, and fragmentation of large particles of plastics are another most important sources of entrance of MPs to the aquatic streams. It is estimated that quantity of MPs which enters into seawater is between 4.8-12.7 million tons, while already around 14 million tons MPs are deposited on the floor of the oceans. Because of the floating character of plastic particles, they can easily be spread around the water, passing them to gather on seashores, where they may remain for millions of years. MPs have been found everywhere, from the earth's atmosphere to the sediments of deep seas, from ice in the poles to all ecosystems. Franeker, et al. studied the stomachs of 1295 of seabirds and found that 95% of them contained an average of 34.5 ± 2.5 pieces of MPs. Recently, it has been shown that MPs can be absorbed by the roots of plants and translocated to aerial tissues and can be accumulated in their organs . They can also remain in the terrestrial and sea plants. It is proved that MPs can even have a significant effect on microorganisms during fermentation of biomass. Due to their high ratio of surface area to mass, MPs can adsorb bacteria and pollutants and toxins such as pharmaceuticals, heavy metals, personal care products and so on which can be ingested by aquatic animals and finally be consumed by humans posing an unpredictable health risk. MPs can also enter into the human bodies through contaminated drinks and breathing as a result, MPs particles have been seen

in human blood and stool. Recently, MPs have been declared as contaminants of emerging concern and present a significant risk to human health as endocrine disruptors. Consequently, MPs can cause cancer, malformation in humans, impaired reproductive activity, and reduce immune response. MPs fibers in the respiratory system can cause tumors in the lung and azo dyes used for polymers coloring may cause endocrine disruption, dermatitis, and hormone dysregulation. It should be mentioned that toxicity of MPs is not only because of their own nature but also is due to the various additives and plasticizers that are added to them during their manufacturing. Khan & Jia recently summarized the impact of MPs over ecosystems and human health. The European Union started a strategy on controlling release of MPs into waterways to reduce their pollution in water resources. To keep all of the sources of water safe, there is a need to remove MPs as a major water pollutant, which is also a major concern globally. one of the most important ways that MPs can enter the human body is through drinking contaminated water. Wastewater treatment plants (WWTPs), cannot completely remove MPs. It has been shown that even after treatment, about 73.8% of MPs can be accumulated in the sludge of the WWTPs, so the effluent released from these plants contains substantial quantities of MPs. If these effluents mix with freshwater, MPs enter the drinking water supply chain. Another source for MPs entering the water distribution systems is via the system itself, since many parts of water treatment plants and water distribution and pipeline systems are made up of polymers such as PP, HDPE and PVC. MPs in the water resources are mainly found in the forms of Fibers, fragments, pellets, foams and films **(**Figure2**)**. The obvious harmful effects of MPs on the environment, human health, and ecology, led scientists to investigate ways to remove them from aquatic media During treatment in WWTPs, water passes through three levels of primary, secondary, and tertiary treatments. Sometimes, there is also an initial step for removal of large floating objects. Throughout primary treatment, insoluble solids from the wastewater physically settle down. At this stage, 35–59% of MPs can be removed by their trapping in solid flocs and screening the light floating MPs. This process leads to a 37% increase in small particles (0.1mm). The removal efficiency in water and WWTPs is calculated based on the MPs concentration in the influent and effluent, i.e. The number of MPs present per liter of the liquid. By using the attached growth or suspended growth system, during the secondary biological treatment stage, targets degradation of the biological content of the wastewater happens. At this stage, 50–98% of MPs can be removed. The main mechanism of MPs separation at this stage is the skimming and settling of the entrapped MPs by gravity. It is proven that this treatment removes fragments more effectively than micro fibers. Tertiary advanced stage of the treatment is the final stage in which chemical disinfection, ozonation, ultra/micro/nano-filtration, reverse osmosis are utilized. For tertiary treatment, different mechanisms are suggested for the removal of MPs. Efficiency of this stage for the removal of MPs is highly dependent. Visually distinguishing micro plastic particles from natural particles under a light microscope is difficult and may require confirmation using more precise instrumentation. The study pointed out that MPs

can interact with other pollutants in water, like heavy metals and organic compounds. This interaction may change the behavior and toxicity of MPs, making their removal from water even more crucial. [1].

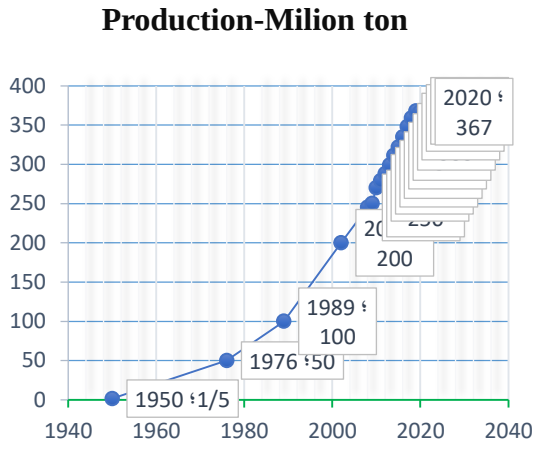

Figure 1-Production of MPS in World (Statista, 2022)

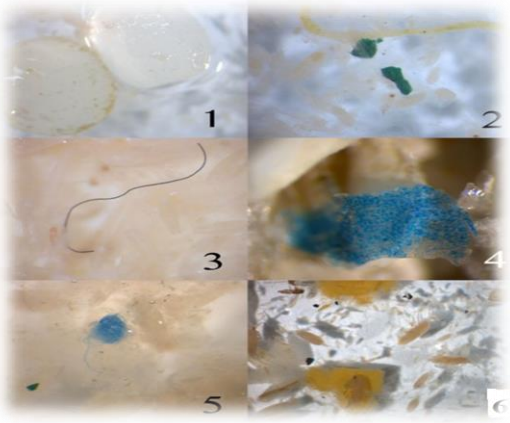

Figure 2-. 1. bullet 2. Pieces 3. Fiber 4. Film 5. threads and strings 6. sponge/ foam (Frias et al., 2018).

In the Table 1 shown the various shapes of MPs in Some seawater and marine environments of Iran

Table1- Summary of the various shapes of MPs in water and marine environments of Iran

In the Figures below, the common schematic processes of removing MPs from the water environment are shown, including: oxidation, hydrolysis, organic metal structures, photo catalyst, phase change, photo electrochemical.

In Figure 3 shown Oxidation mediated MPs

Result	Polymeric nature	Microplastic type	Date	Place
All 51 studied samples were contaminated with micro plastics, and a total of 28 micro plastics were identified (Ghatavi et al.)	-	86% fiber 11% piece 3% bullet	1398	**sea Oman**
All 50 fish samples contained microplastics (Kord and Naji).	PE PET	55% fiber 26% piece 1% film 18% bullet	1398	**Chabahar Gulf**
2169 micro plastic particles from 5 stations The investigated item was identified (Maghsodian *et al*., 2022)	ps	60% fiber 27% piece 11% film 2% bullet	1400	**Persian Gulf**
899 of the 15 investigated stations Micro plastic was detected (Kor & Mehdinia, 2020).	PE PP	44.1 % fiber 29 % piece 12.2 % bullets 14.7 % movie	1399	**Persian Gulf**
Of the 50 samples examined, an average of 218 particles per liter of micro plastic con.had (Hosseini *et al*., 2020l)	PE PET PA	42.54 % fiber 28.66 %piece 10.57 % bullets 18.24 % film	1399	**sea Oman**

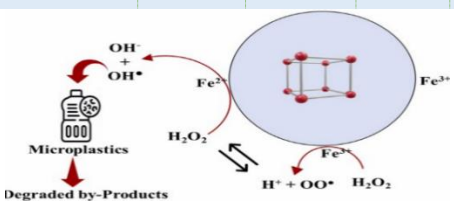

Figure 3-Oxidation mediated micro plastics degradation utilising MOF-based Fenton

In Figure 4 shown Hydrolytic mediated MPs degradation by MOF, results in cleavage of polymeric chain.

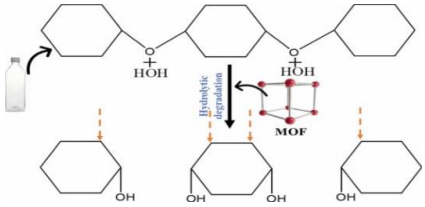

Figure 4- Hydrolytic mediated micro plastics degradation by MOF

In Figure 5 shown MOF based biommic king of enzyme to degrade phenolic compounds, here MOF shows the enzyme like activity which mimics the action mechanism for phenolic compounds (which is some of by products produced during MPs degradation).

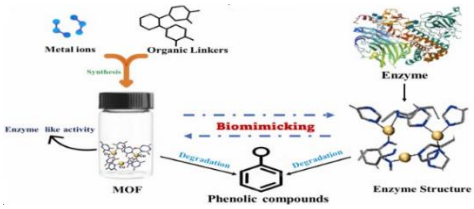

Figure 5- MOF based bio mimicking of enzyme to degrade phenolic compounds

In Figure 6 shown Photocatalytic degradation mechanism of MPs by MOF

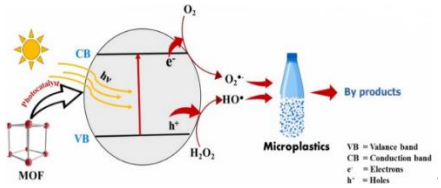

Figure 6- Photocatalytic degradation mechanism of micro plastics by MOF

In Figure 7 Phase transformation based MPs degradation. Here, MOF and their phase transformed structure degrades polymeric MPs more disposable monomeric units, under specific high temperature, pressure and time duration.

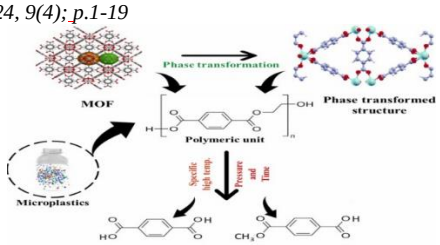

Figure 7- Phase transformation based micro plastics degradation

In Figure 8 Photo electrochemical degradation mechanism for MPs. Holes (h^+) and electrons actively take part to generate photo anode with syn chronisation with electrochemical platform and perform

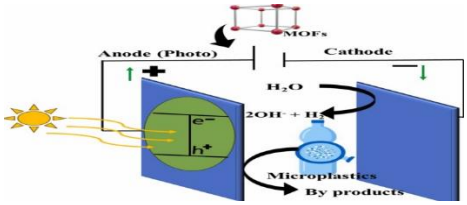

Figure 8- Photo electrochemical degradation mechanism for micro plastics

2. Materials and methods

2-1. Material

Poly sulfone (PSF or AMSA=Amino Methyl Sulfonic Acid)in the form of granules was used as a polymer matrix, it was purchased from Sigma Aldrich company, 99% pure, transparent and with a molecular mass of 22//000 g/mol., poly vinyl pyrrolidone (average Mw 10000), *N*-methyl-2-pyrrolidone (NMP), micro plastic particles such as polyvinyl chloride(PVC, high molecular weight(Mw = 48,000 g mol^{-1}))and poly ethylene(PE, ultra-high molecular weight (Mw = 3,000,000–6,000,000 g mol^{-1})) was purchased from Sigma Aldrich, South Korea. and Ethanol were procured from Daejung Chemicals Ltd. Hydro chloric acid (HCl,37.0%), methanol (≥99.8%), N,N-dimethyl formamide (99.5%) and acetone(≥99.8%) were acquired from

Scharlau.1,3,5-benzenetricarboxylic acid (H_3BTC, >98%) were obtained from ACROS organics., poly vinylidene difluoride (MW ~180,000), sodium hydroxide (NaOH, ≥ 97.0%) were obtained from Aldrich., Fe(III) chloride hexa hydrate($FeCl_3 \cdot 6H_2O$,>97%) was acquired from Panreac. And ultrapure water (18.2 MΩ cm). mixer speed of 700 rpm, 1.1 μm PS microspheres.

Characterizations of Micro Plastics

The crystallinity of the micro plastics plays an essential role in the adsorption of pollutants. intense peaks of polyethylene MPs, including 21.5 and 24.1° at 2θ [37]. Two diffraction peaks of PVC were present at 18 and 24.3° at 2θ. Surface morphology of the PE and PVC MPs Specifically, Both PE and PVC MPs had uneven shapes with dimensions of about 44.5 μm and 142.6 μm, respectively. In this research preparation of a novel adsorbent by grafting PSF to coordinatively unsaturated iron sites of MIL-100-Fe, an iron-benzene tri carboxylate MOF characterized by its low cost, great porosity and water stability, that was prepared in 10 min by microwave-assisted method. The developed sulfonic-functionalized MIL-100-Fe was used for the removal of MPs. After batch experiments, the functionalized MIL-100 material was immobilized in a 3D column by a simple and fast coating method and used for the extraction of MPs. It is proved that MPs removal can be reached to 100%. Nanomaterials such as MOFs are known as excellent adsorbents due to their huge surface areas, ease of synthesis and rapid functionalization, and high association with various pollutants. It should be noted that the adsorption capacity of adsorbents is highly affected by the shape and size of MPs. Due to their smooth and edge-less surfaces, microbeads are adsorbed to a lesser extent compared to the MPs with irregular shapes. As mentioned earlier, MOFs are under increasing attention in water remediation due to their successful applicability [38]. These materials are classified as highly ordered crystalline metal clusters with high porosity (> 90%) which are composed of metal–oxide clusters and organic linkers. They have extremely large surface area (10,000 m2/g), which make them suitable for a wide variety of applications, including MPs adsorption. By changing metal oxides and organic linkers, it is possible to control the pore size, volume, and functionality of MOFs to adjust them for any designable applications. Also, the characteristics of MOFs mainly depend on the nature of the selected inorganic and organic nodes and ligands and their conectivity. MOFs are also characterized by their ease of synthesis and modification. They showed high performance in recycling and large-quantity filtration experiments as well. The functional groups of MOFs can form hydrogen bonding or van der Waals interaction with MPs. The positively charged defects present in the MOFs show high affinity to a wide range of negatively charged MPs. As mentioned, a range of techniques have been proposed for the removal of MPs from sea water, however, these methods can be expensive and may not be effective in removing MPs, especially smaller particles. Recently, new methods based on adsorbents such as MOFs are presented for removing MPs from an aqueous environment. One of the significant advantages of using MOFs for MP removal is their high

selectivity toward these particles. MOFs can be tailored for specific applications by modifying their composition and pore size to selectively capture different sizes and types of MPs. This selectivity allows more efficient removal of MPs while minimizing the impact on other water constituents. Application of MOFs for the removal of MPs from sea water is a promising method which offers a range of advantages over other techniques. Using MOF has several advantages over other methods in terms of efficiency, selectivity, regenerability, scalability, and environmental impact. They can selectively adsorb MPs while leaving other materials in the water untouched. MOFs can also be regenerated and reused for multiple cycles, making them more cost-effective and sustainable compared to single-use filters or other methods that require frequent replacement. MOFs are made from non-toxic materials and do not produce harmful byproducts during the purification process, making them a more environmentally friendly option compared to some other methods. In contrast, filtration can remove MPs but may not be as selective as MOF, and filters need to be replaced frequently. Sedimentation can be less effective for MPs removal... As research in this area continues to progress, we can expect to see the development of more efficient, cost effective, and sustainable methods for MPs removal. Several research studies have explored the use of MOFs for the removal of MPs from sea water. Chen et al. loaded melamine foam with Zr-based UiO-66-X MOFs, which were created using the 1,4-dicarboxybenzene ligand with different functional groups. The researchers tested the MOF-based foam's ability to remove MPs from a simulated suspension of three different types of plastics: PVDF, PMMA, PS. The results showed that the MOF-based foam was able to achieve a removal rate of up to 95.5%, with the removal rate affected by the particle size and zeta potential of the MPs. The MOF-based foam was also found to have good stability and reusability in repeated adsorption-desorption cycles, meaning that it could be used multiple times to remove MPs from water, making it a cost-effective solution for MPs. Furthermore, the researchers investigated the effect of MOF loading and foam density on the adsorption capacity of the MOF-based foam. They found that increasing the MOF loading and foam density resulted in higher adsorption capacity, indicating that more MOF material and higher foam density could improve the ability of the foam to remove MPs from water. It is worth noting that smaller MPs were more difficult to remove than larger ones due.

2-2. Methods

Synthesis of MIL-100-Fe & sulfonic-functionalized MIL-100 (MIL-100-Fe/AMSA)

Iron-based MIL-100 was synthesized using a rapid microwave-assisted method [38]. Typically, 2.43 g of $FeCl_3 \cdot 6H_2O$ were dissolved in 30 mL of water. After that, 0.84 g of 1, 3, 5-benzenetricarboxylic acid were added under constant stirring. The resulting mixture was introduced to a Teflon vessel and heated at 403 K for 10 min in a microwave oven. The obtained light brown solid was separated by centrifugation and washed three times with water and ethanol. Finally, the product was treated with 150 mL of ethanol at 373 K for 2hr.MIL-100-Fe was functionalized following an adaptation of the experimental procedure reported by Hasan et al.

[39]. Before functionalization, 0.5 g of MOF were activated at 453 K for 12 h in a round bottom flask with continuous circulation of N_2 to generate coordinatively unsaturated sites. After activation, MIL-100-Fe was suspended in 50 mL of ethanol, and 1 mmol of PSF was added. The mixture was stirred under reflux overnight.

The obtained solid was filtered, washed with ethanol and then dried at room temperature. The design of the 3D printed column with integrated packing based on interconnected cubes was carried out using the software Rhinoceros 5.0 SR11 32 (Mc Neel & Associates). This device was 3D printed vertically with stand with 1016 layers at a resolution of 0.500 mm using the SLA technique. In order to remove unreacted monomers, the 3D printed column was washed with 2-propanol and then dried at room temperature.

Finally, the UV post-curing was carried out for 4 h at 365 nm.MIL-100-Fe-PSF/3D column was prepared by an easy coating method using a concentrated ink [40].

Basically, 150 mg of MIL-100-Fe- PSF were dispersed in 5 mL of acetone through sonication for 30 min. Then, the dispersion was mixed with 1 g of PVDF solution (7.5 w t % in DMF), and the resulting mixture was sonicated for another 30 min, and subsequently concentrated by acetone evaporation using gentle nitrogen flow. The obtained dispersion was pumped through the 3D printed column and, after removing the excess of dispersion using a nitrogen stream, the device was introduced in an oven at 333 K to eliminate DMF.

2-3.Characterization MIL-100-Fe and MIL-100-Fe-PSF samples

Nitrogen adsorption-desorption isotherms were acquired at 77 K by using a TriStar II(Micro meritics) gas adsorption instrument. The samples were previously activated at 423 K for 15 h. Data were analysed using the Brunauer-Emmett-Teller model (BET) to obtain the specific surface area and the two-dimensional non-local density functional theory model to determine the pore size distribution. The X-ray diffraction patterns were obtained using CuK_α radiation on a Bruker D8 Advance diffractometer. The morphology and elemental distribution of the prepared materials were studied by using a scanning electron microscope (SEM) Hitachi S–3400 N, equipped with a Bruker AXS X flash 4010 energy-dispersive X-ray spectroscopy system, and transmission electron microscope (TEM) Thermo Scientific Talos F200i operated at 200 kV. Fourier transform infrared (FTIR) spectra were acquired using a Bruker 80v spectrometer equipped with an MCT cryodetector. For IR experiments, thin self-supported wafers of the MOF samples were prepared and outgassed in a dynamic vacuum at 453 K for 8 hr. After this activation treatment, carbon monoxide was dosed into the cell to study the open metal centers. A Formlabs Form 2 3D Printer and clear photoactive resin composed of methacrylate monomers/oligomers and initiator (Form labs Clear V4) were used for device fabrication. For post-curing the 3D printed devices, an Upland CL-1000 ultraviolet cross linker with a 365 nm UV lamp was used. Percent removal of

MPs by MOF were calculated in terms of mg/g with Equations (1).

$$(R\%)=\frac{(C_0-C_e)\times 100}{C_0} \qquad (1)$$

In this research, the important conditions affecting the MPs absorption process, including the concentration of the MPs, the amount of the absorbent, and the contact time, were investigated using the experimental design method. In these relationships, Ce is the equilibrium concentration and C_0 is the initial concentration of the Micro plastic in ppm. Also, the absorption capacity (M) is in mg/g.

The X-ray method was used to determine the qualitative properties of Characterization of MIL-100-Fe and MIL-100-Fe-PSF samples.

The presence of sharp peaks indicates the purity of the crystallinity and single phase of the material. With the information of the intensity and width of the peak, the average diameter of the crystal particles can be calculated from the Scherer Equation.

In Equation(2), L the average diameter of the particle, K is Scherer's constant (0.9), λ the wavelength of X-ray is 1.54060 Angstroms , θ diffraction angle of each peak and β is the width of the peak in half of the maximum height(radians)

$$L= K\lambda / \beta Cos\theta \qquad (2)$$

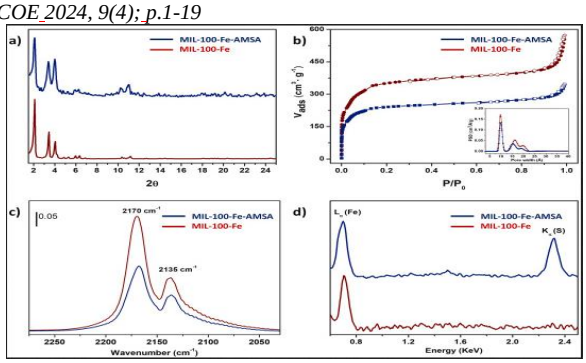

Figure9- (a) XRD patterns (b) N_2 adsorption-desorption isotherms. Inset: Pore size distribution (c) FTIR spectra of CO adsorbed at 100 K (d) energy dispersive X-ray spectra.(AMSA=AMINO METHYL SULFONIC ACID.[1])

SEM and TEM image of the organometallic structure MIL-100-Fe and PSF@Fe-BTC are shown in Figures (10). According to the obtained results, the image of PSF@ Fe-BTC shows agglomeration or clumps of irregular particles.

This organometallic sample have nanometer size. Morphology The crystal surface of PSF/MIL-100 (Fe)) is irregular, encapsulated PSF and Immobilization of this in MIL-100 (Fe)) leads to changes in the morphology of the particles and the particles lost their order and their image It goes towards irregular masses. PSF/MIL-100 (Fe)) It is amorphous

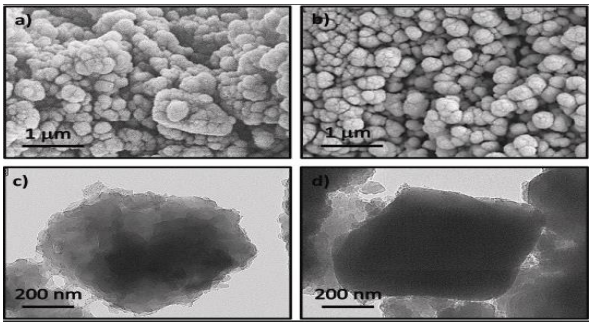

Figure10- SEM images of (a) MIL-100-Fe and (b) MIL-100-Fe-AMSA samples. TEM images of (c) MIL-100-Fe (d) MIL-100-Fe-AMSA samples.

In table 2 shown Summary of the use of different MOFs in the removal of MPs

Table 2. Summary of the use of MOFs in the removal of MPs (*NM* Not mentioned)

MOF	MPs	Size	efficiency (%)	Media
MOF@C@FeO	NM	1000 nm	100	Water
Nano-Fe@ZIF-8	PS	1.1 µm	≥ 98	Water
ZIF-8@Aerogel	PVDF, PS	60–110 nm (PVDF) 90–140 nm (PS)	Water	91.4 (PVDF) - 85.8 (PS)
Ag2O/Fe-MOF	PEG, PE, PET	NM	Deionized water	NM
MIL-100 (Fe)	PVC	40 µm PE & 140 µm (PVC)	NM	Water

3-2. Test design

The results were carried out with the statistical method of response level (RSM) in three levels and three variables table 3 with a central composite design. The number of samples has been estimated using table4. The variables by using the answer software & using quadratic regression Equation (3) was calculated.

variable	Symbol	1	0	-1
MPs (mg/l)	X	32	15	5
Time (min)	Y	6	3	1
Adsorbent (mg)	Z	5	2	1

Number	MPs (mg/l)	Adsorbent (g)	Time (min)	Percentage separation
1	25	**0.030000**	1	85.98
2	25	**0.030000**	4	90.30
3	25	**0.030000**	4	90.82
4	25	**0.030000**	4.	92.00
5	5	**0.035000**	3	91.86
6	32	**0.035000**	3	93.50
7	25	**0.030000**	4	90.68
8	32	**0.035000**	3	75.80
9	5	**0.025000**	3	95.00
10	25	**0.020000**	4	90.10
11	25	**0.030000**	4	90.30
12	10	**0.030000**	4	100.0
13	32	**0.025000**	3	92.16
14	32	**0.035000**	5	95.78
15	25	**0.030000**	4	90.12
16	15	**0.025000**	6	92.64
17	32	**0.035000**	6	78.59
18	32	**0.025000**	3	100.0
19	32	**0.025000**	6	85.57
20	5	**0.030000**	4	85.50
21	5	**0.035000**	5	92.00
22	25	**0.030000**	4	96.62
23	5	**0.035000**	5	88-5
24	5	**0.030000**	4	90.51
25	15	**0.030000**	6.	92.31
26	32	**0.035000**	6	95.41
27	5	**0.025000**	3	96.68
28	15	**0.025000**	6	92.11
29	25	**0.040000**	4	88.85
30	32	**0.025000**	6	98.28

$$Y = \sum_{i=1}^{n} \beta j\, X_i + \sum_{i=1}^{n} \beta jj\, X_i^2 + \sum_{i=1}^{n} \sum_{j=1}^{n} \beta jk\, X_i X_j + \beta 0 \quad (3)$$

In which coefficient: β_j: linear, $\beta_{j\ j}$: squared, β_k: interaction of the coefficients that the fitting constants, Xi, X_j^2, X_j, X_k: independent variables, B_0: width of the origin, Y: response .The number of test points is obtained from Equation (3). That K and C0 are the number of variables & central points, both values are set to 3 in this research. The reason that pH is omitted in the reviews is that it is difficult to consider the 4 characteristics of the experiments and also the interpretations.

Table 3. Range of variables in CCD method

According to the values determined by the model, 30 tests were performed for each factor, whose characteristics are shown in table 4.

Table4: Characteristics MPs solution and other components in experiments.

The selected software designs the experiments, the obtained model is shown by Equation(4), and table 4 of the effect of the primary factor on the interaction of the factors and the surface response is based on the ANOVA analysis, It is predicted by the statistical model and the actual value is

calculated. there is a precise relationship between both results.

$$N=2K(K-1)+C_0 \quad (4)$$

The statistical evaluation of Eqation (3) was done by performing the Fisher's test, which is a measure of the deviation of the data from the mean, and analysis of variance of the quadratic level response model. Anova data confirms the accuracy of this model. To check reliability, correlation coefficient (R^2), P value (probability at 95% confidence level), F and T-test are used. The F value equal to (72) is very high for this model and it shows that the model has predicted the test results well. The numerical value of $p<0.04$ and shows the significance of this model. Statistical tests are used to determine meaningful and non-meaningful sentences. Table (4) shows the analysis of the design of the experiment. Coefficients with small P value are significantly greater zero.

Here $p<0.04$ is significant at $\alpha=0.05$ level and corresponds to 95% confidence level. If the P for Lack-of-Fit is greater than the value chosen to be significant with a certain confidence level, it indicates that the model is favorable.

The values of Also R adj and R pred to the order is 0.9716 and 0.7435, it is in agreement and shows the good accuracy of the used model. On the other hand, the effect of three variables on the percentage of MPs absorbed amount is shown in **F**igures 11 to 13. In each Figure the response surface graphs as a function of a characteristic and it is also drawn on two characteristics at the same time with Expert seven Trial software. By examining the graphs of the response level, it can be seen that the relationship between characteristics is significant. effect of adsorbent conc. on the amount of **MPs** solution separation with the software is shown in Figure **11.**

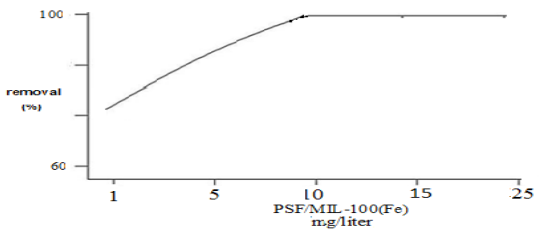

Figure11: Effect of adsorbent conc. on the amount of MPs solution separation with the software.

The influence curve of the on the separation percentage is shown in Figure 12.

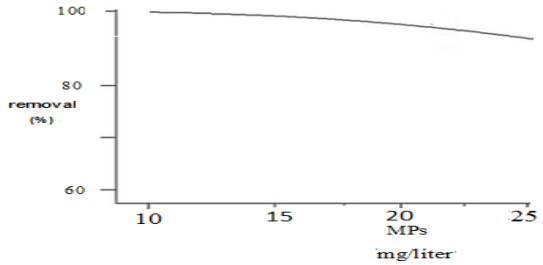

Figure 12: Effect of MPs factor on separation percentage

Also with the increase in contact time of the absorbent with the MPs, the percentage of removal increases and after 10 minutes due to the Filling of the empty places of the absorbent, it becomes a constant trend, In investigating the effect of the amount of adsorbent, different amounts of MOF have been used in the conditions of the initial MPs concentration of 5 mg/liter. The maximum removal of the MPs was with the amount of 25 mg/liter from the absorbent and after 10 minutes with the increase in the amount of absorbent, Figure 13 shown the effect of two characteristics of the concentration of the solution containing the MPs and the amount of adsorbent on the removal of the MPs can be seen simultaneously.

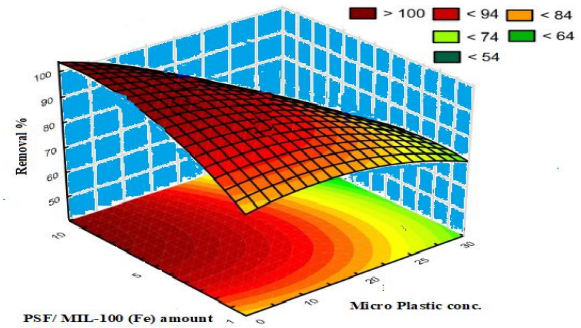

Figure 13: Effect of MPs factor & adsorrbent on separation percentage

The amount of adsorbent in high concentration of the MPs has an effect more will have an effect on the absorption percentage as well characteristic of concentration on absorption percentage will be very small. The percentage of removal increases with the increase of the absorber can be justified according to the increase of active sites based by increasing the amount of adsorbent, the percentage of removal must increase, because the number of accessible sites for adsorbed molecules increases with the increase of adsorbent amount.

Variaion	Sum of Square Between & within groups	Freedom	Mean Square	*F*	p
Model	796/43	20	44/821	18/8	< 0.0001
MP	142/08	1	162/08	68/2	< 0.0001
Adsorbent	50/257	1	50/257	21/1	0/000763
Time	12/084	1	12/084	5/08	0/0454
pH & MP	72/038	1	72/038	30/3	0/0001
MPs & A	12/443	1	12/443	5/24	0/0022
MPs & T	114/33	1	114.33	48/1	< 0.0001
pH & A	14/044	1	14.044	5/91	0/0332
pH & T	117/99	1	117/99	49/6	< 0.0001
A & T	3/3215	1	3/3215	1/39	0.0001
(MPs)2	0/8843	1	0/88439	0/37	0/5540
(pH)2	17/060	1	17/060	7/185	0/0213
(A)2	29/694	1	29/694	12/5	0/0046
(T)2	33.970	1	33/970	14/3	0/0030
Residual	26/118	11	2/3743		
Lack of Fit	17/177	6	2/8628	0.08	0.2

On Figure 14 shown **e**ffect of time factor & adsorrbent on adsorbent capacity (q).

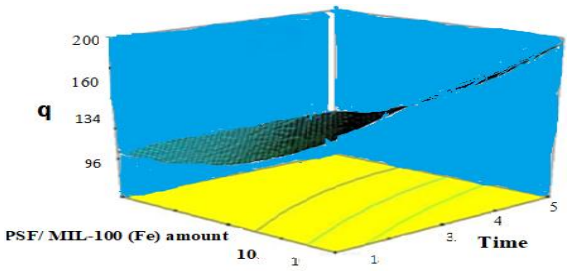

Figure 14: Effect of Time factor & adsorrbent on adsorbent capacity

The answer P and F obtained for answer and are given in table (5).

Table 5: P and F response values obtained from surface response analysis for response

According to the value of MPs, although by increasing the amount of adsorbent, more MPs can be absorbed, but in the unit mass of the adsorbent, this amount takes a decreasing trend. The effect of time is insignificant. The effect of the concentration of the MPs on the amount adsorption is greater, and at higher concentrations of the MPs, the effect of the amount adsorption is also lower Figure 13.

In the alkaline environment, the hydroxide agent increases in solution Findings and the surface of the absorbent with the loss of hydronium ion has a negative charge on the surface, which will cause the amount of electrostatic attraction between the positively charged MPs and the absorbent surface to increase, and in this way, the absorption of the MPs will increase to the saturation level.

This phenomenon is the presence of negative charge surface groups that It prevents the absorption of negative ions and for the absorption of cationic ions It is more practical, so the efficiency of the absorption process is highly dependent on functional groups present on the surface to absorb a type of pollutant

It is special to increase the removal with increasing amount of adsorbent due to increase Absorbent surface and greater access to absorption and decomposition sites It is an PSF because with the increase of the active level, the amount of MPs removal catalyst is also increased more free surfaces cause them to remain empty, that's Why the percentage Absorption remains constant and the equilibrium absorption capacity decreases. [41]

3. Results and Discussion

Mohana et al, conducted a study to investigate the behavior of MPs in water and their removal using MOF-based membranes. They utilized MOF-based ED-MIL 101(Cr) UF membrane. According to their findings, the MOF based ED-MIL 101(Cr) UF membrane exhibited efficient water permeability and had the potential to remove over 90% of negatively and positively charged MPs from water through electrostatic forces of attraction and repulsion. The research showed that MPs have the ability to break down into smaller particles in water, which could lead to an increase in their distribution and harmful effects. Researcher discovered that MF and UF membranes were successful in removing MPs, with removal rates ranging from 80-99%. and NF and RO membranes were not as efficient due to their smaller pore sizes, which can lead to fouling and reduced membrane performance over time. Golgoli et al. prepared a thin-film composite as a hydrophilic and stable MOF by incorporating different concentrations of MIL-53 (Fe) in the substrate layer of PSF membranes, which showed higher performance, antifouling behavior, hydrophilicity, roughness, and porosity compared to the untreated membrane.(0.2wt % MIL-53(Fe) loading) indicated a smoother and more hydrophilic surface having a more nodular structure. The presence of the MOF increased the porosity and hydrophilicity of the substrates leading. MOFs with nanoscale pore sizes can remove MPs despite the size mismatch. They can act as a barrier or sieve, preventing the passage of larger MPs. MOFs exhibit diverse surface properties, such as dual charge characteristics or specific functional groups [42]. The incorporation of MOFs into foams and membranes, increases filtration performance by enhancing porosity and surface area, facilitating better contact between MOFs and contaminants. The use of MOFs increases substrate porosity and hydrophilicity, while forming a smooth and hydrophilic protective layer on the membrane surface. Qin et al, tried to tackle two significant environmental problems: the buildup of MPs and the necessity for renewable energy sources. Their proposed solution involves a new photocatalytic process that employs the Ag2O/Fe-MOF catalyst. This process can transform polyethylene glycol, PE, and polyethylene terephthalate plastics into useful chemicals, and additionally generate hydrogen. The photocatalytic and non-homogeneous photo catalysts are the basis of this approach, utilizing light to transform MPs into valuable substances. [43], The scientists used a fresh approach to create photo catalysts for the

conversion of MPs by transforming the metallic locations on a MOF into semi-conductive nanoparticles. The Fe Ag-MOF was the precursor used, and the exposure to light caused the formation of 6 nm Ag2O particles within the MOF structure. The resulting Ag2O/Fe-MOF has active sites that absorb a vast range of solar light, allowing it to be an efficient catalyst for converting MPs into useful chemicals and producing hydrogen.

The study findings indicated that the Ag2O/Fe-MOF was more effective in terms of its photocatalytic efficiency and hydrogen production rate when compared to pure Ag2O. Additionally, it exhibited selectivity in converting MPs into useful chemicals, presenting a sustainable and eco-friendly solution for managing plastic waste. The technique researcher proposed involves transforming the metallic sites on MOFs into semi conductive particles that work as photo catalysts to convert MPs into valuable substances.

You et al used MOF-based wood aerogel for removing MPs The results of the study indicate that ZIF-8@Aerogel has a highly favorable effect on the removal of nanoparticles of PVDF and PS in seawater was similar to that in water. The removal efficiencies for these particles reached 91.4% and 85.8%, respectively.

In comparison, a similar experiment was conducted using only aerogel to remove the MPs, and the removal efficiencies were found to be significantly lower, at 56.9% for PVDF and 42.5% for PS. To further verify the removal performance of ZIF-8@Aerogel in natural aquatic environments,

This demonstrates the potential of ZIF-8@A to effectively remove nano MPs in real-world applications. The removal performance of ZIF-8@A on MPs is the result of a combination of different factors. The first factor is the strong electrostatic interaction between the positively charged ZIF-8 within the aerogel and the negatively charged MP particles. Another factor is the hydrophobic interaction between the MPs and ZIF-8. This interaction is enhanced by the fact that both PVDF, PS, ZIF-8 are hydrophobic substances, meaning they repel water. This hydrophobic interaction makes it easier for the ZIF-8 to trap and remove the MPs from the water. Additionally, there is a potential van der Waals force between the MP molecules and the composite material molecules.

Pasanen et al, conducted a study to assess the effectiveness of nano-Fe@ZIF-8 in removing MPs. They found that using 5mg of nano-Fe@ZIF-8. This improvement was due to the smaller particle size, which increased the available effective surface area for interaction between the ZIF crystals and PS microspheres. The study also examined the effect of agitation time on the MPs removal efficiency and found that the removal efficiency increased with an increase in agitation time, reaching a maximum at 5min. The researchers also found that the nano-Fe@ZIF-8 was effective in removing MPs with different sizes and functionalities, including 15μm PS beads and 1μm carboxyl-functionalized PS beads.

Haris et al. using a nano pillared structure made up of a two-dimensional MOF and carbon encapsulated iron oxide (C@FeO) nano pillars. To

address these issues, a new 2D nano pillared hetero structure was developed by growing a 2D MOF on magnetic nanoparticles made of C@FeO. The self-assembly of this nano material between the MOF sheets prevents the 2D sheets from sticking together, thereby significantly increasing the surface area. Additionally, the magnetic properties of that make it easy to separate the adsorbent from the water. This material can remove 71.7% of MPs with concentration of 1000 mg/L in 60 min while the MOF@C@FeO was found to remove 100% of both MPs and MB from a binary system in just 60 min. The MOF@C@FeO was tested for reusability and stability over 6 consecutive adsorption cycles and removal efficiency was obtained 90%.

Therefore, the study found that ZIF-67 is a promising material for removing MPs from water, thanks to its effective use of hydrogen bonding, electrostatic attraction, and π–π stacking. These findings have the potential to contribute to the development of new water for removing MPs, especially in environments with low to moderate alkalinity. there is no specific technique to entirely remove MPs from aqueous environment. Geometry, size and density of them dictate how they can be dispersed. Large, dense and irregular-shaped particles tend to sediment underwater while smaller, lighter and spherical-shaped MPs are retained on the surface. MOFs have emerged as a promising solution for removing MPs from aqueous environments due to their high surface area, tailored porosity, renewability, chemical stability, and versatility. of course, MOFs have some drawbacks, such as their often-unstable powder form, these can be overcome by supporting MOFs on other substrates, such as aerogels or foams. [44-45]

4-Conclusions

In this work, we fabricated a novel composite membrane composed of hydrophilic PSF/MIL-100 (Fe) incorporated in a poly sulfone matrix for the excellent removal of MPs .MIL-100 (Fe) is a type of MOF that contains iron metal ions and terephthalic acid organic ligands, resulting in a mesoporous structure with a small pore diameter (1.79 nm), large pore volume (0.8385 cm3/g) and micro porous windows which allow for the transport of small molecules to create the blended membrane, the researchers integrated hydrophilic MIL-100 (Fe) nanoparticles into a poly sulfone matrix. The incorporation of MIL-100(Fe) significantly affected the morphology of the membrane, including its hydrophilicity, porosity, wetting energy, work of adhesion, and pore size. The best performance was achieved using a 0.50 wt % loading of MIL-100 (Fe) in the PSF matrix, The PSF/MIL-100 (Fe) membrane showed optimal performance in an alkaline environment (pH 10) due to the electrostatic repulsion mechanism towards cationic-charged contaminants. The study also demonstrated the membrane's reusability, as the organic ligands in the MIL-100 (Fe). Structure help to retain its stability even after several cycles of use. overall, the results of this study suggest that the PSF/ MIL-100 (Fe) blended membrane is an effective method for removing MPs from seawater. The use of MIL-100 (Fe) in the membrane design contributes to its high surface area, which is critical for efficient removal of MPs. The optimal removal of MPs was achieved using 10 mg of nano PSF/ MIL-100 (Fe) (1:4) with 100 % removal MPs within 5 min. The structure boasted a large surface area of 1000 m2/g, many active sites, and magnetic

properties that make it easy to separate MPs from the water.

5. Thanking

The author of the article is grateful to Qom University of Technology & Tehran University, which has provided the utmost cooperation in the implementation of this research

6. Conflict of interest

No conflict of interest has been declared by the authors in this article is.

7. References

1-Zhila Honarmandrad, Massoud Kaykhaii1 and Jacek Gębicki. (2023) Micro plastics removal from aqueous environment by metal organic frameworks. *BMC Chemistry,17:122*

2-Holm P, Schulz G, Athanasopulu K. Mikroplastik (2013). ein unsichtbarer Störenfried. Biol Unserer Zeit. 1(43), 27–33.

3. Darabi M, Zhang Y. (2021) Removal of microplastic pollution in water and wastewater treatment. Green Chem Water Treat. 7, 109.

4. Shahraki M, Rezaei Kahkha MR, Piri J, Sharafi A, Kaykhaii M. (2022) Microplastics in atmospheric dust samples of Sistan: sources and distribution. J Environ Health Sci Eng. 20, 1–6.

5. Mishra S, Das AP. (2021) Current treatment technologies for removal of microplastic and microfiber pollutants from wastewater. Wastewater treatment. Elsevier; 237–51.

6. Barnes D, Galgani F, Thompson R, Barlaz M. (2009) Accumulation and fragmentation of plastic debris in global environments. Philos Trans R Soc B Biol Sci.;364,1985–98.

7. Picó Y, Barceló D. (2019).Analysis and prevention of microplastics pollution in water: current perspectives and future directions. ACS Omega. 4(4), 6709–19.

8. Duis K, Coors A. (2016) Microplastics in the aquatic and terrestrial environment: sources (with a specific focus on personal care products), fate and effects. ESEU28(1), 1–25.

9. Browne MA, Crump P, Niven SJ, Teuten E, Tonkin A, Galloway T, et al. (2011). Accumulation of microplastic on shorelines worldwide: sources and sinks.Environ Sci Technol. 45(21), 9175–9.

10. Sul J, do, Costa MF, Fillmann G. (2014) Microplastics in the pelagic environment around oceanic islands of the Western Tropical Atlantic Ocean. Water Air Soil Pollut. 225, 1–13.

11. Barrett J, Chase Z, Zhang J, Holl M, Willis K, Williams A, et al. (2020). Microplastic pollution in deep-sea sediments from the great Australian bight. Front Mar Sci. 7, 576170.

12. Van Franeker JA, Blaize C, Danielsen J, Fairclough K, Gollan J, Guse N, et al. (2011).Monitoring plastic ingestion by the northern fulmar *Fulmarus glacialis* in the North Sea. Environ Pollut.159(10), 2609–15.

13. Liu Y, Guo R, Zhang S, Sun Y, Wang F. (2022). Uptake and translocation of nano/ microplastics by rice seedlings: evidence from

a hydroponic experiment.J Hazard Mater.421, 126700.

14. Ma J, Aqeel M, Khalid N, Nazir A, Alzuaibr FM, Al-Mushhin AA, et al. (2022). Effects of microplastics on growth and metabolism of rice (*Oryza sativa* L.). Chemosphere. 307, 135749.

15. Kaykhaii M, Honarmandrad Z, Gębicki J. (2023). Effect of microplastics pollution on hydrogen production from biomass: a comprehensive review. Ind Eng Chem Res. 62(9), 3835–43.

16. Gola D, Tyagi PK, Arya A, Chauhan N, Agarwal M, Singh S, et al. (2021). The impact of microplastics on marine environment: a review. Environ Nanotechnol Monit Manag. 16,100552.

17. Galloway TS, Lewis CN. (2016). Marine microplastics spell big problems for future generations. PNAS. 113(9), 2331–3.

18. Cox KD, Covernton GA, Davies HL, Dower JF, Juanes F, Dudas SE. (2019). Human consumption of microplastics. Environ Sci Technol. 53(12), 7068–74.

19. Leslie HA, van Velzen MJM, Brandsma SH, Vethaak AD, Garcia-Vallejo JJ, Lamoree MH. (2022).Discovery and quantification of plastic particle pollution in human blood. Environ Int. 163, 107199.

20. Haris M, Khan MW, Zavabeti A, Mahmood N, Eshtiaghi N. (2022). Self-assembly of C@ FeO nanopillars on 2D-MOF for simultaneous removal of microplastic and dissolved contaminants from water. Chem Eng J. 455, 140390.

21. Pasanen F, Fuller RO, Maya F. (2023).Fast and simultaneous removal of microplastics and plastic-derived endocrine disruptors using a magnetic ZIF-8 nanocomposite. Chem Eng J. 455, 40405.

22. Poerio T, Piacentini E, Mazzei R. (2019). Membrane processes for microplastic removal. Molecules. 24(22), 4148.

23. Sajid M, Ihsanullah I, Khan MT, Baig N. (2022). Nanomaterials-based adsorbents for remediation of microplastics and nanoplastics in aqueous media: a review. Sep Purif Technol. 305, 122453.

24. Laglbauer BJ, Franco-Santos RM, Andreu-Cazenave M, Brunelli L, Papadatou M, Palatinus A, et al. (2014). Macrodebris and microplastics from beaches in Slovenia. Mar Pollut Bull. 89(1–2), 356–66.

25. Yu Y, Mo WY, Luukkonen T. (2021).Adsorption behaviour and interaction of organic micropollutants with nano and microplastics—a review. Sci Total Environ. 797, 149140.

26. Khan A, Jia Z. (2023). Recent insights into uptake, toxicity, and molecular targets of microplastics and nanoplastics relevant to human health impacts. Iscience. 26, 106061.

27. Kentin E, Kaarto H. (2018). An EU ban on microplastics in cosmetic products and the right to regulate. RECIEL. 27(3), 254–66.

28. Üstün GE, Bozdaş K, Can T. (2022). Abundance and characteristics of microplastics in an urban wastewater treatment plant in Turkey. Environ Pollut. 310, 119890.

29. Amrutha K, Warrier AK. (2020). The first report on the source-to-sink characterization of microplastic pollution from a riverine environment in tropical India. Sci Total Environ. 739, 140377.

30. Okoffo ED, O'Brien S, O'Brien JW, Tscharke BJ, Thomas KV.(2019).Wastewater treatment plants as a source of plastics in the environment: a review of occurrence, methods for identification, quantification and fate. Environ Sci Water Res Technol. 5(11), 1908–31.

31. Mintenig SM, Int-Veen I, Löder MG, Primpke S, Gerdts G. (2017). Identification of microplastic in effluents of waste water treatment plants using focal plane array-based micro-fourier-transform infrared imaging. Water Res. 108, 365–72.

32. Karthik R, Robin R, Purvaja R, Ganguly D, Anandavelu I, Raghuraman R,et al. (2018). Microplastics along the beaches of southeast coast of India. Sci Total Environ. 645, 1388–99.

33. Fendall LS, Sewell MA. (2009). Contributing to marine pollution by washing your face: microplastics in facial cleansers. Mar Pollut Bull. 58(8), 1225–8.

34. Shen M, Song B, Zhu Y, Zeng G, Zhang Y, Yang Y, et al. (2020). Removal of microplastics via drinking water treatment: current knowledge and future directions. Chemosphere. 251, 126612.

35. Singh S, Kalyanasundaram M, Diwan V. (2021). Removal of microplastics from wastewater: available techniques and way forward. Water Sci Technol. 84(12), 3689–704.

36. Zhang Y, Jiang H, Bian K, Wang H, Wang C. (2021). A critical review of control and removal strategies for microplastics from aquatic environments. J Environ Chem Eng. 9(4), 105463.

37. Sun J, Dai X, Wang Q, Van Loosdrecht MC, Ni B-J. (2019). Microplastics in wastewater treatment plants: detection, occurrence and removal. Water Res. 152, 21–37.

38. Yuan F, Zhao H, Sun H, Sun Y, Zhao J, Xia T. (2022). Investigation of microplastics in sludge from five wastewater treatment plants in Nanjing, China.J Environ Manage. 301, 113793.

39. Wan H, Wang J, Sheng X, Yan J, Zhang W, Xu Y. (2022). Removal of polystyrene microplastics from aqueous solution using the metal–organic framework material of ZIF-67. Toxics. 10(2), 70.

40. Wiśniewska M, Chibowski S, Urban T, Sternik D, Terpiłowski K.(2016). Impact of anionic polyacrylamide on stability and surface

properties of the Al2O3– polymer solution system at different temperatures. Colloid Polym Sci. 294, 1511–7.

41. Lapointe M, Farner JM, Hernandez LM, Tufenkji N. (2020). Understanding and improving microplastic removal during water treatment: impact of coagulation and flocculation. Environ Sci Technol. 54(14), 8719–27.

42. Guo Y, Liang H, Bai L, Huang K, Xie B, Xu D, et al. (2020). Application of heatactivated peroxydisulfate pre-oxidation for degrading contaminants and mitigating ultrafiltration membrane fouling in the natural surface water treatment. Water Res. 179, 115905.

43. Waldschläger K, Schüttrumpf H. (2020).Infiltration behavior of microplastic particles with different densities, sizes, and shapes—from glass spheres to natural sediments. Environ Sci Technol. 54(15), 9366–73.

44. Talvitie J, Mikola A, Koistinen A, Setälä O. (2017). Solutions to microplastic pollution–removal of microplastics from wastewater effluent with advanced wastewater treatment technologies. Water Res.123, 401–7.

45. Heinonen M, Koistinen A, Talvitie J, Mikola A. (2017). How well is microliter purified from wastewater? A detailed study on the stepwise removal of microliter in a tertiary level wastewater treatment plant. Water Res. 109, 164–72

INTERNATIONAL JOURNAL OF
COASTAL, OFFSHORE & ENVIRONMENTAL ENGINEERING IJCOE Vol.9/No.4 /Autumn 2024 (20-29)

Available online at: www. Ijcoe.org

Numerical simulation of flow for improved width of the shipwreck in the curvature of the Waal River in Netherlands by using of Groyns

Parisa Alinouri [1], Mehdi Nezhadnaderi[2]*, Mohammad Hossein Vafaee [3], Babak Fazli Malidareh[4], Babak Pordel Maragheh[5]

[1] *MSc of Water Engineering- Water Structures, Imam Khomeini International University, Qazvin, Iran. P.alinouri2018@gmail.com*
[2*] *Department of Civil Engineering, Tonekabon Branch, Islamic Azad University, Tonekabon, Iran. (Corresponding Author). mehdi2930@yahoo.com.*
[3] *Assistant Professor, Department of Civil Engineering, Pooyesh Instituteof Higher Education, Qom.Iran. M.h.vafaee2024@gmail.com*
[4] *Department of Civil Engineering, Babol Branch, Islamic Azad University, Babol, Iran. Fazli.babak@babolia.ac.ir*
[5] *Department of Civil Engineering, Ardabil Branch, Islamic Azad University, Ardabil, Iran. civil_babak2005@yahoo.com*

ARTICLE INFO

Article History:
Received: 11 Sep 2024
Accepted: 4 Oct 2024

Keywords:
Groyne
Flow pattern
Secondary currents
90 Degree bend
Waal river

ABSTRACT

One of the effective methods for protecting the shores of navigable rivers at the site of the arches is the use of groynes. In order to study a case in the Netherlands, a numerical study was carried out on the effects of using submerged vanes with vertical groynes on the protection of the Waal coast in Netherlands. In the present study, the numerical results of the impact of vertical groynes series with 5 angular deviations were compared to the external arc wall with a length of 25% channel width (87.5 m) and a spacing of 595.859 meters with a nonsubmerged vane at a distance of one fourth of the width of the internal arc with a full arc length of 90 degrees are paid to the average velocity distribution and pressure in the arc of 90 degrees, with a width of 350 meters and a depth of 4.5 meters. The results of the study showed that the presence of groynes series causes uniformity of upstream velocity and high-velocity transmission from the inner arc to the middle of the canal. In the case of the presence of groynes in the outer arc with a submerged vane close to the inner arch, about one quarter of the width of the internal arc produces a counterflow stream that reduces the normal secondary flow in the bends of the river. Hence, the high- velocity current, which is driven radially to the inner shore, is diverted to the middle direction. So it will improve the sedimentation on the inner shore of the bend and scouring on the outer shore of the bend. In this way, the flow rate from the mean value of one meter per second reaches 1.98 m/s in the middle region and decreases from the sedimentation in this range.

[1)] MSc
[2)] Associate Professor
[3)] Assistant Professor

1. Introduction

With the increase of construction on the banks of the rivers, the use of protective structures to preserve and restore the banks of the rivers is considered. Among the coastal protection structures, there are breakwaters that are used in coastal engineering to protect and stabilize beaches. These structures are simple in terms of structure and have the ability to adapt to all kinds of diverse conditions and have a wide application in stabilization and stabilization of beaches, hence the investigation and understanding of the process of erosion and sedimentation in the area of breakwaters in terms of design, protection and maintenance are very important.

Considering that the topic of this research is related to the effect of using breakwaters in coastal protection, it is appropriate to briefly describe the organization methods and determine the position of breakwaters before entering the main discussion and dealing with it. Considering that in many cases, the design and construction of breakwaters is not cost-effective due to the lack of access to suitable materials, although breakwaters have been used in different cases in different countries, but the criteria and design criteria for it are not clear. Because these types of structures can be used in many cases to protect the coasts of the country, it seems necessary to study and research in this case.

In recent decades, many laboratory or numerical studies have been conducted in the field of flow patterns in arches, which led to the development of different methods and techniques for river management, among which the laboratory study of Shukri (1950) can be mentioned. He observed that for an arc with a gentle curve, the place of maximum velocity in the first half of the arc inclines towards the inner wall and moves towards the exit of the arch towards the outer wall. Based on the research of Vashni and Grade (1975) when R/B (ratio).

If the radius of the arch is more than 3.5, the shear stress distribution in the entrance section of the arch is almost uniform, and the maximum stress area occurs in the exit part of the arch and its outer wall (cited by Ghodisian, 2008).

Tingsanchali and Maheswaran (1990) used a two-dimensional numerical model to investigate the distribution of average velocity and bed shear stress near a breakwater located in a rectangular channel, and according to the curvature of the flow lines around the breakwater, they added a correction factor to the k-ε model.

Giri et al. (2004) investigated the flow and turbulence pattern in a flume similar to spiral rivers by changing the position of the non-submersible breakwaters investigated its effect on the flow field around the breakwater. The results of the experiments and their comparison with the extended model showed the effectiveness of the above model in showing the distribution of the speed and intensity of the flow in the shear layer.

2008) used measured three-dimensional velocity data in small agricultural waterways in the Midwest region to determine the flow pattern around submerged weirs constructed in the arch of the waterway. These researchers developed a three-dimensional mathematical model to simulate the flow pattern around submerged spillways and used real data to calibrate their model.

Duan et al. (2009) obtained three-dimensional data of velocity in a straight channel with the presence of a rectangular breakwater and investigated the flow pattern in two flow fields of smooth bottom and bottom with scour hole. Their research shows an increase in the longitudinal and transverse components and a decrease in the vertical component of the velocity after the formation of the scour hole, and the shear stress of the bed around the scour is reported to be six to eight times greater than the upstream shear stress.

Van den Hewer - (2013) conducted a laboratory study to investigate the erosion, sedimentation and flow hydraulics in a laboratory model made similar to spiral rivers. The length, distance and placement angle of breakwaters were the variables studied by him. From the results of his research, we can refer to the report of the creation of a low-velocity area between breakwaters, where sedimentation takes place in this area. As the distance between the breakwaters increases, the speed between the breakwaters increases, and this increase in speed causes a change in the sedimentation pattern between the breakwaters.

Qodsian et al. (2007) investigated the two-dimensional flow pattern around a single breakwater in different positions in the arch and with changes in the length of the breakwater and the descent number of the flow, from the results of this research, the ratio of the maximum shear stress to the upstream shear stress at the breakwater location and to the maximum It reaches 10 to 20 degrees downstream of the breakwater.

Fazli et al. (2008) conducted a research and compared the shear stress calculation methods in arched channels. In this laboratory research, computational stresses were investigated and compared with two methods of averaging velocity in depth and using Reynolds stress. The results of this research showed that the distribution of shear stress in the arch, which is obtained by averaging in depth, is more consistent with the process of scouring and deposition in the arch than the distribution of shear stress calculated by the method of Reynolds stresses. Also, how The distribution of the average velocity of

the flow near the bottom, which is related to the shear stress of the bed, shows better agreement with the shear stress calculated by the averaged velocity method in depth. Qodsian (2008) investigated the effect of different parameters on the flow and scour pattern around the breakwater in the 90 degree arc. Among these parameters, we can mention the flow rate, the length of the breakwater, the location of the breakwater in the arch, the distance and number of breakwaters, and the radius of curvature of the arch. From the results of this research, it can be pointed out that the amount of shear stress upstream of a single breakwater does not change with the increase in its length and the increase in shear stress at the breakwater location with the increase in the length of the breakwater. Also, the results of this research show the deviation of the high-speed area from the vicinity of the outer wall of the arch towards the inner wall and the middle of the channel by installing breakwaters in different positions of the arch.

2. Methods

A critical review of available turbulence models with the aim of evaluating their suitability for use in hydraulic problems is valuable and needed. This was done by Professor Wolfgang Reddy with years of experience in the development and application of these models. In the book ((turbulence models and their application in hydraulics)), he introduced the topic of turbulence modeling in a simple way that can be understood by any reader with basic knowledge in the field of fluid mechanics and summarized the latest published articles in this field. is In the first chapter, the role of turbulence models is explained (Salehi Nishabouri and Nasiri Saleh, 2017).

Basic conservation laws are expressed by exact equations (Navier-Stokes equations). They describe all the details of fluid movement. Since there is little hope to solve these equations and also due to the lack of interest of engineers in the details of oscillatory motion, a statistical approximation (which was first proposed by Asburn Reynolds) was used and these equations, on the time scale - which in The comparison with the time scale of turbulent motion is large - they were averaged.

Unfortunately, the averaging operation creates a new problem that the equations cannot form a closed system, because they contain unknown sentences that describe the transfer of the amount of motion, heat, and average mass by means of turbulent motion. This system of equations can be closed only by using experimental input, therefore, calculation methods based on averaged flow equations are semi-empirical.

The so-called field methods - which use the original partial differential equations - require the specifications of the turbulent transfer terms that appear in the equations at every point of the flow. This specification is defined by using the equations (algebraic or differential) that determine the turbulent transfer terms in the average flow equations, and the system of equations is closed using those equations. The basis of chaos models are hypotheses about chaotic processes that require experimental input in the form of constants or functions. They do not simulate the details of the turbulent motion, but simply "simulate the effect of turbulence on the behavior of the average flow" (Salehi Nishabouri and Nasiri Saleh, 2017).

In this study, flow is unsteady with two-dimensional turbulence form. Velocity and pressure are a function of time and space. To model of the velocity and pressure fluctuations is the integrated from the Navier Stokes equation at time. Integration of Navier Stokes equations at time is known Reynolds equations (Reynolds, 1984). Turbulence model equations are two equation models k-ε (Standard) that have be averaged in depth (Rastogi and Reddy, 1978). ε equation is as one of the main sources of the limitations of accuracy of the standard version of the k-ε model and the Reynolds stress model. It is interesting that k-ε model includes a correction term that is dependent to strain with c13 constant in the ε equation of RNG model (Yakhot et al, 1992). WillCox provided turbulence equations of k-ω (standard) model (WillCox, 1988).

$$\frac{\partial u}{\partial x}+\frac{\partial v}{\partial y}+\frac{\partial w}{\partial z}=0 \quad (1)$$

$$\frac{\partial \rho u}{\partial t}+\frac{\partial \rho uu}{\partial x}+\frac{\partial \rho uv}{\partial y}+\frac{\partial \rho uw}{\partial z}-\rho f_c v=-\frac{\partial P}{\partial x}+\frac{\partial \tau_{xx}}{\partial x}+\frac{\partial \tau_{xy}}{\partial y}+\frac{\partial \tau_{xz}}{\partial z} \quad (2)$$

$$\frac{\partial \rho v}{\partial t}+\frac{\partial \rho uv}{\partial x}+\frac{\partial \rho vv}{\partial y}+\frac{\partial \rho vw}{\partial z}+\rho f_c u=-\frac{\partial P}{\partial y}+\frac{\partial \tau_{yx}}{\partial x}+\frac{\partial \tau_{yy}}{\partial y}+\frac{\partial \tau_{yz}}{\partial z} \quad (3)$$

$$\frac{\partial \rho w}{\partial t}+\frac{\partial \rho uw}{\partial x}+\frac{\partial \rho vw}{\partial y}+\frac{\partial \rho ww}{\partial z}=-\frac{\partial P}{\partial z}+\frac{\partial \tau_{zx}}{\partial x}+\frac{\partial \tau_{zy}}{\partial y}+\frac{\partial \tau_{zz}}{\partial z}-\rho g \quad (4)$$

Turbulence model equation

Known two-equation model of k-ε (Standard) are presented for averaged form in depth as follows: (Rastogi and Reddy, 1978).

$$\frac{\partial hk}{\partial t}+\frac{\partial U_j hk}{\partial x_j}=\frac{\partial}{\partial x_j}[(\nu+\frac{\nu_t}{\sigma_k})h\frac{\partial k}{\partial x}]+hP_k+hP_{kv}-h\varepsilon \quad (5)$$

$$\frac{\partial h\varepsilon}{\partial t}+\frac{\partial U_j h\varepsilon}{\partial x_j}=\frac{\partial}{\partial x_j}[(\nu+\frac{\nu_t}{\sigma\varepsilon})h\frac{\partial \varepsilon}{\partial x}]+hc_{1\varepsilon}\frac{\varepsilon}{k}P_k+hP_{\varepsilon v}-hc_{2\varepsilon}\frac{\varepsilon^2}{k} \quad (6)$$

$$\frac{\partial h\varepsilon}{\partial t}+\frac{\partial U_j h\varepsilon}{\partial x_j}=\frac{\partial}{\partial x_j}\left[\left(\nu+\frac{\nu_t}{\sigma_\varepsilon}\right)h\frac{\partial \varepsilon}{\partial x}\right]+hc_{1\varepsilon}\frac{\varepsilon}{k}P_k+hP_{\varepsilon v}-hc_{2\varepsilon}\frac{\varepsilon^2}{k}\ \nu_t=c_\mu\frac{k^2}{\varepsilon},P_k=2\nu_t S_{ij}.S_{ij} \quad (7)$$

$$P_{kv}=c_k\frac{k^2}{\varepsilon},c_k=\frac{1}{c_f^{1/2}},P_{\varepsilon v}=c_\varepsilon\frac{u_f^4}{h^2},c_\varepsilon=\frac{1}{\sqrt{e_*\sigma_t}}\frac{c_{2\varepsilon}c_\mu^{1/2}}{c_f^{3/4}},c_f=\frac{u_f^2}{u^2+v^2+w^2}=\frac{n^2g}{h^{1/3}} \quad (8)$$

$$c_\mu=0.09,c_{\varepsilon 1}=1.44,c_{\varepsilon 2}=1.92,\sigma_k=1.0,\sigma_\varepsilon=1.31$$

P_{kv} and P_{kv} are production terms as result of non-uniform distribution velocity in depth that is stronger near-bed. P_k is production term of turbulent kinetic energy averaged in depth as result of velocity gradients in the plan. ν_t is the vortex viscosity. Turbulence model is used for calculation of lateral flow into one channel and is achieved much better results in comparison with ν_t for fixed parameters of rotational flow (MCGurik and Rodi, 1978). c_f is the bed friction coefficient. σ_t is Schmidt number that shows relationship between turbulence viscosity and turbulent diffusion coefficient according to the following equation:

$$\varepsilon_d=\frac{\nu_t}{\sigma_t} \quad (9)$$

Amount of σ_t is considered 0.5 (Keller and Rodi, 1988). Although values of σ_t are 0.5 to 2 in variable references (Gibson and launder, 1978). e_* is coefficient that gives turbulence diffusion coefficient in depth by following equation (Keller and Rodi, 1988).

$$\varepsilon_d=e_*hu_f \quad (10)$$

Direct measurement of color broadcasting in the fixed-width channels offers 0.15 for e_*. Although Keller and Rodi achieved better solutions for the velocity and stress within the composite channels (Keller and Rodi, 1988). On the other hand Biglari and Sturm have been assumed e_* equaled to 0.3 to get the better answer within the composite channels (Biglari and Sturm, 1998). MCGurik and Rodi have considered $\frac{1}{\sqrt{e_*\sigma_t}}$ equaled to 3.6 (MCGurik and Rodi, 1978). In ε equation of RNG model includes a correction term $c_{\varepsilon 1}$ that is constant strain-dependent (Yakhot et al, 1992). For k-ε (RNG), we have:

$$\frac{\partial h\varepsilon}{\partial t}+\frac{\partial U_j h\varepsilon}{\partial x_j}=\frac{\partial}{\partial x_j}[(\nu+\frac{\nu_t}{\sigma\varepsilon})h\frac{\partial \varepsilon}{\partial x}]+hc_{1\varepsilon}^*\frac{\varepsilon}{k}P_k+hP_{\varepsilon v}-hc_{2\varepsilon}\frac{\varepsilon^2}{k} \quad (11)$$

$$c_\mu=0.0845,c_{1\varepsilon}^*=c_{1\varepsilon}-\frac{\eta(1-\frac{\eta}{\eta_0})}{1+\beta\eta^3},c_{1\varepsilon}=1.68,\sigma_k=1.39,\beta=0.0$$

$$\eta=(2E_{ij}.E_{ij})^{1/2}\frac{k}{\varepsilon},\eta_0=4.377 \quad (12)$$

Only constant β is adjustable, high levels of turbulent data are obtained near-wall. All other constants are calculated explicitly as part of the RNG process.

$$\frac{\partial hk}{\partial t}+\frac{\partial U_j hk}{\partial x_j}=\frac{\partial}{\partial x_j}[(\nu+\frac{\nu_t}{\sigma_k})h\frac{\partial k}{\partial x}]+P_k+P_b-h\varepsilon \quad (13)$$

$$\frac{\partial h\varepsilon}{\partial t}+\frac{\partial U_j h\varepsilon}{\partial x_j}=\frac{\partial}{\partial x_j}[(\nu+\frac{\nu_t}{\sigma\varepsilon})h\frac{\partial \varepsilon}{\partial x}]+hc_{1\varepsilon}\frac{\varepsilon}{k}P_k+hc_1S_\varepsilon-hc_2\frac{\varepsilon^2}{k+\sqrt{\nu\varepsilon}}+S_\varepsilon \quad (14)$$

$$c_1 = Max[0.43, \frac{\eta}{\eta+s}], \eta = s\frac{k}{\varepsilon}, s = \sqrt{2s_{ij}s_{ij}}, \mu_t = hc_\mu \frac{k^2}{\varepsilon}, P_k = -\rho\overline{u_i'u_j'}\frac{\partial u_j}{\partial x_i'},$$

$$P_k = \mu_t s^2, P_b = \beta g_i \frac{\mu_t}{\Pr_t}\frac{\partial T}{\partial x_i}, \mu_t = \rho c_\mu \frac{k^2}{\varepsilon}, c_\mu = \frac{1}{A_0 + A_s\frac{KU^*}{\varepsilon}}, U^* = \sqrt{s_{ij}s_{ij} + \overline{\Omega_{ij}}\,\overline{\Omega_{ij}}}, \quad (15)$$

$$\overline{\Omega_{ij}} = \Omega_{ij} - \varepsilon_{ijk}\omega_k, A_0 = 4.04, A_s = \sqrt{6}\cos\Phi, \Phi = \frac{1}{3}\cos^{-1}(\sqrt{6}\omega), \omega = \frac{s_{ij}s_{jk}s_{ki}}{\tilde{s}^3}, \tilde{s} = \sqrt{s_{ij}s_{ij}},$$

$$s_{ij} = \frac{1}{2}(\frac{\partial u_j}{\partial x_i} + \frac{\partial u_i}{\partial x_j}), c_{1\varepsilon} = 1.44, c_2 = 1.9, \sigma_k = 1, \sigma_\varepsilon = 1.2, \beta = -\frac{1}{\rho}(\frac{\partial P}{\partial T})p, \Pr_t = 0.85$$

WillCox, turbulence model k-ω (standard) equation to be provided as follows: (WillCox, 1988):

$$\frac{\partial k}{\partial t} + U_j\frac{\partial k}{\partial x_j} = \tau_{ij}\frac{\partial U_i}{\partial x_j} - \beta^* k\omega + \frac{\partial}{\partial x_j}[(\nu + \sigma^*\nu_T)\frac{\partial k}{\partial x_j}] \quad (16)$$

$$\frac{\partial \omega}{\partial t} + U_j\frac{\partial \omega}{\partial x_j} = \alpha\frac{\omega}{k}\tau_{ij}\frac{\partial U_i}{\partial x_j} - \beta\omega^2 k\omega + \frac{\partial}{\partial x_j}[(\nu + \sigma\nu_T)\frac{\partial \omega}{\partial x_j}] \quad (17)$$

$$\frac{\partial k}{\partial t} + U_j\frac{\partial k}{\partial x_j} = \tau_{ij}\frac{\partial U_i}{\partial x_j} - \beta^* k\omega + \frac{\partial}{\partial x_j}[(\nu + \sigma^*\nu_T)\frac{\partial k}{\partial x_j}]$$

$$\nu_t = \frac{k}{\omega}, \alpha = \frac{5}{9}, \beta = \frac{3}{40}, \beta^* = \frac{9}{100}, \sigma = \frac{1}{2}, \varepsilon = \beta^*\omega k$$

3. Numerical Model

The values of the physical properties of water are considered as a default respectively, for density, viscosity, heat capacity and thermal conductivity. Solutions of all governing equations are subject to assignment of variables correctly in the boundary nodes. In steady state problems required only boundary condition but in unsteady state problems is required the initial conditions for all nodes in the network. Common boundary conditions in hydraulic issues include (Soltani and Rahimi Asl, 2003):

A- Inlet boundary condition: numerical models can fit the model by means of the various boundary conditions such as velocity, mass flow, etc. For example, in modeling of flow inside a closed or open channel can be used velocity inlet as input boundary condition.

B- The outlet boundary condition is considered pressure outlet equals the atmospheric pressure. If the output is chosen at a far distance from geometric constraints, and no change in direction of flow then the flow state is developed full. Using this model is caused the output surface is perpendicular to the flow and gradient is zero in the perpendicular direction on the output surface (Soltani and Rahimi Asl, 2003).

C - Wall boundary condition: the wall boundary condition is used to limit the area of between fluid and solid. The model is ready for simulation by Solutions set and defining the model. The following steps show the simulation process (Versteeg and Malalasekera, 2007): selection methods of discretization equation: In this paper first order upstream difference method is used for discretization of momentum, k, ε and ω equations and the standard method is used to find the pressure. Selection methods of the relation velocity - Pressure: this step is only be studied segregated. In this paper is used from SIMPLE method for velocity - pressure coupling. Determine the discount factors: the discount factor values are used for control of calculated variables in the each iteration. In this paper, the default values are used respectively for the pressure, density, momentum, k, ε and turbulent viscosity. In this paper, the initial values of the relative pressure is considered zero And the initial values of velocity components close to the average values presented in the input stream. By completing the steps in the numerical model, we can start the introduced process of problem by defining of repeat process. The frequency of reporting of results can be introduced before computing the numerical model. During solution process can be seen convergence of solution by the control of residues, integral of surface, statistics and values of the force. After finishing solution the computation of the unknown quantities and the results can be calculated at any point of the field and can be displayed by vector in the form, contour and profile views (Versteeg and Malalasekera, 2007). In this paper for solution of flow is usually introduced initial number repeat 1000 with report of every step of the calculation that conditions for convergence of the unknown parameters were satisfied after 300 to 350 iterations.

The dimensions of the Waal river in the Netherlands are not sufficient for the development of inland waterways, so it must be enlarged to increase the shipping capacity. In the middle part of the Vaal river between Nijmegen and Tiel, the extension of the handles in long and straight spans is an option. But in the bends of the upstream and downstream areas of the river, due to the difference in morphological and hydraulic processes (spiral flow), a different solution is needed. The Dutch Ministry of Public Works commissioned Haskoning to prepare a preliminary design to improve the width of the navigable part of the channel in one of the bends of the river through

the use of submerged fins. Submerged fins are thin slabs or wing-shaped walls that are installed on the stream bed in a river. And they usually have an angle with the main flow direction. When placed at the optimal angle, submerged vanes produce an anti-helix flow that reduces, or even possibly completely eliminates, the natural secondary flow in river bends. This is why the sediment flow, which is originally pushed towards the inner bank of the bend, is changed and directed to the opposite side. Therefore, it will improve sedimentation on the outer shore of the bend and washing water on the inner shore of the bend.

Figure 1- Map of navigable rivers in the Netherlands and the location of the Waal river in it.

Figure 2- The picture of the Waal river and the vertical breakwater structures in the outer arch and the middle wall in its inner arch

In this research, version 16/3/2 of Gambit software is used to generate its geometry and grid. The grid pattern is made of Quad element and map type is used for pages. The available boundary conditions are the velocity input from the left side from the top of the arc and the pressure output boundary condition at the bottom of the arc. The simulation results can be seen in Figures 3 to ۱۱.

4. Results and Discussions

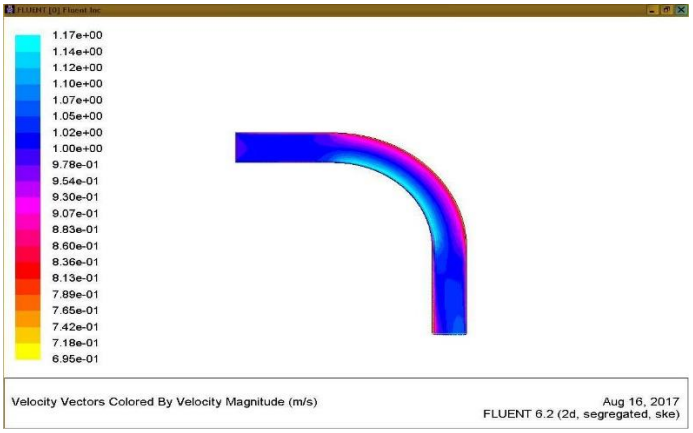

Figure 3- Velocity curve, meters per second, in a 90-degree arc with a width of 350 meters and a water height of 4.5 meters. K- ε perturbation model is used. The results show that the velocity values in the inner arc obtained from the numerical model in the state without the presence of coastal protection structures immediately after the end of the straight path of the channel and at the beginning of the inner arc equal to 1.17 m/s and in the outer arc equal to 8.13 meters per second.

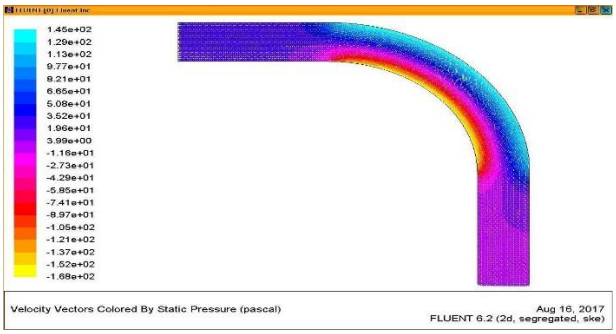

Figure 4- Isometric pressure curve in terms of pascal, in a 90 degree arc with a width of 350 meters and a water height of 4.5 meters. K- ε perturbation model is used. The results show that the amount of negative pressure in the inner arc obtained from the numerical model in the absence of coastal protection structures immediately after the end of the straight path of the channel and at the beginning of the inner arc equals -1.68e+2 pascal and the positive pressure in the outer arc equals It is 1.45e+2 pascal. In the inner arc, the sedimentation potential is higher and in the outer arc, due to the positive hydrostatic forces, the erosion potential is higher.

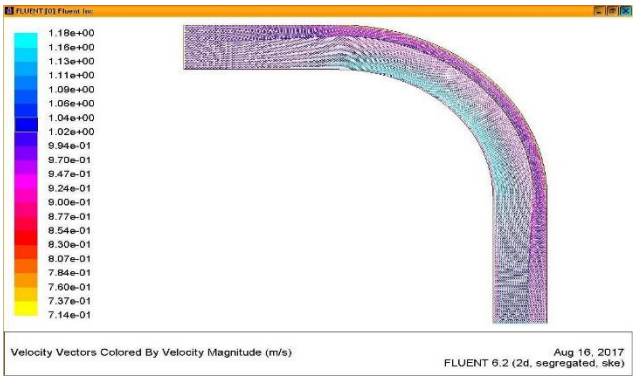

Figure 5- Isometric curve, meters per second, in a 90-degree arc with a width of 350 meters and a water height of 4.5 meters. K- ε perturbation model is used. The results show that the velocity values in the inner arc obtained from the numerical model in the presence of the arc vane in a quarter of the width near the outer arc of the coast immediately after the end of the straight path of the channel and at the beginning of the inner arc, equal to 1.18 m/s and in the arc External is equal to 8.77 meters per second. Compared to the state without this structure, there was not much change

.

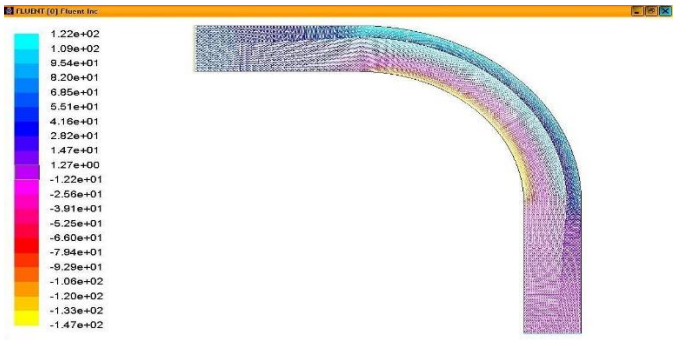

Figure 6- Isometric curve in terms of pascal, in a 90 degree arc with a width of 350 meters and a water height of 4.5 meters. K- ε perturbation model is used. The results show that the amount of negative pressure in the inner arch obtained from the numerical model in the presence of the arch vane in a quarter of the width near the outer arch of the coast immediately after the end of the straight path of the channel and at the beginning of the inner arch, is equal to -1.68e+2 pascal and the pressure Positive in the outer arc is equal to 1.45e+2 pascal. In the inner arc, the sedimentation potential is higher and in the outer arc, due to the positive hydrostatic forces, the erosion potential is higher. Compared to the state without this structure, there was not much change.

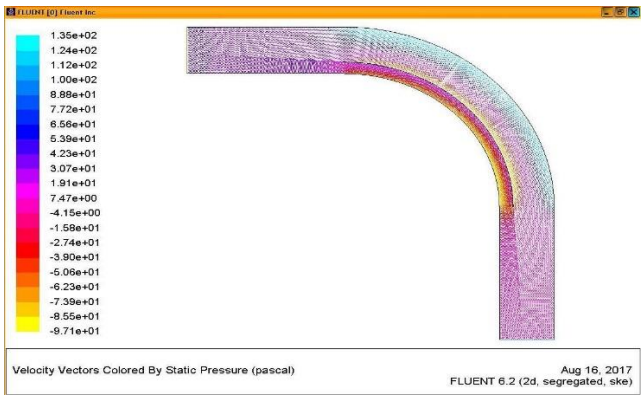

Figure٧ - Isometric curve in terms of pascal, in a 90 degree arc with a width of 350 meters and a water height of 4.5 meters. K- ε perturbation model is used. The results show that the amount of negative pressure in the inner arch obtained from the numerical model in the presence of the arch vane in a quarter of the width near the inner arch of the beaches immediately after the end of the straight path of the channel and at the beginning of the inner arch, is equal to -9.71e+1 pascal and the pressure Positive in the outer arc is equal to 1.355e+2 pascal. In the inner arc, the sedimentation potential is higher and in the outer arc, due to the positive hydrostatic forces, the erosion potential is higher. Compared to the case without this structure, the negative pressure change in the inner arch is reduced.

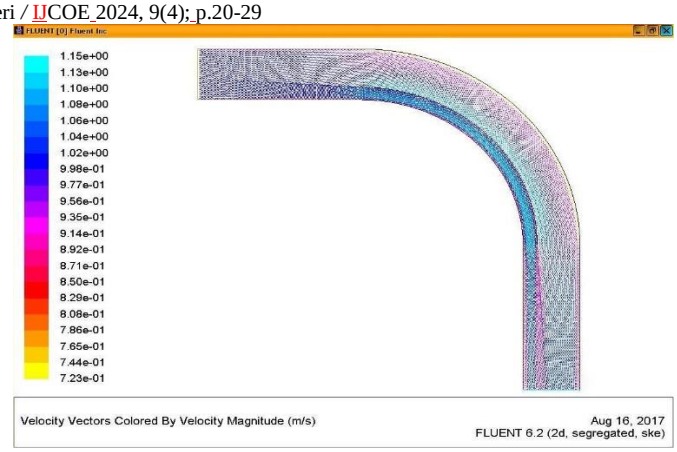

Figure ٨-- Isometric curve, meters per second, in a 90-degree arc with a width of 350 meters and a water height of 4.5 meters. K- ε perturbation model is used. The results show that the velocity values in the inner arc obtained from the numerical model in the presence of the arc vane in a quarter of the width near the inner arc of the beaches immediately after the end of the straight path of the channel and at the beginning of the inner arc, equal to 0.1 m/s and in the arc External is equal to 5.8 meters per second. Compared to the case without this structure, the speed has decreased near the inner arc .The maximum speed was transferred from the inner arc to the middle part. In this way, the amount of negative pressure was reduced and the sedimentation potential was also reduced

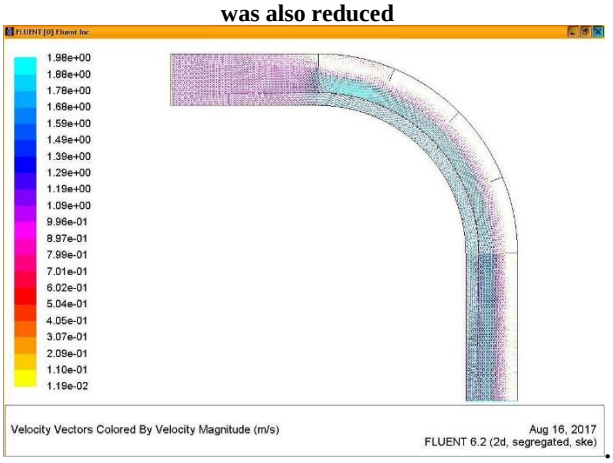

Figure ٩- Isometric curve, meters per second, in an arc of 90 degrees with a width of 350 meters and a water height of 4.5 meters. K- ε perturbation model is used. The results show that the velocity values in the inner arc obtained from the numerical model in the presence of vertical breakwaters in the outer arc along with the arc vane in a quarter of the width near the inner arc of the beaches immediately after the end of the straight path of the channel and at the beginning of the inner arc, equal to ١. ٦٨ m/s and in the outer arc is equal to 7.99 m/s. Compared to the case without this structure, the speed has decreased near the inner arc. The maximum speed was transferred from the inner arc to the middle part. In this way, the amount of negative pressure was reduced and the sedimentation potential was also reduced. Reducing the speed in the areas between the breakwaters also prevents scouring of this area.

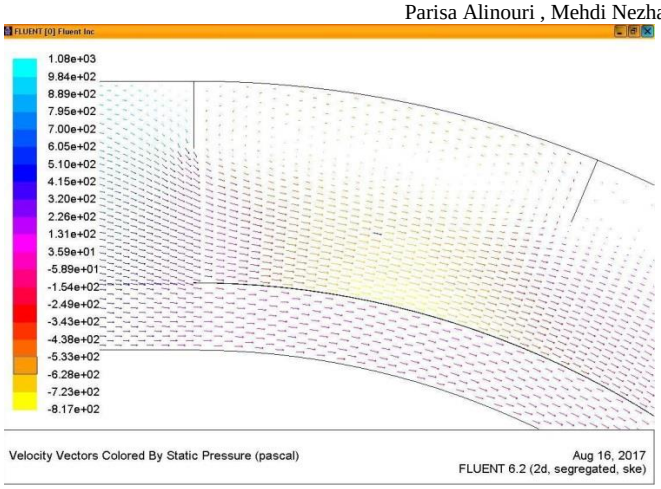

Figure ١٠- isopressure curve in pascal, in a 90 degree arc with a width of 350 meters and a water height of 4.5 meters. K- ε perturbation model is used. The results show that the amount of negative pressure in the outer arch obtained from the numerical model in the presence of vertical breakwaters in the outer arch along with the arch vane between the breakwaters is equal to -8.17e+2 pascals and the positive pressure in the inner arch is equal to 1.31e+2 pascals. Before the construction of protective structures, the potential for sedimentation is higher in the inner arch and the erosion potential is higher in the outer arch due to the positive hydrostatic forces. Compared to the state without these structures, the negative pressure change in the inner arch disappeared and became negative pressure in the outer arch in the space between the breakwaters. In this way, the balance of the navigable river bed was established in the internal and external arcs.

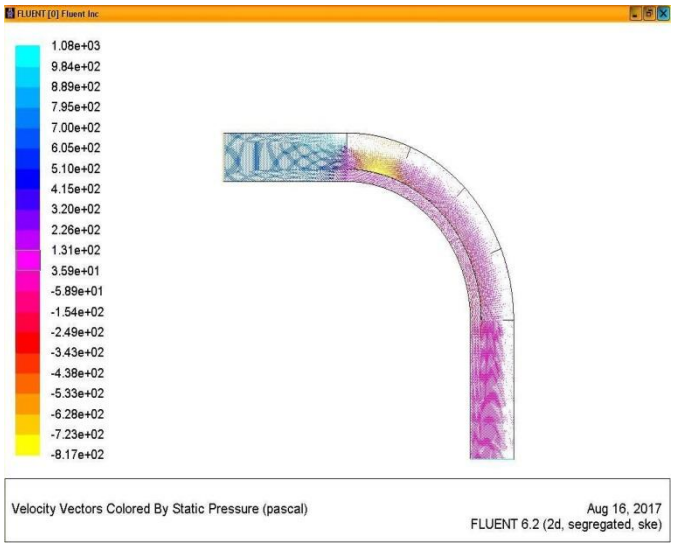

Figure ١١- isopressure curve in pascal, in a 90 degree arc with a width of 350 meters and a water height of 4.5 meters. K- ε perturbation model is used. The results show that the amount of negative pressure in the outer arch obtained from the numerical model in the presence of vertical breakwaters in the outer arch along with the arch vane between the breakwaters is equal to -8.17e+2 pascals and the positive pressure in the inner arch is equal to 1.31e+2 pascals. Before the construction of protective structures, the potential for sedimentation is higher in the inner arch and the erosion potential is higher in the outer arch due to the positive hydrostatic forces. Compared to the state without these structures, the negative pressure change in the inner arch disappeared and became negative pressure in the outer arch in the space between the breakwaters. In this way, the balance of the navigable river bed was established in the internal and external arcs.

5. Conclusions

For the purpose of a case study in the Netherlands, a numerical study of the effect of using submersible vanes along with vertical breakwaters in the protection of the banks of the Waal River in the Netherlands was used from field data. In the present research, the effect of a series of non-submersible breakwaters with 5 placement angles (vertical breakwaters) is numerically investigated, relative to the outer wall of the arch with a length of 25% of the channel width (87.5 meters) and with a distance of 529.875 meters from each other along with a submerged vane in The distance of a quarter of the width from the inner arc to the full length of the 90 degree arc, the distribution of average speed and pressure in the 90 degree arc with a width of 350 meters and a water depth of 4.5 meters was studied. The results of the study showed that the presence of a series of breakwaters causes the uniformity of the upstream speed and the transfer of the high-speed area from the vicinity of the outer wall to the middle of the channel to the inner wall. If the breakwaters are placed in the outer arch along with the submerged blade close to the inner arch at a distance of a quarter of the width, they produce an anti-helix flow which reduces the natural secondary flow in the bends of the river. Therefore, the high-speed current, which is originally pushed towards the inner bank of the bend, is changed and directed to the middle side. Therefore, it will improve sedimentation on the inner shore of the bend and washing water on the outer shore of the bend. In this way, the flow speed reaches from an average value of 1 m/s to a value of 1.98 m/s in the middle part, and sedimentation is reduced in this area, and the potential of sedimentation is reduced by reducing the speed in a quarter of the width near the inner arch. and external increases. According to the results, the speed in the vicinity of the inner shore of the arch is greatly reduced and the placement of breakwaters causes the dispersion and transfer of the high-velocity area from the inner wall to the middle of the channel. The main reason for the sedimentation of the inner coast of the arc is the concentration of areas with negative pressure in the inner arc, which creates a secondary flow and causes a swirling flow and sedimentation in this area. As it can be seen, the placement of the submerged vane with the same length as the arch near the inner arch along with the breakwaters in the outer arch has prevented the formation of these

areas. Due to the speed changes in the vicinity of the breakwaters, the speed has changed and high velocities have been placed at a short distance from the breakwaters. This shows that protecting the nose of breakwaters is inevitable in order to maintain the stability of the breakwater structure.

3. References

1. Qodsian, M.. 2018 final report on scouring, sedimentation and flow pattern around the breakwater in the 90 degree arc. Iran Water Resources Management Joint Stock Company.
2. Tingsanchali, T. and S Maheswaran, 1990. 2-d depth-averaged flow computation near groyne. Journal of Hydraulic Engineering, 116(1): 71-86.
3. Giri, S. Shimizu, Y. and B Surajata, B. 2004. Laboratory measurement and numerical simulation of flow and turbulence in a meandering-like flume with spurs. Flow Measurement and Instrumentation, 15: 301-309.
4. Abad, J. D. and B. L Rhoalds, 2008. Flow structure at different stages in a meander-bend with bend way weirs. Journal of Hydraulic Engineering. 134(8): 1052-1063.
5. Duan, J. He, Li. Fu, X. and Q Wang, 2009. Mean flow and turbulence around experimental spur dike. Advances in Water Resources, 32(12): 1717-1725.
6. Van den Heever, A. 2013. An Investigation of the use of groynes as a means of riverbank erosion protection. M.Sc. Thesis, Department of Civil Engineering, Stellenbosch University, South Africa.
7. Qodsian, M., Waqfi, M. van Panahpour 1387. Laboratory investigation of the two-dimensional flow pattern around the breakwater in a 90 degree arc. Journal of Agricultural Sciences and Natural Resources, 15 (4): 269-282.
8. Fazli, M. Waqfi, M. and Qudsian, M. 2018. Review and comparison of shear stress calculation methods in arched channels. Proceedings of the 8th International Congress of Civil Engineering, Shiraz University, Shiraz.
9. Shaker, A. and Kashfipour, M. 2012. Laboratory investigation of the effect of the length and placement angle of rectangular breakwaters on the distribution of speed and shear stress in a 90 degree arc, Scientific and Research Journal of Irrigation Science and Engineering. Article 1, Volume 38, Number 3.
10. Salehi Nishabouri, S.A.A. and Nasiri Saleh, F, (translators). 2017. Reddy, Wolfgang, (1979), "Disturbance models and their application in hydraulics", Publications of Water Engineering Research School, Tarbiat Modares University, Tehran.
11. Shojaifard, M.J. and Noorpar Hashtroudi, AS (translators). 1379. Versteeg, H.K. and Mallalaskara, (1995), "Introduction to Computational Fluid Dynamics", Iran University of Science and Technology Publications, Tehran.
12. Launder, B. E. and Spalding, D. B. (1974). The Numerical computation of turbulen flows, comput. Methods Appl. Mech. Eng., Vol. 3, pp. 269-289.
13. Tennekes, H, and Lumley, J. L. (1972). A first course in turbulence, MIT Pres Cambridge, MA.
14. Ouillon, S., and Dartus, D. (1997), Three-dimensional computation of flow around groyne, Journal of Hydraulic Engineering, ASCE, 123(11), pp. 962-970.

15. Patankar, S.V. (1980), Numerical heat transfer and fluid flow. Mc Graw- Hill Book Company, New York.
16. Peng, J., Tamai, N., Kawahara, Y., and Huang, G. W. (1999), Numerical modeling of local around spur dikes, 28th IAHR congress, Graz, Austria.
17. Rodi, W. (1984), Turbulence models and their application in hydraulic. State- of- the art paper, IAHR Experimental and Mathematical Fluid Dynamics.
18. Reynolds, O., 1984. On the dynamical theory of incompressible viscous fluids and the determination of the criterion. Phil. Trans. Roy. Soc. London, 123- 161.
19. McGurik, J.J. and Rodi, W., 1978. A depth-averaged mathematical model for the near fluid of side discharge into open- channel flow. Journal of Fluid Mechanics, 864, 761-781.
20. Keller, R.J. and Rodi, W., 1988. Prediction of flow characteristics in main channel/floodplain flows. Journal of Hydraulic Research, IAHR, 26(4), 425- 441.
21. Biglari, B. and Sturm, T.W., 1998. Numerical modeling of flow around bridge abutments in compound channel. Journal of Hydraulic Engineering, ASCE, 124(2), 156-163.
22. Gibson, M.M. and Launder, B.E., 1978. Ground effects on pressure fluctuations in the atmospheric boundary layers. Journal of Fluid Mechanics, 86, 491- 511.
23. Rastogi A. K. and Rodi, W., 1978. Prediction of heat and mass transfer in open channels. Journal of Hydraulics Division, ASCE, 104(3), 397- 420.
24. Yakhot V., Orszag S.A., Thangam, S., Gatski, T.B. and speziale, C.G., 1992. Development of turbulence models for shear flows by a double expansion technique. Physics of Fluids A, Vol. 4, No. 7, pp1510-1520.
25. Wilcox D.C., 1988. Re-assessment of the scale-determining equation for advanced turbulence models. AIAA Journal, vol. 26, pp. 1414- 1421.
26. Versteeg, H.K. and Malalasekera, W., 2007. An Introduction to Computational Fluid Dynamics: The Finite Volume Method, Prentice Hall, Feb 16, 503 pages.
27. Soltani, M.V. and Rahimi Asl, R., 2003. Computational fluid dynamics by Fluent software, Tehran, Tarrah issues.
28. Fluent 6.2 User's Guide, Janurary 2005.
29. Gambit 2.2 User's Guide, September 2004.

INTERNATIONAL JOURNAL OF
COASTAL, OFFSHORE & ENVIRONMENTAL ENGINEERING
IJCOE Vol.9/No. 4/Autumn 2024 (30- 41)

Available online at: www. Ijcoe.org

Investigating spectral and experimental methods in predicting wind waves in the southern regions of Iran (case study: Asalouye port)

Homayoon Ahmadvand[1*], Ali Sheykh bahai[2], Amer Kaabi[3], Dariush Abolfathi

*1- *PhD in Marine Physics, Khorramshahr University of Marine Sciences and Technology, Iran*
2- Responsible director of the International Quarterly Journal of Coastal and Offshore Engineering
3- Petroleum University of Technology, Department of Basic Sciences and Language (Abadan)
4- Assistant Professor, Payam Noor University, Department of Natural Geography

ARTICLE INFO

Article History:
Received: 15 Jun 2024
Accepted: 15 Oct 2024

Keywords:
wind waves
duration
significant wave height
wave spectrum

ABSTRACT

sea level rise due to wind are one of the most important phenomena in marine environments that are effective in the coastal and offshore processes. This paper discusses methods to evaluate the accuracy of experimental and spectral methods in predicting wind waves in Asaluyeh port. Empirical methods including SMB, SPM, CEM and Jonswap and Spectral methods include Bretschneider, Mitsuyasu, Pierson-Moskowitz, Jonswap, ISSC spectrum were considered to evaluted the mentioned waves. The results show that Jonswap method among experimental methods in duration of 6 hours is the most appropriate method to determine the wave profile in Asaloyeh port. Furthermore by comparing spectral methods it was found the Bretschneider, Mitsuyasu and Pierson-Moskowitz spectrum show lowest error in the calculation of H_{m0} nd f_p. To better match the measured spectra, their coefficients were corrected and after height value was calculated using each spectrum. Then, using corrected and uncorrected spectra, directional spectra of the region were plotted.

1. Introduction

The presence of waves caused by wind and sea level rise near the coastal strip can be effective in increasing the energy of coastal waves. Especially in areas where root and tidal waves are also present in these areas [1]. Recently, various methods have been used to obtain the values of the significant wave height and the wave period as characteristics of the wave energy base on real data observation [2]. Raj N and et al, predicted significant wave height for sustainable wave energy [3]. Hashemi and shahidi Extracted of the significant wave height from synthetic HF radar data acquired on a floating platform [4]. Ardhuin and Carlo retracking of altimeter waveforms yields fluctuations in wave height and sea level. The result shows that Retracking of altimeter waveforms yields fluctuations in wave height and sea level, correlated at the scale of the effective footprint[5]. Accurate modelling of multimodal sea states is of primary importance for most of offshore and coastal activities, such as wave energy device optimization, maritime design practice and for safety at sea. Sartini and Antonini have researched spectral wave climate and wave systems analysis of the French Atlantic Ocean. Furthermore swell system and local topography are evaluated quantitatively on the whole area The results of this research have shown that the two-faceted shape of this region and the interruption of the seas in this region cause the change of the entire wave directional spectrum[6]. In the last 5 years, the experimental study of wave height , crest and the trough distribution of the directional irregular waves that are produced on a sloping surface have been studied [7]. In the ports of Iran, especially the southern ports of Iran, research has been done on waves and renewable energy, one of the sources of which is wind [8]. Goharnejad et all evaluated the energy of waves in the Persian Gulf under the influence of the region's climate [9]. Furthermore Vafaeipour Sorkhabi et al investigated the behavior of quay walls under random waves through experimental methods. The study used walls with vertical geometrical form, which were exposed to sea random waves under the JONSWAP spectrum. A neural network model was developed using the feedforward method with the backpropagation algorithm to analyze the time series of water surface level and strain[10].

Waves caused by the wind in the coastal strip can affect the fish and aquatic environment[11,12].

Considering that fish and marine animals are caught on the shores of Asalouye port, and also the relationship between weather conditions and the height of strong sea waves [13], therefore, in this research, it is supposed to predict local and online wind waves in this area using experimental models and Suggested spectrum.

In addition, according to the breakwaters built in Asalouye port and the necessary measures to repair or maintain them, it is necessary to access the statistics of the waves recorded in that area, so in terms of the engineering principles of marine structures, it is necessary to investigate and analyze the spectrum of these types of waves[14]. Lee et al studied joint Probability Distribution of Significant Wave Height and Peak Wave Period Using Gaussian Copula Method [15]. Therefore, the study of the index wave period is still one of the important topics in marine science and engineering studies.

Considering the numerous offshore and onshore constructions, drillings and oil and gas platforms in the region, the demand for a reliable metocean forecast system has highly increased in recent years. For methods of forecasting SMB, SPM, CEM and Jonswap methods can be noted. In each of these methods by comparing of tmin with wind duration, continuous time limit or fetch limited condition was determined, then the values Hm0 and TP were obtained. In particular, Jonswap, Pierson-Moskowitz, Mitsuyasu and Bretschneider and ISSC spectral methods can be cited which using the calculated spectral parameters m0, m2 and m4 of every one of them, Hm0, H1/10 , Tz and Tc and Tp parameters are calculated [16,17].

Mohammad Pakhirehzan, et al, The numerical study of winter shamal wind forcing on the surface currents and the wave field in Bushehr Offshore using MIKE21 model [18]. The significant wave height and wave propagation speed for the period of Winter Shamal Wind in comparison with the days prior to the wind show significant changes.

The latest research from the study of the wave that has been published on the topic of the wave goes back to the article of Wang et all. In this study, the Assimilating wave spectrum and wave height Assimilation based on from satellite observations have been investigated and compared. When comparing with the buoy measurements, spectrum assimilation demonstrated superior effectiveness in improving mean wave period (MWP) compared to SWH assimilation [19]. Ahmadvand et al used empirical and spectral methods in predicting wind wave characteristics in Amir Abad port [20]. Stanislav Kotaška studied the spectral analysis and empirical formulaof wind wave parameters of Haline water resources under limited wavelength conditions [21]. This means, the proposed methods in this research, which include experimental and spectral methods, are not obsolete yet. Therefore, in this research according to the climate changes of a region, this issue has been re-examined.

In the following, the coefficients of the spectral models were corrected and the directional spectrum of this port was calculated and drawn using the effective spectrum in this area. In no other research, the directional spectrum of wind waves in Asalouye port has not been investigated.

2.Material and methods

2.1. Empirical methods of wave prediction

A simple method to predict the parameters waves are using by empirical relationships. These methods which are provided based on dimensional analysis, generally, calculate the significant wave height and peak periods based on input parameters such as wind speed, wind direction, duration. In Table 1 some of theses methods mentioned. In the following we will refer to these relations (It is mentioned in the appendix)

- In all methods if the actual time is greater than tmin, Wave growth, is limited by the fetch and based on relations at the last column of the table, wave height and period (Ts and Hs) values can be calculated. In SMB method when the real duration is smaller than the tmin, limited duration condition dominates and equation (1) used to determine the effective fetch [22].

$$X = \frac{U^2}{g} exp\left(\frac{1.76A - 0.369 - \sqrt{0.084A^2 - 1.3A + 6.776}}{1.51} \right)$$

$$A = \ln t - \ln\left(6.59 \frac{U}{g} \right)$$

(1,2)

- In the SPM method, wind stress1 is related directly to the wave growth. To determine the vertical profile of wind stress and hence wind speed, differences in air-water temperature, sea surface roughness and friction velocity should be considered. All of these factors with wind stress UA are taken into account by SPM and its value is calculated according to the following equation [16].

$$U_A = 0.71 U_{10}^{1.23}$$

(3)

- In the CEM method, wind shear speed u* is in meters per second and is calculated from following equation [17].

$$u_* = U_{10} \{ 0.001 (1.1 + 0.035 U_{10}) \}^{0.5}$$

(4)

In the CEM method if the duration limited condition dominates, for the computation of the equivalent fetch, equation (4) is used.

$$\frac{gX}{u_*^2} = 5.23 \times 10^{-3} \left(\frac{gt}{u_*} \right)^{\frac{3}{2}}$$

(5)

[1] - U_A

In SMB and Jonswap methods for calculation of the effective fetch, a limited region within ± 45 on each side of main wind direction should be considered that consist of 15 radials from the wave station at intervals of 6 degrees, and extending until they first intersect the shoreline. The component of length radial in a direction parallel to the wind direction is measured. The effective fetch is calculated from weighted average of length of radials using following equation [22]:

$$X = \frac{\sum X_i \cos\theta_i}{\sum \cos\theta_i}$$

(6)

While X_i is the length of each radial and θ_i is the angle of each of each radial. In SPM and CEM methods for calculation of the effective fetch, a limited region within ±15° relative to the main wind direction is considered.

2.2. Wave spectrum

The power spectral density represents the effect of frequency on the signal's power [23]. The spectrum of a signal can be viewed as a function that tells us what portion of the power is carried by what frequency components – it is a function of the spectral power density. In general, for a frequency spectrum equation (9) is presented. A and B are regulator of the shape and spectrum scale parameters respectively and can be defined as a producer function of wave, wave height and wave period.

$$E = \frac{A}{f^5} exp\left(-\frac{B}{f^4}\right)$$

(7)

In the past decade based on data collected and analysis conducted, spectrum for several different conditions are presented. In Table 2 refers to a number of them [24, 25] (table is in Appendix). One of the important methods for determining the profile of the wave spectrum is the use of spectral moment. The spectral parameters H_{m0} and T_p can be (8) to (9) achieved.

$$H_{mo} = 4\sqrt{m_o}$$

(8)

$$T_p = f_p^{-1}$$

(9)

In the above relationships H_{m0} and T_p are wave height and peak period.

2.3. Directional spectrum

the directional wave spectrum applied for separating wind sea and swell from directional wave spectra in finite-depth waters [26]. So use of directional wave spectrum in the advanced models is essential. Wave models are often one-dimensional directional models modified by a function of frequency and the wave direction.

$$E(f,\theta) = E(f)G(f,\theta)$$

(10)

E(f,θ) is directional spectrum, E(f) is frequency spectrum and G(f,θ) is non-dimensional spreading function. Since the modified frequency spectrum to the directional spectrum does not change the total energy density, the following relationship is established:

$$\int_{-\pi}^{\pi} G(f,\theta)d\theta = 1$$

(11)

$$m_o = \int_0^{\infty}\int_{-\pi}^{\pi} E(f,\theta)d\theta\, df$$

(12)

θ usually is clockwise its origin considered to be zero in direction of dominant wind and its practical range is from $-\pi/2$ to $\pi/2$. Based on wave data analysis and theoretical analysis, several publications related to the directional spreading function $G(f,\theta)$ provided. One of the relationships is PNJ and the formula is as follows [27]:

$$G(f,\theta) = G(\theta) = \begin{cases} \frac{\pi}{2}\cos^2\theta & |\theta| \le \frac{\pi}{2} \\ 0 & |\theta| > \frac{\pi}{2} \end{cases}$$

(13)

3. Study area

The study area is located in Asaloye region at the southern coast of Iran in the Persian Gulf (Fig. 1). Asaloyeh is an important economical region in the Persian Gulf because it is close to the Pars gas field and marine transportation activities. Wind and wave data were gathered by Iranian National Center for Oceanography (INCO), respectively. The recorded wave data was collected at $27^o49'94''$ and $52^o59'0''E$ and water depth at the wave station was about 25 m. The period of data collection was from 2002 to 2003. Statistics of wave and wind characteristics are indicated in Table 3. Table 3 shows that the average wind and wave directions are from the southeast and south directions, respectively.

Another important subject is the possible existence of swells. Since the Persian Gulf is a semi-enclosed sea, swells cannot easily propagate into it from the Indian Ocean due to the existence of Strait of Hormuz.

4- Result and discussion

4.1. predicting H_{m0} by experimental formula

In order to use the wave prediction equations, status of deep or shallow water has been verified. Therefore, using the ratio d/L= 8.41, were found that deep water conditions are prevailing. Also, using the relations listed in Table 1, and by assuming t= 6, 9 and 12 hours, results of calculations are shown in figures 2 to 5.

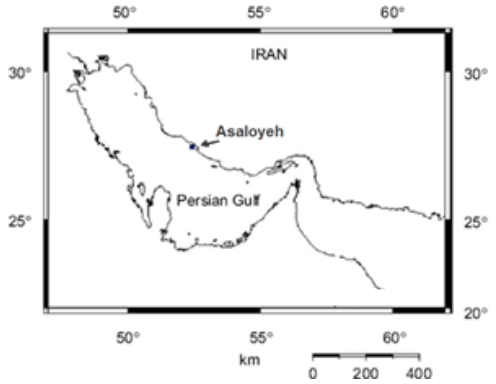

Fig. 1. Map of Persian Gulf at Asalouye port.

Table 3: Maximum, minimum and average values of the used data.

Parameters	Min	Average	Max
Significant wave height (m)	0.011	0.582	3.24
Wave direction (deg.)	37.91	258.3	349.2
Wave peak period (s)	1.845	4.32	7.37
Wind speed (m/s)	0.124	5.12	16.9
Wind direction (deg.)	0.255	228.9	359.9

Predicted values in each of the above methods, compare to the measured values are with error. Thus for compare and evaluate each of them, mean square root values are calculated in Table 4. Comparison between the calculated values of using Jonswap method for wind with of 6 hours duration showed maximum accuracy in estimation of wave height and period. The results showed that SMB and SPM method with duration of 12 hours calculate more

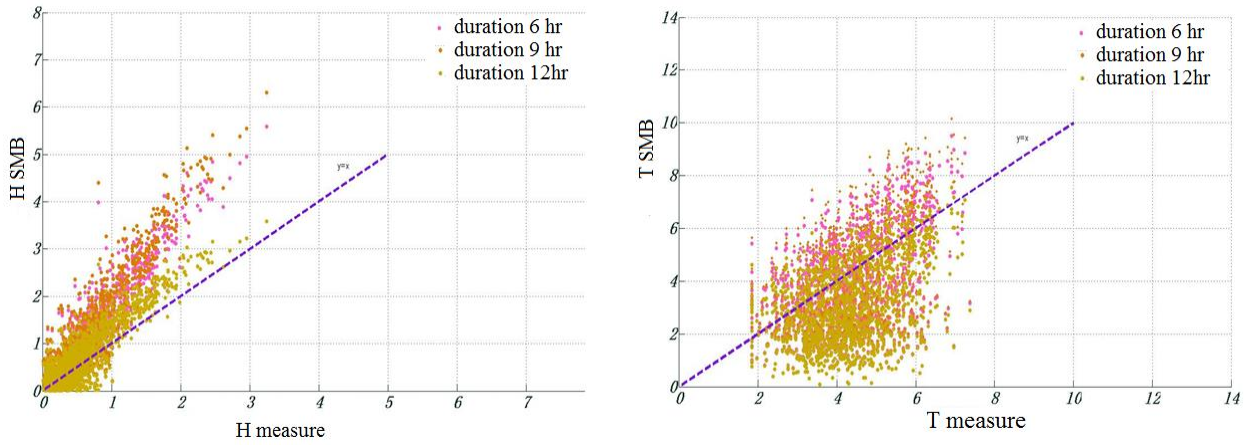

Figure 2: Comparison of measured and predicted values of wave height and period by using SMB formula

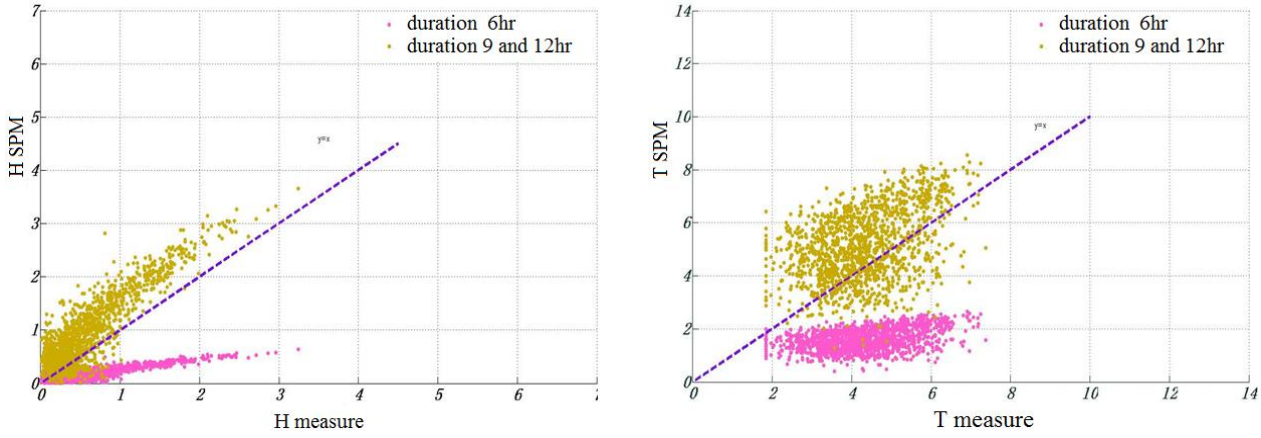

Figure 3: Comparison of measured and predicted values of wave height and period by using SPM formula

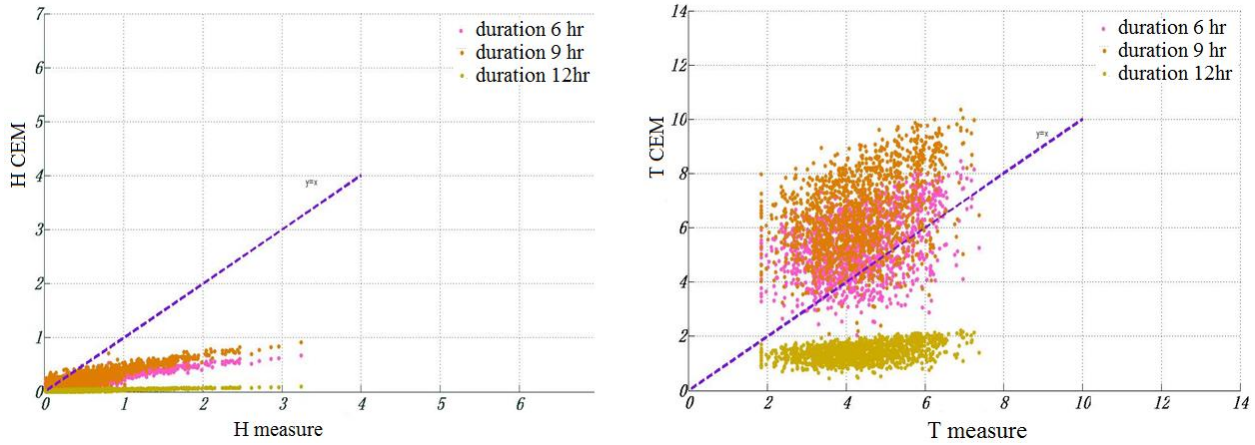

Figure 4: Comparison of measured and predicted values of wave height and period by using CEM formula

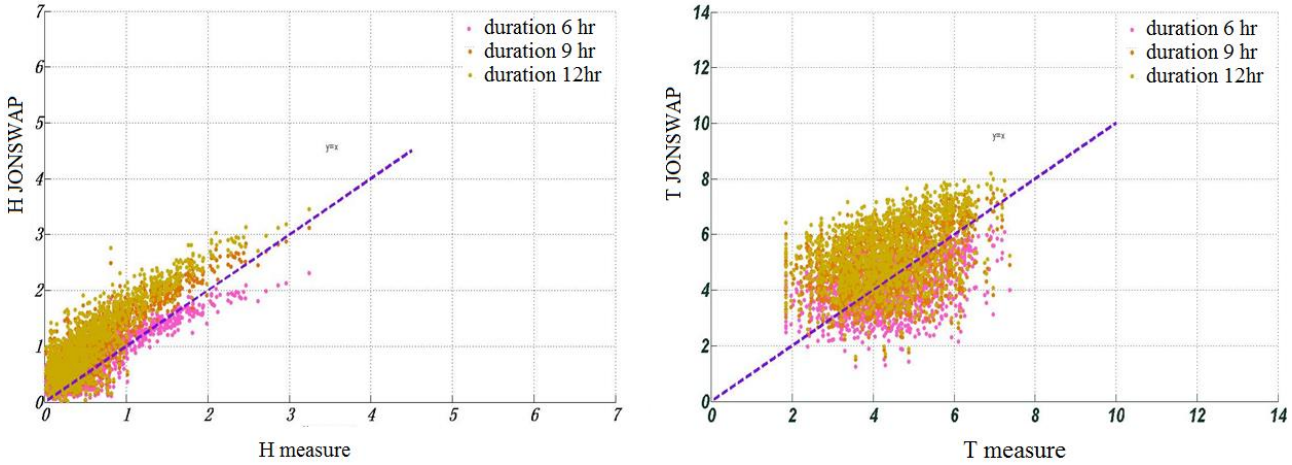

Figure 5: Comparison of measured and predicted values of wave height and period by using Jonswap formula

Table 4: Comparison of the mean square root values of Hs and Ts in experimental methods of wave prediction

		duration		
	parameter	***6hours***	***9hours***	***12hours***
SMB	H_s	87.77	100.16	45.53
	T_s	42.92	43.98	42.38
SPM	H_s	75.40	63.79	63.79
	T_s	65.08	34.30	43.30
Jons wap	H_s	44.99	68.39	73.89
	T_s	29.89	29.66	34.66
CEM	H_s	72.06	62.62	96.16
	T_s	35.59	57.80	69.21

accurate values of the wave height and period. While the Jonswap for 6 hours duration, predicts the wave height and period with the lowest error. In the CEM method for duration of 9 hours and 6 hours respectively, minimum error in the calculation of wave height and period will result. So with an overall view of the table we can say, Jonswap method with duration of 6 hours, show the least amount of error in calculating the wave height and period.

4.2. Spectral analysis of data

To plot the selected spectrum, first the Δf value calculated based on the frequency difference between maximum and minimum divided by number of data, And then adding Δf each time to minimum frequency, the frequency values and frequency spectral density values are calculated. Also for plotting the measured spectrum using the relationship S = a^2 / 2, S values for each data which expressed with specifications ai and fi can be plotted. In Figure (6) the spectra are plotted without fitting. As can be seen many fluctuations in the energy spectrum, but the location and maximum size has been determined to be appropriate. To reduce its volatility, the chart in the MATLAB software using the first order Gaussian fitted which which results is shown in the figure (7).

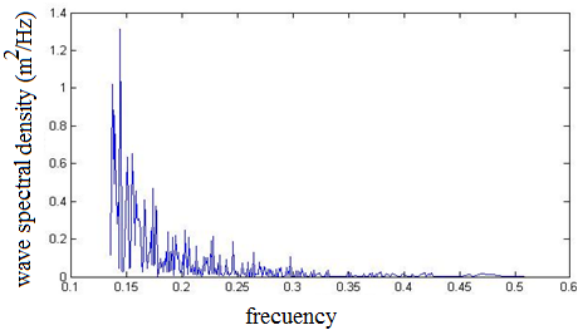

Figure 6: Spectrum of the measured data

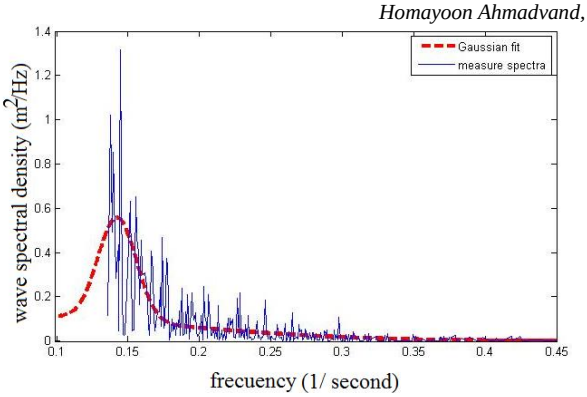

Figure 7: The fitted spectral density data

In order to compare each spectrum with the plotted spectra, Using Table 2, in the figure (8) spectrum are plotted and compared with the measured spectrum. It can be concluded that the spectra of the Pierson-Moskowitz and Bretschneider Mitsuyasu spectrum are closely fitted.

4.3. Comparison of the measured spectrum with selected spectra

For analyze and evaluate each of the spectra, we compared the calculated values of H_s with calculated value from measured spectrum. So that based on $H_{mo} = 4\sqrt{m_0}$ equation and assumption that in deep water $H_{mo} = H_s$ significant wave height of each of the Pierson-Moskowitz, Mitsuyasu and Bretschneider has been calculated. Also for calculation the H_s time series based on zero up-crossing spectrum is plotted. The values of the each frequency interval of measured spectrum in equation (20) have been replaced. The values of phase function chosen uniformly of a random number in the range of 0 to 2π (Figure 9).

$$\eta = \sum_{n=1}^{\infty} a_n \cos(w_n t + \varphi_n) \quad (13)$$

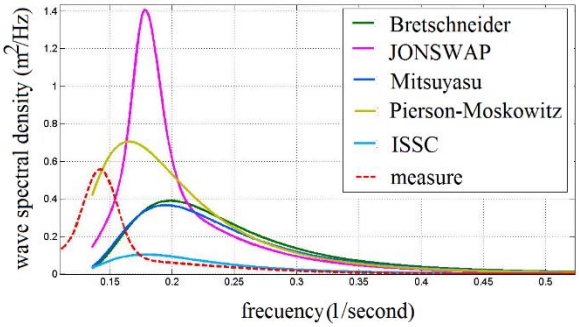

Figure 8: Comparison of spectral energy density of measured data with theoretical spectrum

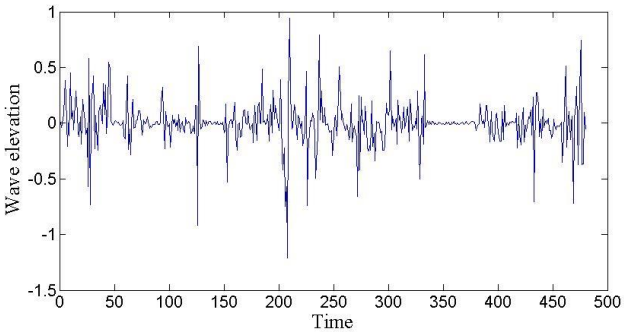

Figure 9: profile of the sea level using the values of wave height and frequency selected from measured spectra

Results using the mentioned methods listed in Table 5. The results show that Mitsuyasu and Pierson-Moskowitz spectrum predict the wave height with minimum and maximum error respectively,

Table 5: Comparison of calculated and measured Hs in Mitsuyasu - and Pierson Moskowitz and Bretschneider spectrum

Spectrum	Pierson-Moskowitz	Bretschneider	Mitsuyasu
Hs (m)	1.015	0.849	0.815
Error of measurement H_S (%)	35.57	13.39	8.5

4.4. Correction of spectral relations of Mitsuyasu, Pierson-Moskowitz and Bretschneider

Mazaheri et al have also shown that the wave coefficients can be modified and the use of modified wave coefficients can be used to express the wave behavior in the northern waters of the Persian Gulf with higher accuracy [28].

Pierson-Moskowitz, Bretschneider and Mitsuyasu spectra with little difference have the good agreement with measured spectra. In order to match and more consistentency of Pierson-Moskowitz, Mitsuyasu and Bretschneider spectrum by the measured spectrum, their relationship as shown in Table 6 was calibrated to improved the results. In Figure 10 and Table 7 the results of these corrections is shown.

Table 6: corrected spectral relations of Mitsuyasu, Pierson-Moskowitz and Bretschneider

spectrum	Spectrum relation	description

Pierson-Moskowitz	$S(f)=\frac{3.362}{16}H_s^2\ f_p\ f^{-5}\ exp\left(-\frac{5}{4}\left(\frac{f_p}{f}\right)^4\right)$	$T_p=1.65\overline{T}$
Mitsuyasu	$S(f)=\frac{4298\times10^{-8}}{K^{0.3}}\frac{g^2}{f^5}exp\left[-0.99.6K^{-1.23}\left(\frac{f_u}{g}\right)^{-4}\right]$	$K=\frac{g\,F}{u^{1.37}}$
Bretshneider	$S(f)=0.116\left(\frac{\overline{H}}{gT^2}\right)^2\frac{g^2}{f^5}exp\left[-0.178\left(\frac{1}{\overline{T}\,f}\right)^4\right]$	---------

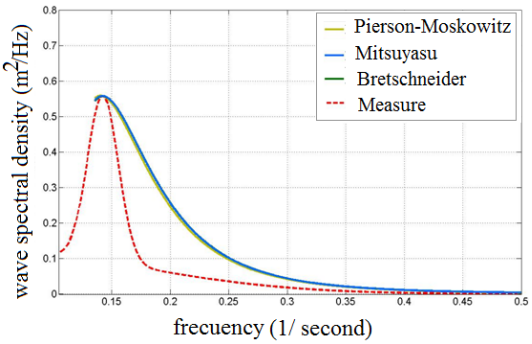

Figure 10: plotted Spectra Pierson-Moskowitz, Bretschneider and Mitsuyasu and after correction of relations

Lowest frequency that each of these spectra plotted are near the peak of the wave. For the spectrum at frequencies lower than the peak frequency, each of modified spectra, according to the figure 11, has fitted with Gaussian functions. In this figure minimum frequency is shown in shape of a point. Comparing the calculated errors values, wave height spectrum is calculated by the modified Pierson-Moskowitz More accurate than the other two spectra. Therefore the spectral parameters of the region using the mentioned spectra calculated H_{m0}=0.81 m and f_p= 0.14 (1/s).

Table 7: Comparison of significant wave height measurement error in each of the modified spectrum

spectrum	Pierson-Moskowitz	Mitsuyasu	Bretschnieder
Calculated H_S	0.81	0.8252	0.8265
Error of calculation (%)	8.56	10.21	10.39

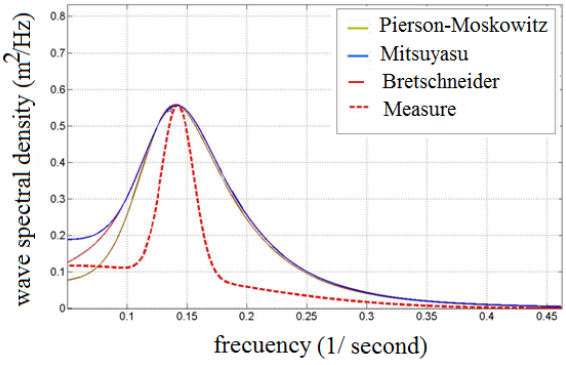

Figure 11: Gaussian fitted corrected spectra Pierson-Moskowitz ,Mitsuyasu and Bretschneider.

4.5. Directional spectrum of the wave

To plot directional spectrum using the relationship $E(f,\theta)=E(f)G(f,\theta)$ the function of the frequency $E(f)$ based on the frequency spectrum Pierson-Moskowitz, Mitsuyasu and Bretschneider and the angular part $G(f,\theta)$ based on the theory of PNJ is considered. Directional spectra of the region using modified and unmodified Pierson-Moskowitz, Bretschneider and Mitsuyasu Spectra have been plotted in Figures 12 to 15. Figure 12 shows the directional spectrum of the Pierson-Moskowitz spectrum similar to its frequency spectrum; less of the minimum frequency is not defined.

4.6. Comparison with previous research

Shamshirband et al, has predicted the height of the index wave in Asalouye region. In this research, soft models have been compared. The results demonstrate that all the models generally provide sound predictions. Due to the high level of variability in the bathymetry of the study area, implementation of the nested grid with different Whitecapping coefficient is a suitable approach to improve the efficiency of the numerical models.

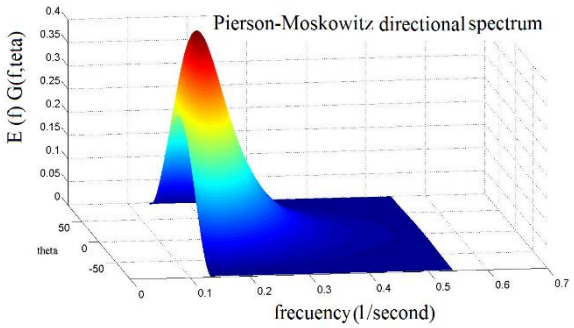

Figure 12: Pierson-Moskowitz directional spectrum, before the correction.

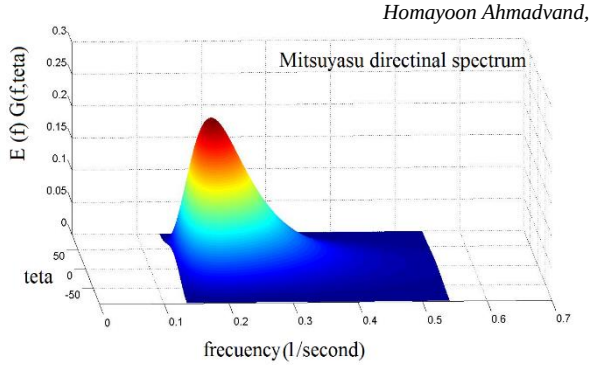

Figure 13: Mitsuyasu directional spectrum before the correction

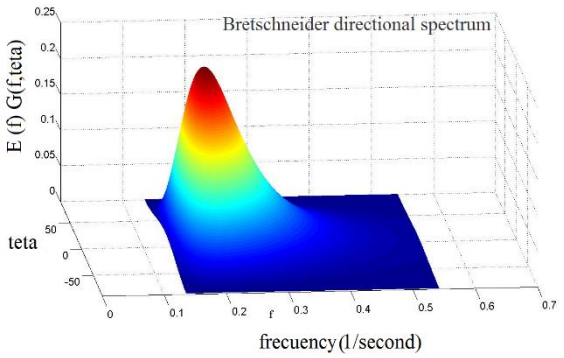

Figure 14: Bretschneider directional spectrum before the correction

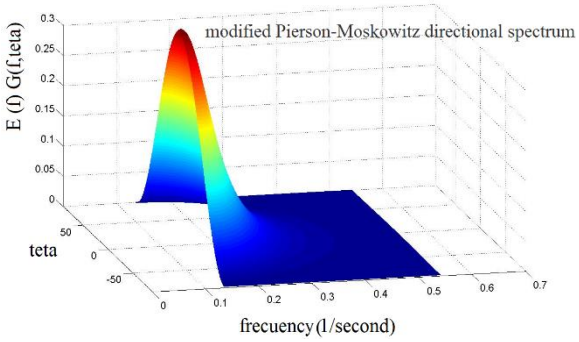

Figure 15: modified Pierson-Moskowitz directional spectrum

Performance on the ML models do not differ remarkably even though the ELM model slightly outperforms the other models. Figures (16) show the results of each of these models [29].

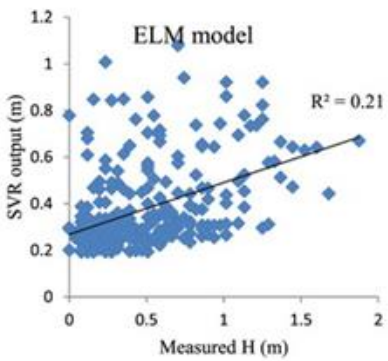

Figure 16 : The modeling results of Shamshirband et al. (2019) in predicting the height of waves in Asalouye region by soft computing

By comparing the results of Shamshirband research with the present research, it can be concluded that the best experimental model, which is the Jonswap model of this research, in predicting the wave height, is actually stormy and strong winds with higher accuracy than any of the soft models proposed in the shamshirband research.. This is despite the fact that in the researsh Shamshirband et al forecast is related to the online prediction and it is expected to have a lower accuracy.

Boyd and weaver was created parametric solver which incorporates four different wave height formulations (SMB, SPM, TMA, CEM) and can be used to create an ensemble average of parametric results. With validation from an ADCP deployed in the domain, the parametric models produced an average accuracy within 6% for wave height. This model also accurately simulates tropical storm wind events including variability in wind speed and direction with an average global accuracy of within 12.9% compared to SWAN [30]. Kotaška et al, concluded that the SMB model is the most accurate among the experimental models with an RMSE of 0.02 in online prediction in the deep water region [21]. So It is possible to predict with Jonswap's formula with an accuracy of 0.44 in Asalouye port, the data were collected in areas that were in deep water conditions. This difference in accuracy can be applied to the results of forecasts calculated in the lead time hours.

In the research of Najarpour et al., using adcp data, have shown the dominant spectrum of this region is in good agreement with the Janswap wave spectrum. In this research, it has been shown that with higher accuracy, the dominant spectrum of this region is closer to the Pierson-Moskowitz wave spectrum after the parameterization of the wave spectrum coefficients [31].

4.7. Conclusion

Assimilating observation data in to wave models can significantly improve the numerical simulation accuracy of ocean waves. This research focuses on the use of experimental and spectral methods in predicting wind waves in Asalouye port. The most important results of this research can be listed as follows:

- According to the past results in wave forecasting, it can be mentioned that experimental models have still maintained their validity in predicting wave height and in some cases where there is no access to marine measuring devices, these valid methods can be used with high predictive accuracy. It was used to evaluate the height and period of wind-induced waves in the region asalouye.
- In general, comparing performed show that Jonswap method for duration of 6 hours more accurately estimates the wave height and wave period. For durations of 6 and 9 hours the Jonswap empirical formula provided the most accurate estimation of

wave height (Hm0) with an average of RMSE = 0.44 m. Furthemore SPM and SMB methods for 12 hours duration, are considered most useful.

--The results show that the spectral proposed method has a high accuracy for identifying wave parameters shuch as wave period and significant wave height which is a re-emphasis on past results. in addition the spectral analysis of data showed that Pierson-Moskowitz, Mitsuyasu and Bretshneider spectrum with slight differences are close to the spectrum measured. So in the end it became clear that with the correction of their relationship Hs in the lowest range of errors is calculated by Bretshneider.

-It is noteworthy that the spectrums that are discussed in this study, all are suitable for deep water condition. With waves of deep water to the area with an average depth or less, time changes in the form of spectrum will take place. In this case use of TMA spectrum recommended that is modified Jonswap spectrum and by the depth and frequency-dependent coefficient of φ (f,h) is amended. This spectrum serves as a basis for simulating oscillatory waves and their impact on shore protection structure design.

- In the past research, it has been shown that in the northern sea areas of Iran (Caspian sea), the spectrum of wind waves has a double peak. This issue has been studied due to the return of waves from the coastal strip as well as the swell waves formed in the coastal zone. This is despite the fact that in the areas of the southern coasts of Iran, the spectrum of computational waves does not show such a thing and wave period sea had had lower 10 s. However, sometimes strong winds have been present in this area and the spectrum shown does not indicate the presence of swell waves, and all the waves recorded by marine devices are all the presence of local wind and local waves of the region.

Acknowledgement

The authors are thankful to the Ports & Maritime Organization, Iran for data used in this study.

References

[1] Barnes AT, Becker JM, Tagarino KA, O'Reilly WC, Siegelman M, Thompson PR, Merrifield MA. Rising sea levels and the increase of shoreline wave energy at American Samoa. Scientific Reports. 2024 Mar 2;14(1):5163.

[2] Verdejo H, Awerkin A, Kliemann W, Becker C, Chávez H, Barbosa KA, Delpiano J. A Dynamic Stochastic Hybrid Model to Represent Significant Wave Height and Wave Period for Marine Energy Representation. Energies. 2019 Mar 7;12(5):887.

[3] Raj N, Prakash R. Assessment and prediction of significant wave height using hybrid CNN-BiLSTM deep learning model for sustainable wave energy in Australia. Sustainable Horizons. 2024 Sep 1;11:100098.

[4] Hashemi S, Shahidi R, Gill EW. Extraction of the significant wave height from synthetic HF radar data acquired on a floating platform. IET Radar, Sonar & Navigation. 2023 Nov;17(11):1639-45.

[5] Ardhuin F, De Carlo M. Along-track resolution and uncertainty of altimeter-derived wave height and sea level: re-defining the significant wave height in extreme storms. Authorea Preprints. 2024 Apr 19.

[6] Sartini L, Antonini A. On the spectral wave climate of the French Atlantic Ocean. Ocean Engineering. 2024 Jul 15;304:117900.

[7] Xu J, Liu S, Li J, Jia W. Experimental study of wave height, crest, and trough distributions of directional irregular waves on a slope. Ocean Engineerigdng. 2021 Dec 15;242:110136.

[8] Rashidi Ebrahim Hesari A, Andi S, Farjami H. Study of internal waves in the Persian Gulf using field data and satellite images. International Journal Of Coastal, Offshore And Environmental Engineering (ijcoe). 2019 Nov 1;4(4):9-16.

[9] Goharnejad H, Nikaein E, Perrie W. Assessment of wave energy in the Persian Gulf: An evaluation of the impacts of climate change. Oceanologia. 2021 Jan 1;63(1):27-39.

[10] Vafaei Poursorkhabi R, Ejlali RG, Naseri A, Hosseinchi Gharehaghaji A. Experimental Study on Assessing Interaction of Quay Walls and Random Waves Using Artificial Neural Network. International Journal Of Coastal, Offshore And Environmental Engineering (ijcoe). 2023 Nov 1;8(4):1-8.

[11] Roulston MS, Ellepola J, von Hardenberg J, Smith LA. Forecasting wave height probabilities with numerical weather prediction models. Ocean Engineering. 2005 Oct 1;32(14-15):1841-63.

[12] Szewczyk TM, Morro B, Díaz-Gil C, Gillibrand PA, Hardwick JP, Davidson K, Aleynik D, Planellas SR. Interactive effects of multiple stressors with significant wave height exposure on farmed Atlantic salmon (Salmo salar) welfare along an inshore-offshore gradient. Aquaculture. 2024 Jan 30;579:740184.

[13] Kumar P, Yadav A, Sardana D, Prasad R. Extreme wave height response to climate modes and its association with tropical cyclones over the

Indo-Pacific Ocean. Ocean Engineering. 2024 Mar 15;296:116789.
[14] Zhang C, Li Y, Cai Y, Shi J, Zheng J, Cai F, Qi H. Parameterization of nearshore wave breaker index. Coastal Engineering. 2021 Sep 1;168:103914.
[15] Lee UJ, Cho HY, Lee BW, Ko DH. Joint probability distribution of significant wave height and peak wave period using gaussian copula method. Journal of Coastal Research. 2024 Jan 15;116(SI):96-100.
[16] "Shore protection manual" (1984), U.S.Army Coastal Engineer Waterways Station,Vicksburg, MS, 2 Volumes, 4^{th} Edition.
[17]- "Coastal Engineering Manual" (2003), Chapter II -2: "Meteorology and Water Climate",Engineer Manual 1110-2-1100, U.S. Army Corps of Engineers, Washington,DC.
[18] Pakhirehzan M, Rahbani M, Malakooti H. Numerical Study of Winter Shamal Wind Forcing on the Surface Current and Wave Field in Bushehr's Offshore Using MIKE21. International Journal Of Coastal, Offshore And Environmental Engineering (ijcoe). 2018 Jul 1;3(2):57-65.
[19] Wang C, Li S, Yu H, Wu K, Lang S, Xu Y. Comparison of wave spectrum assimilation and significant wave height assimilation based on Chinese-French oceanography satellite observations. Remote Sensing of Environment. 2024 May 1;305:114085.
[20] Ahmadvand, H., Paeen Afrakoti, I., Akbari Nasab, M. Comparison of wave prediction methods in Amirabad port. International Journal Of Coastal, Offshore And Environmental Engineering(ijcoe), 2024; (): -. doi: 10.22034/ijcoe.2024.341132.0
[21] Kotaška S, Duchan D, Pelikán P, Špano M. Spectral analysis of oscillatory wind wave parameters in fetch-limited deep-water conditions at a small reservoir and their prediction: Case Study of the Hulín Reservoir in the Czech Republic. Journal of Hydrology and Hydromechanics. 2024;72(1):95-112.
[22] U.S. Army Coastal Engineering Research Center 1977 Shore protection manual. Fort Belvoir, VA, 3 Volumes, 3th Edition.
[23] Mahmoud M, Salameh T, Al Makky A, Abdelkareem MA, Olabi AG. Case studies and analysis of wind energy systems. InRenewable Energy-Volume 1: Solar, Wind, and Hydropower 2023 Jan 1 (pp. 363-387). Academic Press.
[24] Massel, S.R. 1955 Ocean Surface Waves: Their Physics and Prediction, WORLD SCIENTIFIC, Pub.
[25] Rubert, T. 2006 Waves and Waves Forces on Coatal and Ocean Structures. Vol. 21.
[26] Zheng Z, Dong G, Dong H, Ma X, Tang M. Research on the methods for separating wind sea and swell from directional wave spectra in finite-depth waters. Ocean Dynamics. 2024 Feb;74(2):113-31.
[27] Marghany M. Synthetic aperture radar imaging mechanism for oil spills. Gulf Professional Publishing; 2019 Aug 21.
[28] Mazaheri et al have also shown that the wave coefficients can be modified and the use of modified wave coefficients can be used to express the wave behavior in the northern waters of the Persian Gulf with higher accuracy (Mazaheri and Arabzadeh 2015).
[29] Shamshirband S, Mosavi A, Rabczuk T, Nabipour N, Chau KW. Prediction of significant wave height; comparison between nested grid numerical model, and machine learning models of artificial neural networks, extreme learning and support vector machines. Engineering Applications of Computational Fluid Mechanics. 2020 Jan 1;14(1):805-17.
[30] Boyd SC, Weaver RJ. Replacing a third-generation wave model with a fetch based parametric solver in coastal estuaries. Estuarine, Coastal and Shelf Science. 2021 Apr 5;251:107192.
[31] Najarpoor M A, Chegini V, Sadrinasab M. Characteristics of wind wave spectrum in Asalouye region. Jurnal of Marine Sience and Techlogy, 2013 March. 11(4): 57-63.

Appendix

Tabel 1: Empirical equation to prediction wave

method	Minimum time necessary for fetch limited condition	Wave height and wave period
SMB	$\frac{gt_{min}}{U} = 6.5882\, exp\left\{A^{0.5} + 0.8798\left(ln\left(\frac{gX}{U^2}\right)\right)\right\}$ $A = 0.0161\left(ln\left(\frac{gX}{U^2}\right)\right)^2 - 0.3692\left(ln\left(\frac{gX}{U^2}\right)\right) + 2.2024$	$\frac{gH_s}{U^2} = 0.283\tanh\left[0.125\left(\frac{gX}{U^2}\right)^{0.42}\right]$ $\frac{gT_s}{2\pi U} = 1.20\tanh\left[0.077\left(\frac{gX}{U^2}\right)^{0.25}\right]$
Jonswap	$t_{min} = 65.5\frac{X^{0.67}}{g^{0.33}U_{10}^{0.33}}$	$H_{mo} = 0.0016\frac{U_{10}\, X^{0.5}}{g^{0.5}}$ $H_p = 0.286\frac{U_{10}^{0.33}\, X^{0.33}}{g^{0.67}}$
SPM	$\frac{gt_{min}}{U_A^2} = 6.88\times 10^{1}\left(\frac{gX}{U_A^2}\right)^{\frac{2}{3}}$	$\frac{gH_{mo}}{U_A^2} = 1.6\times 10^{-3}\left(\frac{gX}{U_A^2}\right)^{\frac{1}{2}}$ $\frac{gT_p}{U_A} = 2.857\times 10^{-1}\left(\frac{gX}{U_A^2}\right)^{\frac{1}{3}}$
CEM	$t_{x,u} = 77.23\frac{X^{0.67}}{U_{10}^{0.34}\, g^{0.33}}$	$\frac{gH_{mo}}{U_*^2} = 4.13\times 10^{-2}\left(\frac{gX}{U_*^2}\right)^{\frac{1}{2}}$ $\frac{gT_p}{u_*} = 0.751\left(\frac{gX}{u_*^2}\right)^{\frac{1}{3}}$

Table 2: Spectral equation to prediction wave

spectrum	Equation of spectrum	description
Jonswap	$S(f)=\alpha H_s^2\ f_p^4\ f^{-5}\ exp\left[-\frac{5}{4}\left(\frac{f_p}{f}\right)\right]^4$	$\alpha \approx \frac{0.0624}{0.23+0.0336\gamma-\left(\frac{0.185}{1.9+\gamma}\right)}$ $\sigma=\begin{cases}\sigma_a=0.07 & f<f_p\\ \sigma_b=0.09 & f>f_p\end{cases}$ $T_p=\frac{T_s}{\left(1-0.132\gamma^2-0.559\right)}$
Pierson-Moskowitz	$S(f)=\frac{5}{16}H_s^2\ f_p^4\ f^{-5}\ exp\left[-\frac{5}{4}\left(\frac{f_p}{f}\right)^4\right]$	$T_p=1.4\overline{T}$
Mitsuyasu	$S(f)=\frac{1.15\times10^{-4}}{\left(\frac{gF}{U_{10}^2}\right)^{0.312}}\frac{g^2}{f^5}exp\left[-0.99.6\left(\frac{gF}{U_{10}^2}\right)^{-1.23}\left(\frac{U_{10}f}{g}\right)^{-4}\right]$	$k=\frac{gF}{u^2}$
ISSC	$S(w)=5\frac{m_o}{w_p}\left(\frac{w_p}{w}\right)^2 exp\left[-\frac{5}{4}\left(\frac{w_o}{w}\right)^4\right]$	$m_o=0.0625H_s^2$ $w_p=0.7714\,\overline{w}$
Bretschneider	$S(T)=0.43\left(\frac{\overline{H}}{gT^2}\right)^2\frac{g^2}{f^5}exp\left[-0.675\left(\frac{1}{\overline{T}\ f}\right)^4\right]$	-------

INTERNATIONAL JOURNAL OF
COASTAL, OFFSHORE & ENVIRONMENTAL ENGINEERING IJCOE Vol.9/No. 4/Autumn 2024 (42- 55)

Available online at: www. Ijcoe.org

Assessing the Determinants of Effective Transboundary Water Resource Management Strategies in the Harirud River Basin, Iran

Ali Mokhtari Karchegani[1*] Ali Mohammadpour[2] Morteza Tavakoli[3]

[1] PhD student, Department of Geography and Rural Planning, Faculty of Humanities, Tarbiat Modares University, Tehran, Iran. Email: Ali_Mokhtari@Modares.ac.ir*

[2] Department of Civil Engineering, Urban Development and Disaster Management, Malek Ashtar University, Tehran, Iran. Email: mohamadpor1976@yahoo.com

[3]Associate Professor, Department of Geography and Rural Planning, Faculty of Humanities, Tarbiat Modares University, Tehran, Iran; Email: m-tavakoli@modares.ac.ir

ARTICLE INFO

Article History:
Received: 1 Sep. 2024
Accepted: 7 Oct. 2024

Keywords:
Transboundary
Water Management Strategies
multi-objective
optimization model
Harirud River Basin

ABSTRACT

Iran's geopolitical, economic, and social factors have significantly impacted international water resources alongside climatic influences in recent years. Consequently, identifying and implementing strategies to address a potential water crisis in the Harirud region has become crucial. This research primarily aims to uncover the factors influencing integrated water management in the Harirud basin. The findings will enhance decision-makers and policymakers' understanding of water resource utilization and management behaviors during drought periods. The sustainable development model serves as the theoretical framework for this study. The statistical sample comprises 12 interviewers and 128 subject-related experts, selected through a multi-stage technique with proportional allocation. Results from structural equation modeling indicate that geopolitical-hydrodynamic, technical-economic, institutional-legal, social-cultural, and infrastructural-physical variables exert the most significant influence on the adoption of water resource management policies. Practically, this research advocates for Integrated Basin Water Management (IBWM), with results offering vital policy implications to assist decision-makers in conserving international water resources.

1. Introduction

Water is an essential resource for the planet, with no viable substitutes. As humanity progresses into the third millennium, it confronts a significant shortage of water resources, propelling all nations toward a potential global crisis [1]. Population growth, rapid urbanization, agricultural and industrial development, and climate change have escalated water demand, rendering water resources increasingly vulnerable [2]. The sharing of water among countries with differing approaches to utilization can lead to conflicts over shared resources, including rivers, lakes, and groundwater [3]. Consequently, the management of Transboundary Rivers necessitates consideration of engineering, environmental, legal, social, economic, and political factors that are often complex and challenging to resolve . However, territorial cooperation based on shared water resources can yield benefits that would not be achievable without collaboration [4]. Therefore, establishing an effective planning model for the equitable distribution of water resources can maximize advantages for all involved parties[5].

In the past decade, substantial research has focused on allocating water resources in the Harirud basin [5-6]. For instance, Paulo (2013) [7] examined the issue from the water security perspective and the threats arising from restricted access to Harirud's water resources. Nagheeby and Warner [5] (2018) analyzed the Harirud basin from a geopolitical standpoint and argued that Afghanistan's unilateral appropriation of water resources—particularly regarding the Salma Dam—has increased vulnerability for downstream nations. Additionally, ghandahari [8](2016) and Khoshsima and Mahjoobi [9] (2022) demonstrated that Afghanistan's water policies adversely affect neighboring countries,

potentially leading to conflicts. This underscores the necessity for territorial cooperation among the three countries to develop a mutually beneficial strategy. Nonetheless, previous studies have primarily concentrated on political and security dimensions. The ecosystem of the Harirud River Basin faces planning challenges related to instability in social, economic, and environmental systems that have received insufficient attention in earlier research.

The environmental instability within the Harirud River Basin has detrimental effects on partner countries, including Iran. The Afghanistan Institute for Strategic Studies indicates that approximately 50 percent of the water in the Harirud River Basin has diminished over the past thirty years. This decline has been exacerbated by the construction of two Salma Dams by Afghanistan and the Dosti Dam by Iran and Turkmenistan [10]. These developments threaten the water supply in northeastern Iran and induce instability across multiple dimensions. Firstly, concerning social security, issues such as increased regional migration threats, diminished food security, and deteriorating health conditions arise [11]. Secondly, economic security is compromised through heightened production costs and agricultural, industrial, and service stagnation [12]. Thirdly, environmental security suffers from adverse land use changes, reduced surface water access, ecosystem destruction, diminished biodiversity, and drought conditions[13]. Fourthly, political-administrative security is affected by weakened local government authority and decreased citizen satisfaction with political decisions. Lastly, military security is jeopardized by rising internal insecurity and conflicts over water resources [14]. Moreover, it is crucial to recognize that the repercussions of drought in Harirud extend beyond these instabilities; they also serve as leverage in Afghanistan's political dealings with downstream nations [15]. Consequently, there is an urgent need to investigate various aspects of sustainability within human and natural systems in the Harirud watershed from a planning perspective concerning northeastern Iran.

Given the reduced water resources within the Harirud watershed, managing shared water resources with Afghanistan and Turkmenistan is imperative. Spatial analysis of the Harirud watershed can provide a more accurate understanding of its sustainability status [16]. Through strategic planning analysis, all challenges related to security in northeastern Iran can be addressed while striving for territorial balance [17]. Such a comprehensive approach to addressing water issues in this region aims to achieve territorial sustainability by balancing different systems [18]. As neighboring countries strongly desire to optimize shared water resource utilization, pursuing logical solutions grounded in scientific principles is essential [4]. Specifically, developing a scientific program focused on win-win outcomes can avert a common international tragedy [6]. Thus, the successful management of Harirud basin resources for Iran and its neighboring countries hinges on applying spatial planning methodologies.

The primary objective of this study centers on managing the Harirud basin through a spatial planning framework by identifying factors that threaten Iran's social, economic, environmental, political, and military security systems[19]. This research aims to fill existing knowledge gaps regarding sustainability in the Harirud basin while providing critical information for policymaking and strategic planning within this region.

2. Background

Global studies have explored the Harirud Watershed from various perspectives. Several contributions have analyzed the watershed through a geopolitical lens. For instance, Araújo et al [20] (2015) investigated the global trends in water security and the threats to regional stability posed by transboundary water resources. In examining Afghanistan's transboundary water issues, he identified the causes and factors contributing to international conflicts between Afghanistan and its neighboring countries, ultimately proposing a framework for effectively managing the region's water resources. While many scholars have focused on the hydropolitics of Central Asia, particularly regarding the Aral Sea basin [21], specific studies addressing the hydropolitics of the Harirud basin remain limited [15]. This scarcity of research has hindered a comprehensive understanding of the complex geopolitical dynamics within the basin. For example, Thomas and Warner [15](2015) explored the interplay between power and transboundary water interactions but did not adequately emphasize the political implications of this volatile region. The intricate nature of geopolitical interactions necessitates further detailed analysis; for instance, the authors suggest

that Iran may gain from project delays and increased costs [22], yet this perspective is only partially represented in the existing literature.

Some partnerships have concentrated on water management among riparian countries. Research on dispute resolution in transboundary river basins has utilized optimization and game theory models to focus on river water allocation. These studies aim to elucidate water allocation processes and the benefits—or lack thereof—of cooperation among all riparian nations. Mousavizadeh et al, [23] (2023) compared participatory and non-participatory approaches to large-scale river water allocation in southern Iran, highlighting the significance of cooperation concerning both water quantity and quality issues. Timmerman & Langaas. (2005) [24] identified 14 criteria influencing transboundary water management and prioritized these criteria in hypothetical basins using fuzzy clustering methods based on expert opinions. Their findings indicated that food security, equitable profitability, water flow quality and quantity, and hydrohegemony were paramount for advancing negotiations. Naghdi et al. (2020) [25] developed a multi-objective optimization model for water allocation in Iran's Sefidroud basin, aiming to maximize revenue while minimizing inequality in water distribution. Leo et al. (2020) [26] employed a fuzzy coalition game model for water allocation in the Lancang-Mekong River basin across East and Southeast Asia.

Recent studies addressing the Harirud watershed in Iran encompass diverse topics. Aamer (2023) [27] argued that fostering regional cooperation on water issues necessitates shifting away from traditional security approaches towards a human security framework, particularly given the challenges of water scarcity faced by Iran, Afghanistan, and Turkmenistan. This developmental framework could facilitate cooperative initiatives and joint projects in the Harirud basin based on strategic goals and mutual needs, including coordinated management of shared resources, continuous engagement with local users, and control over population growth and migration. Yar (2023) [11] examined the dual role of border rivers in shaping inter-country relations, focusing specifically on the Harirud border river through documentary analysis. They assessed how this shared resource fosters cooperation between Iran and Turkmenistan while introducing four convergence types: political, social, economic, and structural; they noted that climatic factors significantly influence regional tensions. They highlighted the Dosti Dam as an example of cooperative legal frameworks for joint resource exploitation between Iran and Turkmenistan.

Ahmadzai & McKinna (2018) [28] posited that economic variables are critical to fostering regional convergence while emphasizing that sustainable development must prioritize human-centered approaches to environmental threats as primary factors jeopardizing economic stability. Ghandahari et al. (2016) [8] analyzed interactions among Iran, Afghanistan, and Turkmenistan using game theory alongside a comprehensive water resource management model to evaluate various management scenarios within the Harirud watershed. Their findings demonstrated that leveraging knowledge of water resource management could transform potential conflicts into profitable opportunities for all involved nations.

Sakhi (2023) [29] investigated international water agreements—such as treaties, protocols, and bilateral or multilateral accords—that either mitigate or exacerbate disputes among interested countries. They referenced historical agreements like the 1980 Iran-Soviet Treaty concerning northeastern rivers and the 1982 Helmand River Treaty with Afghanistan, analyzing their provisions related to data exchange, organizational structures, and dispute resolution mechanisms. Their results indicated that while most agreements possess desirable data sharing and dispute resolution structures provisions, they often falter during implementation phases.

Kaviani-Rad et al. (2019) [30] acknowledged the longstanding water crisis and is poised to escalate further. They argued that political geography—manifested through hydropolitical orientations—analyzes power relations among political entities from subnational to global scales within contexts ranging from cooperation to competition. They noted that climate change at a global level, coupled with regional precipitation pattern shifts, has led previously arid countries to experience excessive groundwater extraction, aquifer depletion, and land subsidence.

Khoshsima and Mahjoubi (2019) [9] identified transboundary water management challenges from a diplomatic perspective within the Harirud basin. Their study aimed to pinpoint effective parameters influencing negotiations from a hydropolitical standpoint. The results underscored that achieving comprehensive agreements during

bilateral or multilateral negotiations necessitates a strong focus on political and economic axes framed within national security criteria alongside international relations considerations related to the water economy, political economy, joint economic initiatives, exports, and imports.

3. Methodology

This section provides a comprehensive overview of the study area, the rationale for its selection, the sampling design, data collection methods, the indicators chosen for analysis, and the techniques employed for data analysis.

1-3 Study Area Selection

The Harirud River Basin is a vital transboundary water system that traverses Afghanistan, Iran, and Turkmenistan, playing a crucial role in the socio-economic fabric of these countries. Originating in the Hindu Kush mountains, the Harirud River flows through diverse terrains before merging with the Amu Darya River. The basin is characterized by its complex geopolitical dynamics, exacerbated by historical tensions and contemporary interactions among the riparian states [14].

Water availability in the Harirud Basin is critical, with an estimated annual flow of approximately 2.5 billion cubic meters entering Iran from Afghanistan [5]. This water is essential for agricultural irrigation and drinking water supplies in northeastern Iran, where water scarcity poses significant challenges. The region is home to several dams, including the Salma Dam in Afghanistan, which has a capacity of 42 million cubic meters [8], and the Dosti Dam, constructed collaboratively by Iran and Turkmenistan. These dams are pivotal for managing water resources but also serve as points of contention among the riparian states.

Despite its importance, the Harirud River Basin faces significant challenges related to unilateral water management practices and geopolitical tensions. Upstream Afghanistan's dam construction projects have raised concerns among downstream nations regarding their water rights and security. The absence of a comprehensive trilateral agreement complicates these dynamics, increasing the potential for conflict over water allocation and usage. Given these complexities, understanding the hydropolitics of the Harirud River Basin is essential for fostering cooperation and promoting sustainable development among the riparian states.

Map No. 1: Geographical location of the study area.

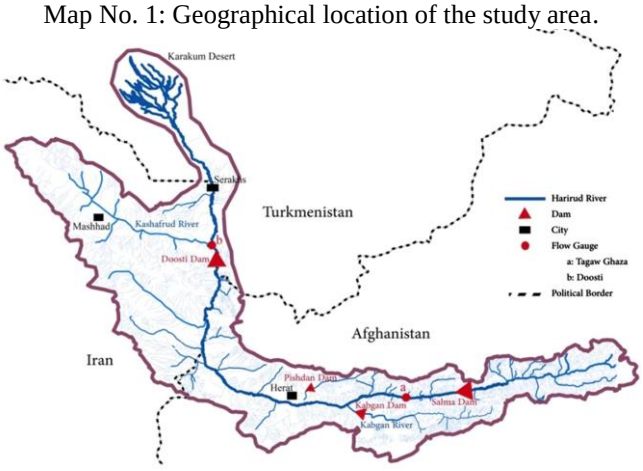

Source: Authors, 2024

2-3 Materials and Methods

This research employs a mixed-methods approach, integrating both qualitative and quantitative methodologies [31]. The initial phase involved qualitative methods to identify criteria and indicators for assessing water management in the Harirud Basin. This phase utilized a review of existing literature alongside interviews with experts and academics, chosen for their flexibility in data collection, particularly in contexts where information is scarce. This qualitative approach facilitated an in-depth exploration of the subject matter.

Data Collection

The study used focus group discussions (FGDs) and key informant interviews (KIIs) for qualitative data collection. These methods enabled the researchers to gather substantial primary data efficiently, reflecting a broad range of participant perspectives. The focus group consisted of 12 executive and academic experts, and the questionnaires were administered to 64 relevant experts who were selected based on their professional experience in water management.

The FGDs were conducted three times, utilizing telephone and in-person formats to discuss various water management strategies and policies pertinent to the Harirud Basin. The guiding questions for these discussions were developed from a thorough literature review, ensuring comprehensive coverage of the research topic. The key themes addressed included: 1) an overview of the status of water resources in the Harirud Basin, 2) the main components influencing water management within the basin, and 3) the extent to which each factor has impacted water management practices.

Quantitative data were collected through a structured questionnaire to assess participants' perceptions of current water management practices. Respondents rated the effectiveness of these practices on a 5-point Likert scale ranging from "very effective" (5) to "very low" (1). The responses were subsequently analyzed using principal component analysis to identify underlying patterns and relationships among the indicators.

3-3 Method of Analysis

This study utilized a mixed-methods research design comprising two consecutive stages of analysis. In the first stage, qualitative methods were employed to extract criteria and indicators for measuring water management in the Harirud Basin. This approach is widely recognized as effective in qualitative research, mainly when dealing with large datasets where participant responses exhibit minimal variation. Data saturation was achieved, indicating that additional data collection would yield diminishing returns in new insights [32]. During the reporting phase, direct quotes from participants were incorporated to enrich the narrative and provide a comprehensive portrayal of the in-depth information gathered.

The second stage involved quantitative analysis, specifically confirmatory factor analysis (CFA), conducted using SmartPLS version 4 software to evaluate the components and implications derived from the qualitative findings (Ringle et al., 2015). This method was chosen for several reasons: it assesses the quality of the measurement model and accommodates multiple criteria necessary for the study [33]. Furthermore, CFA allows for testing the consistency between theoretical constructs and empirical data, facilitating robust interpretation of results [34].

In model fitting, various indices were utilized to evaluate model fit. The Goodness-of-Fit Index (GFI), Comparative Fit Index (CFI), and Adjusted Goodness-of-Fit Index (AGFI) values closer to one indicate a better model fit, while a Root Mean Square Error of Approximation (RMSEA) value approaching zero suggests a superior fit [35]. A lower chi-square divided by degrees of freedom (X^2/df) ratio is preferable; ideally, this value should not exceed two. Although statistical significance in chi-square tests can indicate model suitability, it is often less reliable in larger samples exceeding 100 participants [36]. Overall, all model fit indices in this study demonstrated good fit and supported the proposed model.

4. Findings

4.1. Operationalization of criteria

The research findings are presented through confirmatory factor analysis (CFA) outputs, which elucidate the measurement model's implementation and results. In assessing the validity of the derived model, all indicators and components are evaluated using the Fornell-Larcker criterion for divergent validity. This method is essential for ensuring that constructs are distinct and not merely reflections of one another, thereby enhancing the robustness of the model [37].

In the context of this study, CFA was conducted using SmartPLS version 4 software to validate the measurement model derived from qualitative insights. This approach allows researchers to test hypotheses regarding the relationships among observed variables and latent constructs [38]. The selection of CFA is justified as it provides a comprehensive framework for examining the structural relationships within the data while ensuring that the measurement model meets established psychometric criteria.

A T-test was employed to assess further the significance of the factor loading paths within the model. This statistical test evaluates whether the observed relationships between variables significantly differ from zero, confirming their relevance in explaining the underlying constructs. By employing these rigorous analytical methods, this study aims to provide a nuanced understanding of water management indicators in the Harirud Basin, contributing to theoretical and practical implications in hydropolitics.

Table 1. The respondents need resilience improvement

Variables	Titles of indicators	Code	Sources
Geopolitical-geographical	Security of water resources	G1	Carter, 2010; Farooq, 1999; Favre & Kamal, 2004; Horsman, 2005; Mir,
	Conflict of strategic interests between countries	G2	

	The role of world powers in hydropolitical relations	G3	2010; Peterson, 2013; Shroder & Ahmadzai, 2016
	The influence of countries in procurement Laws related to water	G4	
	Power relations	G5	
	The weakness of Iran's hydropolitical policies	G6	
	The effect of Iran's regional water crisis on national security	G7	
	Geomorphology of Harirod watershed	G8	
	Climate change	G9	
	International dam-building policies	G10	
Technical and economic	Lack of a common interpretative framework	TE1	Favre & Kamal, 2004; Safi & Kohistani, 2013; Shelala, Kasting, & Cordesman, 2013; Yıldız, 2015; Karimipour, Kaviani Rad, 2015
	Weakness of water use technologies	TE2	
	Economic interdependence	TE3	
	Energy security	TE4	
	Iran's economic development program	TE5	
	Food security	TE6	
		TE7	
	Drinking water	TE8	
Institutional-Legal	Afghanistan's place in Iran's foreign policy goals	TE9	Nader, Scotten, Rahmani, Stewart, & Mahnad, 2014; Shelala et al., 2013; Shroder & Ahmadzai, 2016; Thomas & Warner, 2015; Torabi, 2012; (Popli Yazdi and Vathoqi, 2013; Tamna, 2015; Haq Panah and Rahimi, 1390; Sinai, 1390; Safavi, 1385; Kavyani Rad, 2015; Karimipour, 1380; Karimipour, 2013
	The role and perspective of political elites	IL1	
	Politics Local water sources in Afghanistan	IL 2	
	Agreement Letter the proper water Iran from Harirud water	IL 3	
	Performance of regional institutions and international on the issue of transboundary water resources	IL 4	
	Absence of mandatory rules Bringer international for transboundary waters	IL 5	
	A long-term dispute on the Hirmand water issue	IL 6	
Social-Culture	Iran's mistrust of Afghanistan	S1	
	Using water to influence Iran	S2	
	Afghan immigrants	S3	
	Community Participation in Water Management	S4	
	Public Awareness and Education on Water Issues	S5	
	Water Use Efficiency	S6	
	Stakeholder Engagement Level	S7	
Infrastructure - Physical	Infrastructure Development Status	IP1	Nagheeby, M., & Warner, J. 2018; Sinaee, S, 2012; Thomas, J., & Warner, J, 2015; Kamran, M., et al, 2017; O'Hara, S, 2000; Wegerich, K, 2008; Dukhovny, V., & Sokolov, V, 2003; Ghanbari, A., et al, 2023; Krampe, F., & Warner, J, 2017
	Land Use Changes	IP2	
	Irrigation Efficiency	IP3	
	Drought Frequency and Severity	IP4	
	Water Loss Assessment	IP5	
	Investment in Water Infrastructure	IP6	
	Water Pricing Mechanisms	IP7	
	Rainfall Patterns	IP8	

4.2. Measurement Model Analysis

Figure 1 illustrates the measurement model output, including path coefficients, R^2 values, and factor loadings. By established guidelines, the factor

The accuracy of the model employed to identify factors influencing water management in Harirud as preventive responses was evaluated in three stages: examining the model's Reliability and validity, assessing unidimensionality, and determining discriminant validity.

4.2.1. Reliability and validity

The results indicated that the composite Reliability of all constructs in the proposed model exceeded 0.50, and their Cronbach's alpha coefficients were more significant than 0.70. The average variance extracted (AVE) for all constructs was above 0.50. Therefore, all latent variables in the proposed model demonstrated appropriate validity and Reliability (see Table 3). In this context, Reliability is assessed by composite Reliability (CR), and AVE serves as a measure of the internal fit of the model, reflecting the consistency of items selected for measuring each factor. This assessment illustrates the correlation between the questionnaire items and the respective factors. When these values exceed

the recommended thresholds, it confirms that the questionnaire items are reliable and sufficiently valid for operationalizing the model. In essence, this indicates that the measurement accurately captures the target characteristic.

Loading values for observable variables should not fall below 0.4. As depicted in the figure, all factor loading values meet this criterion, indicating their acceptability across all paths analyzed. Furthermore, the R^2 values obtained exceed the threshold of 0.4, suggesting a substantial proportion of variance explained by the model.

The standardized factor loadings (λ) for all indicators selected for the model constructs exceeded 0.5 and were statistically significant at the 1% error level ($p < 0.01$). This finding supports the unidimensionality of the indicators chosen for the measurement models. Consequently, it can be asserted that the selected indicators were appropriately chosen for measuring the research constructs (see Table 2). This result indicates that respondents shared a consistent perception of the questions, as differing perceptions could diminish the measurement accuracy of the research instrument.

4.2.2. Unidimensionality

Table 2. The results of the fit of the measurement models.

Constructs	Measurement item	λ	t	Reliability and validity statistics
Geopolitical- hydropolitical (GH)	G1	0.871	70.952	AVE: 0.544 CR: 0.890 α: 0.902
	G2	0.684	23.706	
	G3	0.669	20.116	
	G4	0.725	20.68	
	G5	0.456	2.386	
	G6	0.807	19.269	
	G7	0.760	22.816	
	G8	0.788	19.533	
	G9	0.800	24.869	
	G10	0.929	299.344	
Technical and economic (TE)	TE1	0.699	30.874	AVE: 0.507 CR: 0.861 α: 0.864
	TE2	0.685	25.935	
	TE3	0.724	18.236	
	TE4	0.716	25.971	
	TE5	0.726	26.899	
	TE6	0.773	20.083	
	TE7	0.487	19.316	
	TE8	0.766	28.741	
	TE9	0.908	25.203	
Institutional-Legal (IL)	IL1	0.740	17.428	AVE: 0.520 CR: 0.818 α: 0.827
	IL 2	0.686	25.614	
	IL 3	0.662	25.847	
	IL 4	0.827	0.337	
	IL 5	0.792	18.612	
	IL 6	0.673	277.95	
Social- Culture (SC)	S1	0.919	213.513	AVE: 0.529 CR: 0.850 α: 0.852
	S2	0.718	0.457	
	S3	0.735	22.673	
	S4	0.784	27.438	
	S5	0.744	22.767	
	S6	0.758	20.574	
	S7	0.723	26.041	
Infrastructure – Physical (IP)	IP1	0.614	19.449	AVE: 0.552 CR: 0.878 α: 0.889
	IP2	0.303	59.057	
	IP3	0.717	21.399	
	IP4	0.736	21.97	
	IP5	0.706	2.489	
	IP6	0.714	21.152	
	IP7	0.677	17.038	

	IP8	0.708	23.74	

Table 3. Correlations with square roots of AVE

Constructs	1	2	3	4	5	6
GG	0.728 [a]					
IBWM	0.929**	0.776 [a]				
IP	0.928**	0.909**	0.743 [a]			
IL	0.766**	0.751**	0.748**	0.721 [a]		
SC	0.816**	0.869**	0.801**	0.666**	0.727 [a]	
TE	0.905**	0.890**	0.915**	0.744**	0.836**	0.737 [a]

[a] the square roots of AVE estimate.
** Correlation is significant at the <0.01 level.

4.2.3. Diagnostic validity

It was found that the square roots of AVE for the research constructs (0.728 < AVE < 0.737) were generally more significant than their correlation (0.766 < r < 0.801), reflecting the diagnostic validity of the constructs in the proposed model (Table 3)

Table 4. The summary of goodness-of-fit indices for the measurement model

Fit index	SRMR	d_ULS	d_G	Chi-square	NFI
Saturated model	0.135	17.357	n/a	infinite	n/a
Estimated model IBEM	0.135	17.357	n/a	infinite	n/a

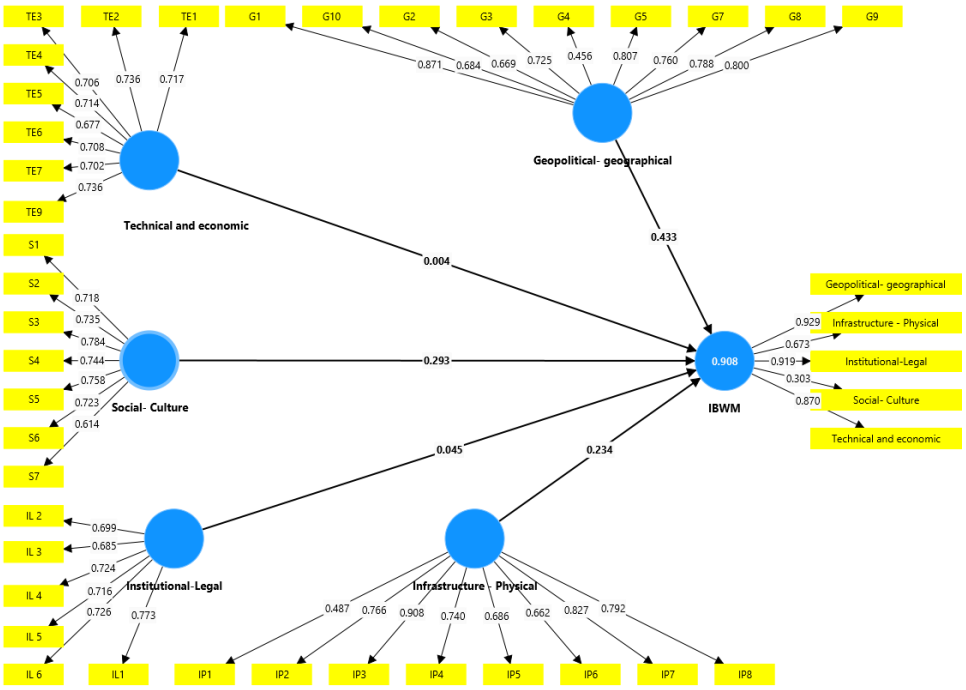

Figure 1. The path model with standardized factor loadings.

4.3. Measurement and structural model

The fit of the structural model, incorporating geopolitical-hydropolitical, technical-economic, institutional-legal, socio-cultural, and infrastructural-physical variables, was assessed using fit indices. The results indicate that the structural model demonstrates a good fit, and the research data adequately support the study's theoretical model (see Table 5).

As previously noted, the hypotheses were tested within the study's conceptual model using path analysis. The research path model, along with t-values and factor loadings, is illustrated in Figures 3 and 4. Table 6 provides a summary of the results from the research structural model, which are detailed in the following sections.

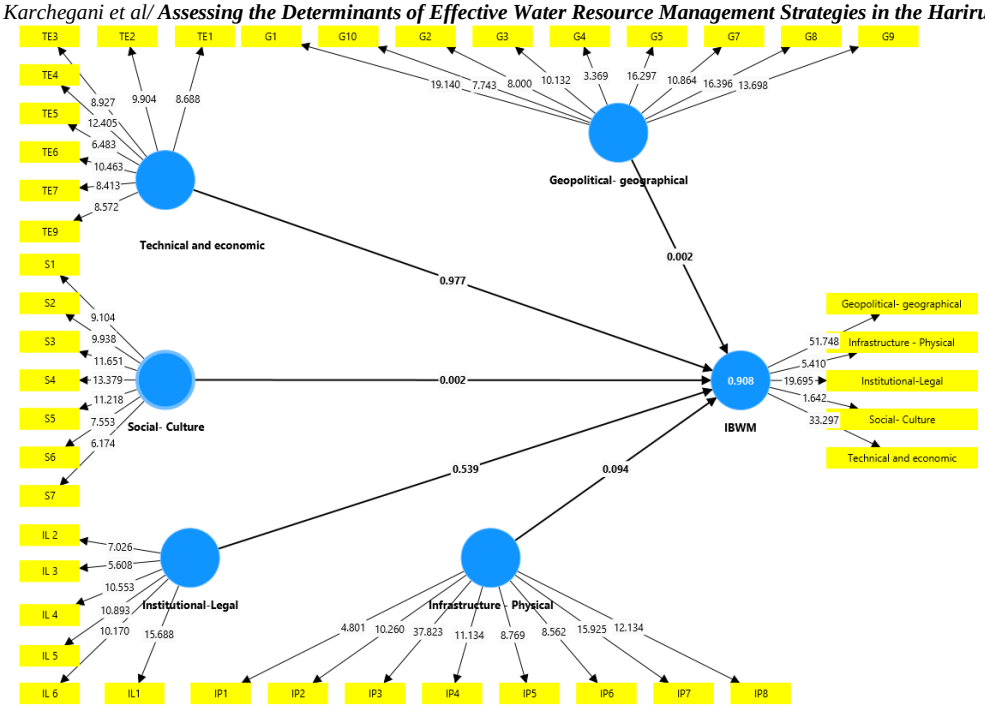

Figure 4. The path model with t-values.

Table 5. Path coefficients: Mean, STDEV, T values, p values

	Original sample (O)	Sample mean (M)	Standard deviation (STDEV)	T statistics (|O/STDEV|)	Result
Geopolitical- geographical -> IBWM	0.155	0.154	0.031	4.957	confirm
Infrastructure - Physical -> IBWM	0.278	0.272	0.069	4.003	confirm
Institutional-Legal -> IBWM	0.185	0.191	0.064	2.909	confirm
Social- Culture -> IBWM	0.172	0.173	0.010	17.749	confirm
Technical and economic -> IBWM	0.268	0.268	0.027	9.894	confirm

4.5. Testing hypotheses

This section presents the results for the final effect of variables on integrated water resources management of the Harirud basin (Table 5). The hypotheses were tested with the bootstrapping technique. All research hypotheses were supported based on the results except the effect of perceived barriers on management behaviors. It was also found that the research variables can account for 73.8% of water resources management.

This research employed Structural Equation Modeling (SEM) to identify the factors influencing water resources management in the Harirud basin. The analysis revealed that all five relationships among the Integrated Basin Water Management (IBWM) constructs were statistically significant. SEM indicated that five variables—geopolitical-hydropolitical, infrastructural-physical, institutional-legal, socio-cultural, and technical-economic—accounted for 87.9% of the variance in water resources management in the Harirud basin. In other words, these five variables effectively predicted 87.9% of the variance in the water resources management strategy for addressing water resource risks in the Harirud basin (Table 1). The research results regarding the hypotheses are presented below.

The findings demonstrated that perceived geopolitical-hydropolitical factors significantly impact water resources management, supporting Hypothesis 1. This result aligns with the report by Kaviani et al. (2019) [30], which underscores the importance of geopolitics-hydropolitics as a positive factor. Policymakers must adopt serious policies and diplomatic measures to address water resource scarcity, particularly when they perceive threats to water resources in the Khorasan region due to international competition and pressure. Hydropolitical issues compel policymakers to seek strategies for risk mitigation.

Perceived technical-economic benefits positively influenced policymakers' adoption of managerial behaviors to address the potential water supply crisis from the Harirud River. This finding

confirms Hypothesis 2, consistent with the results reported by Kaviani et al. (2019) [16] and Gandahari et al. (2016) [8]. Policymakers and managers recognize that their water management behaviors impact themselves and society. These incentives facilitate behavioral changes among citizens and farmers, motivating them to adopt coping and adaptation strategies [39]. Drought and dam construction projects significantly affect water supply security, thereby reducing the productivity and efficiency of agricultural and livestock products [40]. This reduction directly impacts food production and indirectly affects it [41], ultimately increasing production costs, lowering farmers' incomes, and exacerbating poverty in rural agricultural communities [42]. Therefore, if farmers believe that employing drought management practices can mitigate these adverse effects, they are likely to be more motivated to adopt such strategies [43], as drought management practices serve as a means to reduce vulnerability to drought [44].

The findings indicate that physical infrastructure categories significantly influence water resources in coping with water scarcity crises, supporting Hypothesis 3. This aligns with the studies conducted by Sani et al. (2022) [45] and Ghandahari et al. (2016) [8]. Perceived severity suggests that individuals recognize that threats, such as drought scarcity, entail various risks (economic and physical) detrimental to both urban and rural populations. Consequently, if policymakers perceive the lack of transportation infrastructure and drinking water supply as critical, they will likely implement risk reduction strategies. Previous research has demonstrated that threat severity significantly influences the adaptive responses of drinking water and energy supply programs [46].

The results indicate that socio-cultural variables significantly and positively influenced drought management behaviors, supporting Hypothesis 4. This finding is consistent with the studies conducted by Zeweld and Huylenbroeck (2018) [47] and Khoshsima and Mahjoubi (2019) [9]. However, these results are not entirely aligned with the reports by RostamAbadi and Jalali (2014) [48]. Social discussions typically reinforce behaviors, as emphasis on collective participation, public awareness, and productivity levels guide policymakers in utilizing reliable social and collective behaviors. Therefore, if policymakers implement training and outreach programs that leverage local capacities for water conservation, they will gain actionable insights and facilitate the adoption of new behaviors. Nonetheless, this factor has often been underestimated in efforts to motivate the adoption of new behaviors that may pose a threat to citizens [4].

The results regarding the perceived institutional-legal impact on the region's water supply confirm Hypothesis 5. This finding is consistent with Janusz-Pawletta (2015) [49] reports. Previous studies by Blanchon et al. (2012) [50] and King and Sturtewagen (2010) [51]attributed the significant influence of this variable on water resources management to variations in country approaches and the importance of participation. Research indicates that institutional and legal factors can shape policymakers' choices regarding adaptation strategies and decisions [30]. Both public and private organizations play a fundamental role in facilitating the transition from crisis to effective water resource management in various contexts. This process is crucial in guiding policymakers' decisions and behaviors. Highly effective organizations set ambitious goals, demonstrate strong commitment, actively seek solutions to challenges, and anticipate positive outcomes from their efforts. In contrast, less effective organizations tend to avoid challenging issues, exhibit weak commitment to their goals, and focus on failures rather than solutions when confronted with obstacles [52]. Consequently, research demonstrates that institutional-legal factors significantly influence water management and the achievement of macro-level objectives.

5. Discussion

The management of water resources in the Harirud basin is shaped by a complex interplay of geopolitical-hydropolitical, technical-economic, institutional-legal, socio-cultural, and infrastructural-physical factors. Understanding these influences is crucial for developing effective strategies to address water scarcity and promote sustainable management practices in this transboundary region shared by Afghanistan, Iran, and Turkmenistan. This discussion explores these factors' significant roles in shaping water management dynamics in the Harirud basin.

Geopolitical-hydropolitical factors significantly influence water management in the Harirud basin. The geopolitical landscape is characterized by historical rivalries and power dynamics among the riparian states, which complicate cooperation

on water resource management. As Nagheeby and Warner (2018) [5] argue, the control of water resources often serves not only economic interests but also geopolitical objectives that align with national security concerns. For instance, Afghanistan's upstream position allows it to control water flow to downstream nations, while Iran and Turkmenistan view this control as a threat to their water security. The lack of a trilateral agreement exacerbates these tensions, leading to unilateral actions that undermine collaborative management efforts. Consequently, achieving sustainable solutions requires recognizing the geopolitical context and fostering dialogue that emphasizes mutual interests among all stakeholders [5].

Technical-economic factors also play a critical role in shaping water management practices in the Harirud basin. The perceived economic benefits associated with infrastructure development, such as dams and irrigation systems, often drive investment decisions made by policymakers. However, these decisions can have significant ecological and social consequences if not appropriately managed. Research by Kaviani et al. (2019) [30] highlights that effective water management strategies must consider the technical capabilities of existing infrastructure and the economic implications of water scarcity. Policymakers must balance short-term economic gains from infrastructure projects with long-term sustainability goals to ensure water resources are managed effectively for future generations.

Institutional and legal frameworks are essential for facilitating cooperation and ensuring equitable access to water resources in the Harirud basin. The absence of robust institutions often leads to fragmented governance and ineffective management practices. According to Sani et al. (2010) [45], strong institutional arrangements can enhance collaboration among riparian states by establishing clear guidelines for water allocation and conflict resolution. Furthermore, legal instruments such as treaties and agreements can provide a framework for addressing disputes and promoting sustainable resource use. However, as Ahmadzai, Saadatullah (2018) [28] noted, existing legal frameworks often fail to account for the unique hydropolitical dynamics of the region, resulting in challenges for effective governance.

Social factors significantly influence public perceptions of water management practices in the Harirud basin. Community engagement and awareness are crucial for fostering stakeholder cooperation and promoting sustainable water use behaviors. Research indicates that social discussions can reinforce positive behaviors by emphasizing the importance of collective participation [11]. When communities perceive their participation in decision-making processes as valued, they are more likely to adopt adaptive behaviors contributing to effective water management. However, low public awareness about the implications of water scarcity can hinder efforts to implement sustainable practices.

Finally, infrastructural-physical factors are fundamental in determining the effectiveness of water management strategies in the Harirud basin. The condition of physical infrastructure—such as dams, canals, and irrigation systems—directly impacts the efficiency of water distribution and usage [53]. Inadequate infrastructure can exacerbate issues related to water scarcity by limiting access to reliable water sources for agricultural and domestic use. Therefore, investments in infrastructure development must be prioritized to enhance resilience against droughts and improve overall water security in the region.

In conclusion, effective water management in the Harirud basin requires a comprehensive understanding of the multifaceted influences exerted by geopolitical-hydropolitical, technical-economic, institutional-legal, socio-cultural, and infrastructural-physical factors. Policymakers must navigate these complexities while fostering cooperation among riparian states to address shared challenges related to water scarcity. By prioritizing dialogue and collaboration based on mutual interests, stakeholders can work towards sustainable solutions that promote equitable access to water resources while ensuring environmental integrity.

6. Conclusion

Water resources management in the Harirud River Basin, spanning Afghanistan, Iran, and Turkmenistan, is marked by intricate geopolitical dynamics that heavily influence regional cooperation and conflict. Historical rivalries complicate collaborative efforts, often leading to unilateral actions regarding water resource utilization. The absence of a binding tripartite agreement intensifies these tensions, underscoring the necessity for dialogue and frameworks that prioritize mutual benefits among the nations involved. Economic factors further complicate this landscape, as policymakers must navigate the

immediate economic gains from infrastructure projects like dams and irrigation systems against the long-term sustainability of water resources. Investments in such projects require careful consideration to prevent exacerbating existing inequalities or inflicting environmental harm. Effective governance in this context demands strategies that promote economic development while safeguarding ecological integrity. Institutional and legal frameworks are vital for fostering cooperation among the riparian states and ensuring equitable access to water resources. Strong governance structures can facilitate cooperation by establishing clear guidelines for water allocation and conflict resolution; however, weak governance often hinders these efforts, necessitating enhancements in institutional capacities and robust legal agreements to achieve effective transboundary water governance. Socio-cultural elements significantly influence public perceptions and behaviors regarding water management. Engaging communities in decision-making processes fosters a sense of ownership and encourages adaptive behaviors that contribute to sustainable resource usage. Public awareness initiatives are crucial for educating stakeholders about the implications of water scarcity and promoting collective participation in management efforts. Thus, effective water management in the Harirud Basin requires an integrated understanding of these interconnected factors. Policymakers should prioritize cooperation among Afghanistan, Iran, and Turkmenistan while fostering dialogue based on shared interests. By addressing geopolitical tensions, investing in sustainable infrastructure, strengthening institutional frameworks, and engaging communities, stakeholders can work towards equitable access to water resources. This comprehensive approach is essential for ensuring the long-term sustainability of this vital resource while promoting regional stability and cooperation among the riparian countries. Ultimately, a commitment to shared governance will pave the way for a more sustainable future in the Harirud Basin that benefits all involved while preserving precious water resources for future generations.

7. References

[1] Levin, A. T., Owusu-Boaitey, N., Pugh, S., et al. Assessing the burden of COVID-19 in developing countries: systematic review, meta-analysis and public policy implications. *BMJ Global Health, 7*(5), e008477. (2022)

[2] Guterres, A. Secretary-General's statement on the IPCC Working Group 1 Report on the Physical Science Basis of the Sixth Assessment. *United Nations: Secretary General, 9*. (2021)

[3] Gleick, P. H., & Shimabuku, M. Water-related conflicts: definitions, data, and trends from the water conflict chronology. *Environmental Research Letters, 18*(3), 034022. (2023)

[4] Tavakoli, M., & Mokhtari Karchegani, A. Analysis of factors affecting the structure of rural settlements in Makran coastal region in the face of climate change. *Journal of Oceanography, 13*(52), 131-144. (2023)

[5] Nagheeby, M., & Warner, J. The geopolitical overlay of the hydropolitics of the Harirud River Basin. *International Environmental Agreements: Politics, Law and Economics, 18*, 839-860. (2018)

[6] Mirzaei-Nodoushan, F., Bozorg-Haddad, O., Singh, V. P., & Loáiciga, H. A. Analysis of long-term strategies of riparian countries in transboundary river basins. *Scientific Reports, 11*(1), 20199. (2021)

[7] Paulo, P. L., Azevedo, C., Begosso, L., Galbiati, A. F., & Boncz, M. A. Natural systems treating greywater and blackwater on-site: Integrating treatment, reuse and landscaping. *Ecological Engineering, 50*, 95-100. (2013)

[8] Ghandhari, a., Alavi Moghaddam, S. M. R., & omranian khorasani, h. Water Resources Management in the Harirud river basin based on game theory. *Journal of Water and Sustainable Development, 3*(1), 115-121. (2016)

[9] Khoshsima, A., & Mahjoobi, E. Identification of Transboundary Water Resources Management Issues From Hydropolitical Perspective (Case Study: Harirud River). *Advanced Technologies in Water Efficiency, 1*(1), 48-69. (2022)

[10] Mohamadi, H., Ahmadi, E., Ahmadi, S., & Hakimi Khoram, A. Analysis of the effects of Afghanistan Salma Dam on water stresses in Mashhad. *Human Geography Research, 55*(4), 53-70. (2023)

[11] Yar, F. G. M., Rahmani, M., & Amir, E. Identifying the Effective Factors and the Importance of the Harirud Watershed in Afghanistan and its Impact on Iran. *Randwick International of Social Science Journal, 4*(2), 254-267. (2023)

[12] Michel, D. (2017). Iran's impending water crisis *Water, security and US foreign policy* (pp. 168-188): Routledge.

[13] Doost, Z. H., & Yaseen, Z. M. Allocation of reservoirs sites for runoff management towards sustainable water resources: Case study of Harirud River Basin, Afghanistan. *Journal of Hydrology, 634*, 131042. (2024)

[14] Loodin, N., & Warner, J. A review of hydro-hegemonic dynamics on the transboundary Harirud River Basin: 2001–present. *Water, 14*(21), 3442. (2022)

[15] Thomas, V., & Warner, J. Hydropolitics in the Harirud/Tejen river basin: Afghanistan as hydro-hegemon? *Water International, 40*(4), 593-613. (2015)

[16] Motaghi, A., Kavianirad, M., Zarghani, S. H., & Sadrania, H. Identifying and analyzing the factors affecting the hydropolitical relations of Iran and Afghanistan in the Harirud Basin. *Journal of Subcontinent Researches, 10*(34), 235-254. (2018)

[17] Amini, A., Jafari, H., Malekmohammadi, B., & Nasrabadi, T. Transboundary water resources conflict analysis using graph model for conflict resolution: a case study—Harirud River. *Discrete Dynamics in Nature and Society, 2021*(1), 1720517. (2021)

[18] Mokhtari Karchegani, A., Tavakoli, M., & Portahari, M. The New Paradigm of Neo_Endogenous Rural Development: A Thematic Analysis. *Journal of Rural Research, 15*(2), 208-225. (2024)

[19] Najafi, A., & Vatanfada, J. Transboundary water management improvements, the way forward in the middle east; case study: transboundary water management of iran and neighbors. (2013)

[20] Araújo, R. S., da Gloria Alves, M., de Melo, M. T. C., Chrispim, Z. M., Mendes, M. P., & Júnior, G. C. S. Water resource management: A comparative evaluation of Brazil, Rio de Janeiro, the European Union, and Portugal. *Science of the Total Environment, 511*, 815-828. (2015)

[21] aWegerich, K. Hydro-hegemony in the Amu Darya basin. *Water policy, 10*(S2), 71-88. (2008); bDukhovny, V. A., Sokolov, V. I., & Ziganshina, D. R. The role of donors in addressing water problems in central Asia. *Irrigation and Drainage, 65*, 79-85. (2016)

[22] Sinaee, V. Hydropolitics and human security: Water cooperation in relations between Iran, Afghanistan and Turkmenistan. *Iranian Review of Foreign Affairs, 2*(3), 111-133. (2012)

[23] Mousavizadeh, S. R., Moeini, R., & Shanehsazzadeh, A. Management of aquifer and dam reservoir quantitative-qualitative interaction. *Agricultural Water Management, 277*, 108116. (2023)

[24] Timmerman, J. G., & Langaas, S. Water information: what is it good for? The use of information in transboundary water management. *Regional Environmental Change, 5*, 177-187. (2005)

[25] Naghdi, S., Bozorg-Haddad, O., Khorsandi, M., & Chu, X. Multi-objective optimization for allocation of surface water and groundwater resources. *Science of the Total Environment, 776*, 146026. (2021)

[26] Liu, D., Ji, X., Tang, J., & Li, H. A fuzzy cooperative game theoretic approach for multinational water resource spatiotemporal allocation. *European Journal of Operational Research, 282*(3), 1025-1037. (2020)

[27] Aamer, F. Water security: diplomacy, global cooperation, and effective management of shared rivers. *Konrad-Adenauer Foundation & Stimson Center*. (2023)

[28] Ahmadzai, S., & McKinna, A. Afghanistan electrical energy and trans-boundary water systems analyses: Challenges and opportunities. *Energy Reports, 4*, 435-469. (2018)

[29] Sakhi, F. (2023). *Transboundary Water Interaction-The Role of Weaker Riparian States.* George Mason University.

[30] KAVIANI, R. M., Motaghi, D. A., Mokhtari, H. H., & Rashidi, N. A. The Impacts of Hydro-political Ties in Break-out of International Conflicts: a Case Study of Occupation of the Golan Heights. (2019)

[31] Torabi, Z.-A., Hall, C. M., Aallam, Z., & Mokktari Karchegani, A. Power and rent-seeking in the second homes tourism market: evidence from selected villages in Iran. *Journal of Policy Research in Tourism, Leisure and Events*, 1-22. (2023)

[32] Guest, G., Bunce, A., & Johnson, L. How many interviews are enough? An experiment with data saturation and variability. *Field methods, 18*(1), 59-82. (2006)

[33] Belton, V., & Stewart, T. (2012). *Multiple criteria decision analysis: an integrated approach*: Springer Science & Business Media.

[34] Ghanbar, H., & Rezvani, R. Structural equation modeling in L2 research: A systematic review. *International Journal of Language Testing, 13*(Special Issue), 79-108. (2023)

[35] Hu, L. t., & Bentler, P. M. Cutoff criteria for fit indexes in covariance structure analysis: Conventional criteria versus new alternatives. *Structural equation modeling: a multidisciplinary journal, 6*(1), 1-55. (1999)

[36] Kline, R. B. (2023). *Principles and practice of structural equation modeling*: Guilford publications.

[37] Fornell, C., & Larcker, D. F. Evaluating structural equation models with unobservable variables and measurement error. *Journal of marketing research, 18*(1), 39-50. (1981)

[38] Ringle, C. M., Sarstedt, M., Mitchell, R., & Gudergan, S. P. Partial least squares structural equation modeling in HRM research. *The international journal of human resource management, 31*(12), 1617-1643. (2020)

[39] Mills, J., Gaskell, P., Ingram, J., Dwyer, J., Reed, M., & Short, C. Engaging farmers in environmental management through a better understanding of behaviour. *Agriculture and human values, 34*, 283-299. (2017)

[40] Gebreyes, M., Bazzana, D., Simonetto, A., et al. Local perceptions of water-energy-food security: livelihood consequences of dam construction in Ethiopia. *Sustainability, 12*(6), 2161. (2020)

[41] Shabanzadeh-Khoshrody, M., Azadi, H., Khajooeipour, A., & Nabavi-Pelesaraei, A. Analytical investigation of the effects of dam construction on the productivity and efficiency of farmers. *Journal of cleaner production, 135*, 549-557. (2016)

[42] Zobeidi, T., Yazdanpanah, M., Forouzani, M., & Khosravipour, B. Climate change discourse among

Iranian farmers. *Climatic Change*, *138*(3), 521-535. (2016)

[43] Boazar, M., Abdeshahi, A., & Yazdanpanah, M. Changing rice cropping patterns among farmers as a preventive policy to protect water resources. *Journal of Environmental Planning and Management*, *63*(14), 2484-2500. (2020)

[44] Otitoju, M. A., & Enete, A. A. Climate change adaptation: Uncovering constraints to the use of adaptation strategies among food crop farmers in South-west, Nigeria using principal component analysis (PCA). *Cogent Food & Agriculture*, *2*(1), 1178692. (2016)

[45] Sani, Y., & Scholz, M. Interplay of Water–Energy Security and Food Consumption Patterns towards Achieving Nutrition Security in Katsina State, North-Western Nigeria. *Sustainability*, *14*(8), 4478. (2022)

[46] Falk, J., Globisch, B., Angelmahr, M., Schade, W., & Schenk-Mathes, H. Drinking water supply in rural africa based on a mini-grid energy system—A socio-economic case study for rural development. *Sustainability*, *14*(15), 9458. (2022)

[47] Zeweld, W., Van Huylenbroeck, G., Tesfay, G., Azadi, H., & Speelman, S. Impacts of socio-psychological factors on actual adoption of sustainable land management practices in dryland and water stressed areas. *Sustainability*, *10*(9), 2963. (2018)

[48] Rostamabadi, A., & Jalali, S. (2014). Water resources management in new legal order: Amirkabir University Publications, 779p (in Persian).

[49] Janusz-Pawletta, B. Current legal challenges to institutional governance of transboundary water resources in Central Asia and joint management arrangements. *Environmental earth sciences*, *73*(2), 887-896. (2015)

[50] Blanchon, D., & Graefe, O. Radical political ecology and water in Khartoum. A theoretical approach that goes beyond the case study. *Espace géographique (English Edition)*, *41*(1), 36-50. (2012)

[51] King, M., & Sturtewagen, B. Making the most of Afghanistan's river basins. *Opportunities for regional cooperation*. (2010)

[52] Mokhtari Karchegani, A., Khodadadi, A., & Tavakoli, M. The pattern of livelihood adaptation of rural communities in Iran in the face of climate change. *Journal of Geography and Environmental Hazards*, *13*(2), 265-293. (2024)

[53] Tuyisabe, J. B., Silungwe, F. R., & Mahoo, H. F. Assessment of Physical Status of The Irrigation Structures in Nyarubogo Irrigation Scheme, Rwanda. *African Journal of Empirical Research*, *5*(4), 1561-1575. (2024)

INTERNATIONAL JOURNAL OF
COASTAL, OFFSHORE & ENVIRONMENTAL ENGINEERING IJCOE Vol.9/No.4/Autumn2024(56-63)

Available online at: www. Ijcoe.org

Mean dynamic topography and currents in Persian Gulf and Indian Ocean using altimetry and GOCE data

Ali Hakimi[1], Masoud Torabi Azad*[2]

[1] *Hydrography Master of Science, Faculty of Marine Science and Technology, North Tehran Branch, Islamic Azad University, Tehran, Iran. Hakimi.ali68@gmail.com*
[*2] *Prof., Faculty of Marine Science and Technology, North Tehran Branch, Islamic Azad University, Tehran, Iran. (Corresponding author) M_Azad@Iau-tnb.ac.ir, Institution's Web address: (http://www.iau-tnb.ac.ir/) (https://orcid.org/0000-0003-0130-4279)*

ARTICLE INFO

Article History:
Received: 12 Sep 2024
Accepted: 15 Oct 2024

Keywords:
Mean Dynamic Topography
Geostrophic Currents
Mean Sea Surface
Geoid Height Gaussian Filter
Ekman Currents

ABSTRACT

Getting to know the oceans Mean Dynamic Topography (MDT) derived from the satellite altimetry data helps to study climates and steady state currents in the oceans. A MDT model named as MDT_IAU_TN_2014, including steady state surface currents was developed by the Islamic Azad University of IRAN, Tehran-North branch, hydrography group. The model includes magnitudes and directions of currents in the region of Persian Gulf and Indian Ocean given in a grid with 2'x2' arc minutes spacing in the latitude and longitude directions. To build up the model, a Mean Sea Surface (MSS) model should be subtracted from a Geoid heights model. An MSS called MSS_IAU_TN_2014, is derive using observations of 21 years of 6 altimetry satellites: Topex-Poseidon (T/P); ERS (E1) and (E2); Jason (J1) and (J2); Geosat Follow-On (GFO). MSS_IAU_TN_2014 differences relative to the MSS_CNES_CLS_2011 has 0.1 m RMS. Also a series of global geopotential coefficients estimated from four years of GOCE data is used to compute the geoid. A truncated Gaussian Filter with truncation radius of 1.386 arc degrees was used to match the spectral content of both MSS and Geoid. Sea Level Anomaly (SLA) an In-Situ data could be used to make the MDT_IAU_TN_2014 independent from any other models. At last, MDT_IAU_TN_2014 was compared with MDT_CNES_CLS09 0.51m RMS and MDT_DTU_2010 with 0.033m RMS. Velocity vectors from MDT_IAU_TN_2014 shows near coast currents perfectly, but there is some weakness in Oman Sea gyres details.

1. Introduction

The Mean Dynamic Topography (MDT) is a quantity comes from subtracting the Geoid Height (GH) from the Mean Sea Surface (MSS) at every point on sea. Then, the MDT's slope (relative to the geoid) would determine the direction of geostrophic currents. Two MDT models data were available by the time of this research: Mean Dynamic Topography Denmark Technical University 2010 (MDT_DTU_2010) given on geographical grid of 2 arc minutes spacing [1]. This model is based on the mean sea surface topography model MSS_DTU_2010 and the 2 month of GOCE geopotential data for the geoid as the reference surface. One of the advantages of this model is global coverage in a network of 2-minute points, and one of its disadvantages is the lack of north-south and east-west vectors of currents. In this model, after the difference between the two average levels of the seas and the geoid from each other, a type of Gaussian filter is used, this covers up to 111 km in terms of longitude and latitude. The second model is the Mean Dynamic Topography Centre National d'Etudes Spatiales collected localization satellites 2009 MDT_CNES_CLS09) with 15 minutes' resolution [2]. This model contains the east-west and north-south

geostrophic current components with itself as well. It is based on MSS_CLS01 [3] and 4.5 years of GRACE Geopotential data used for the reference geoid. Model MDT_CNES_CLS_2009 does not provide accurate information on medium dynamic topography due to its low resolution (15 minutes) near the shore. In contrast, the high-resolution (2 minutes) MDT_DTU_2010 shows the average dynamic topography in the study area well. MDT_CNES_CLS_2009 estimated changes in average dynamic topography from 0.43 m to 0.8 m, while MDT_DTU_2010 estimated this range from 0.21 m to 0.88 m.

In this research, a series of GOCE geopotential coefficients resulted from the collection of 4 years of GOCE observations was used to estimate the reference geoid in Persian Gulf, Oman Sea and Indian Ocean, i.e., in the area of interest. A mean sea surface topography model is also derived from observations of six altimetry satellites; T/P, E1, E2, J1, J2, GFO in study area of a geographical grid with spacing of 2'x2' arc minute. It is called the MSS_IAU_TN_2014. Both the MSS_IAU_TN_2014 and the geoidal height quantities are referred to the same datum (the Topex mission ellipsoid) and are in Mean tide system [4]. Since the reference ellipsoid is not a level surface, the derived MSS surface (referred to the ellipsoid) cannot be used for steady state current (water flow) investigation on sea. To make it useful or to change it to a dynamic (topography) surface, the reference surface has to be exchanged from the ellipsoid to the above mentioned geoid a level surface. Then, the MSS surface is so exchanged to a dynamic surface called here as MDT_IAU_TN_2014.

A filtering needed in order to eliminate the short scale (higher degree) geoidal errors. The Truncated Gaussian filter with half-width at half-maximum 1.386 degree in space domain was used in this research [2]. For the regional dynamic topography applications, the space domain methods are likely to be more efficient and accurate than spectral methods [1,5]. More information about Truncated Gaussian filter and its kernel is found at GUT User Guide and Algorithm Descriptions [6]. The aim of this study is to find the average dynamic topography using 21 years of altimeter data as well as 4 years of gravity data of GOCE satellite in the Persian Gulf region, Oman Sea and part of the Indian Ocean. Another goal is to obtain geostrophic current vectors in the study area.

2.Materials and Methods

There is a wealth of altimetry data collected from the year 1992 to 2013 (21 years) by T/P, J1, J2, GFO satellites Geophysical Data Record (GDR) and E1 (Geodetic Mission Phase E and F), E2 satellites Ocean Product Record (OPR) available for any user. It is used to derive the MSS_IAU_TN_2014 model. There are researches conducted in 1998 to apply corrections to the ERS data by CERSAT [7], which improves ERS orbit computation since then (RA/ATSR products - User Manual) [8]. But, there was no correct information about the location of ERS-ERS and ERS-T/P (especially E1) crossover points at the time in order to further improvement of orbits. The first step for the Mean Sea Surface (MSS) computation is to calculate the mean of Sea Surface Heights (SSH) along the repeated (in time) sub-tracks of altimetry satellites over the years available in the area of interest. The SSH quantity is computed from altimetry data (Range) as shown in equation 1.

SSH = Altimeter altitude from ellipsoid – measured Range + Corrections (1)

The mean value of SSHs over time in a same track is then called Mean Height (MH). The Basic Radar Altimetry Toolbox (BRAT) version 3.1.0 was used for the MH computation. The correction term in equation 1 includes the tidal periodic variations, physical earth corrections such as troposphere, ionosphere, and sea state biases. All of these corrections are considered from the satellite handbooks T/P (AVISO/Altimetry) [9], J1 (AVISO and PODAAC user Handbook) [10], J2 (OSTM/Jason-2 Products Handbook) [11], ERS (RA/ATSR products - User Manual) [8], GFO (GEOSAT Follow-On GDR User's Handbook) [12]. Among altimetry satellites, T/P (J1 and J2) has the highest orbit and longest data sets so it has been selected as a reference for corrections. After calculating all MHs in the area of interest, ERS MHs have been transformed from WGS84 ellipsoid to the Topex ellipsoid using the datum transformation formula given by Vanicek & Krakiwsky [13].

In order to take a full advantage of all satellite data in the region of interest and for the sake of homogeneity, the compatibility of different data sets (E1, E2, T/P, J1 and J2) are first tested. For this, some points called here as of test points in the number of about 5000 have been distinguished in the region to be in positions onto which the MH quantities can be

precisely derived from all different data sets. Then the differences of the MHs quantities coming from different data sets are computed in the test points relative to the T/P MHs after the unification of datum's. The differences are classified and tested for their fit to the normal Gaussian curve. Most outliers (200 out of 5831), based on the 95% confidence level, are found among the differences of E1 relative to the T/P MHs, concerning that the spacing of the E1 sub-tracks along the equator is about 8 km while for T/P it is about 315 km. The least amount of outliers (50 out of 16174) are found among differences of J1 MHs relative to the T/P MHs, concerning that their orbits are common with the T/P's. In computing the MH in other points (other than 5000) in the region, an average MH is selected out of different MHs obtained from data sets but accounting for the threshold of outliers experienced in the test points. Fig. 1 shows the map of MSSs derived from MHs values on the sub-track points by a linear interpolation on the 2'x2' arc degree grid already positioned in the region of interest. The solution is named as MSS_IAU_TN_2014. The rout mean squares (RMS) differences between the solution and the already available model of MSS_CNES_CLS_2011 are estimated to be 0.1 m in maximum.

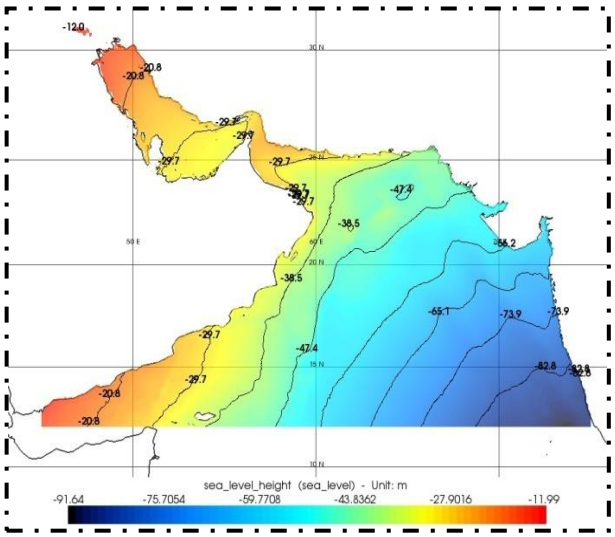

Fig. 1. The MSS_IAU_TN_2014 solution of mean sea surface referred to the reference ellipsoid of T/P satellite.

Precise geoidal heights are now derived from the Gravity field and Ocean Circulation Explorer (GOCE) geopotential model. GOCE has been orbiting the earth since 2009 and gathering higher resolution gravity data compared to the GRACE and facilitating ocean circulation study as the mission has been set for (ESA SP-1233) [14]. The GOCE DIR 4rth generation data could compute the geoidal height in the form of a series of spherical harmonics up to the harmonic degree and order of 260. This computation leaves a higher degree error called omission error as a result of disregarding higher degree (higher than 260) in the gravity field. In addition, there will be another source of errors called the commission errors as the result of least squares estimation method used for the estimation of the geopotential coefficients.

Geoidal heights in the region are calculated from the GOCE level 2 geopotential data (EGM_GOC_2) using DIR method [15]. This solution is called GOCE_DIR4th. By the time of research, the latest version of the data was the 4rth generation from November 2009 until October 2012 with a global coverage. The maximum number of spherical harmonic coefficients used is 260. The GOCE User Toolbox (GUT) version 2.1 was used to get the GOCE_DIR4th solution. The formula used for the geoid computation is completely described in ESA-GUT-AD-001 as it is referenced, (GUT User Guide and Algorithm Descriptions) [6].

3.Results and Discussion

The GOCE geoidal height model is subtracted from the MSS_IAU_TN_2014; the result is given in Fig. 2-a [16,17]. A Truncated Gaussian Filter with the averaging radius of 1.386 arc degree is then applied to filter out the higher order (>260) features surviving the subtraction, (Fig. 2-b). The MSS model so determined is lacking higher order (>260) information. To bring in the information, the MDT_DTU_2010, Fig. 2 c), is used. For this, the truncated Gaussian filter is applied, once more, to the MDT_DTU_2010 model, and the result is subtracted from the model itself to separate the higher order information needed, Fig. 2 d). Table 1 shows statistical differences between the MDT_IAU_TN_2014 relative to the MDT_DTU_2010 and MDT_CNES_CLS09 models.

Table 1. statistics of the three MDT models

	MDT_IAU_TN_2014	MDT_DTU_2010	MDT_CNES_CLS09
Resolution	2'*2'	2'*2'	15'*15'
Min(m)	0.305	0.212	0.436
Max(m)	0.910	0.890	0.800
RMS(m)	Compare to DTU_2010 0.033 Compare to CNES_CLS09 0.051	Compare to CNES_CLS09 0.054	

To derive the geostrophic currents on the sea surface, the gradients of the mean dynamic topography in the east and north directions ($\frac{\partial\zeta}{\partial y}, \frac{\partial\zeta}{\partial x}$) are used in the equations (2a, 2b), [18]:

$$u = -\frac{g}{f}\frac{\partial\zeta}{\partial y}, \quad \text{2-a}$$

$$v = \frac{g}{f}\frac{\partial\zeta}{\partial x}, \quad \text{2-b}$$

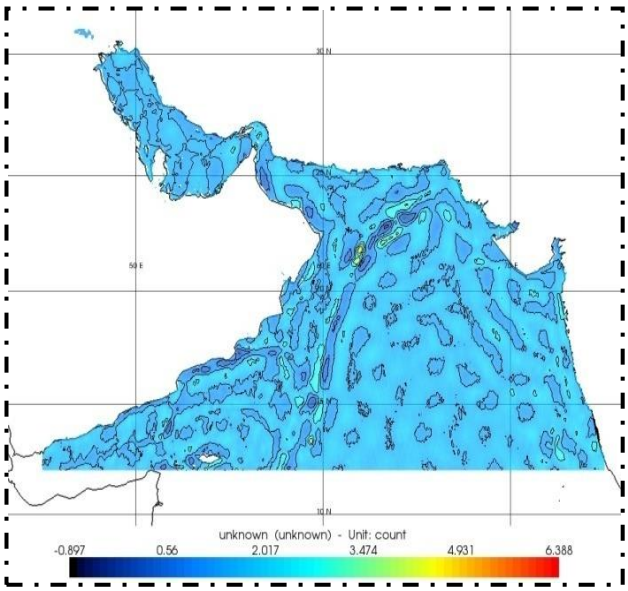

a)

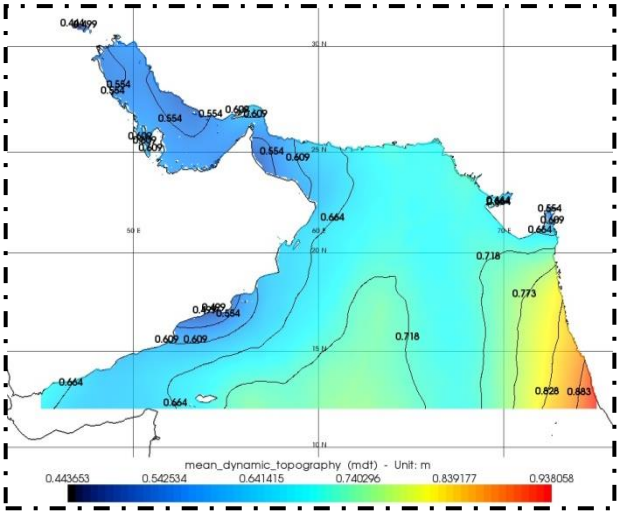

b)

c)

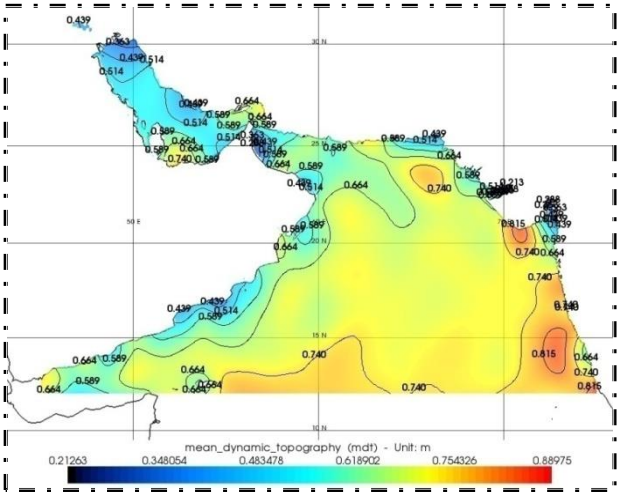

d)

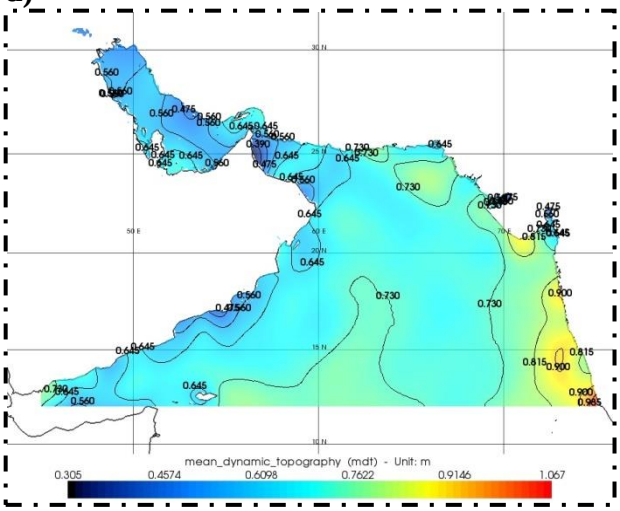

Fig. 2. a) MSS_IAU_TN_2014 subtraction from GOCE geoid, a) Repaired GOCE MDT using Truncated Gaussian Filter with 1.386-degree radius. b) MDT_IAU_TN_2014. c) MDT_DTU_2010.

The equations are the results of compensations between surface pressure gradients and the Coriolis acceleration on sea surface, where *u* and *v* are the east-west, Fig. 3 a), and north-south, Fig. 3 b), components of the current. ζ is the MDT_IAU_TN_2014 mean dynamic topography, g is the gravity, *f* is the Coriolis parameter which is equal to $2\Omega\sin\varphi$ and $|\Omega|= 7.292 \times 10^{-5}$ *radians/s* angular velocity of the earth rotation. The speeds of resultant geostrophic currents $V=\sqrt{u^2+v^2}$ are shown in Fig. 3 c) and the velocity vectors are shown in Fig. 3 d).

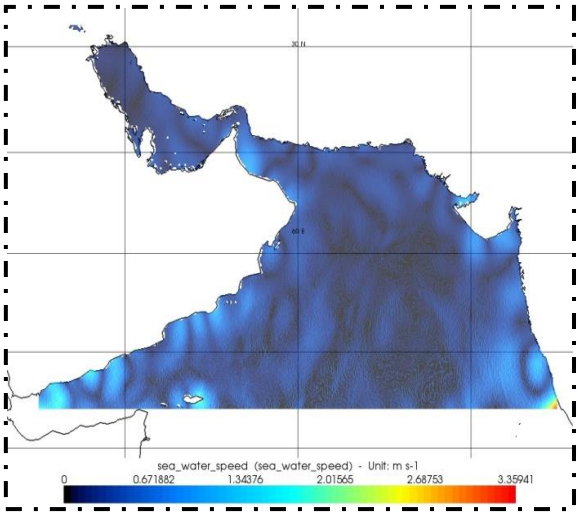

c)

a)

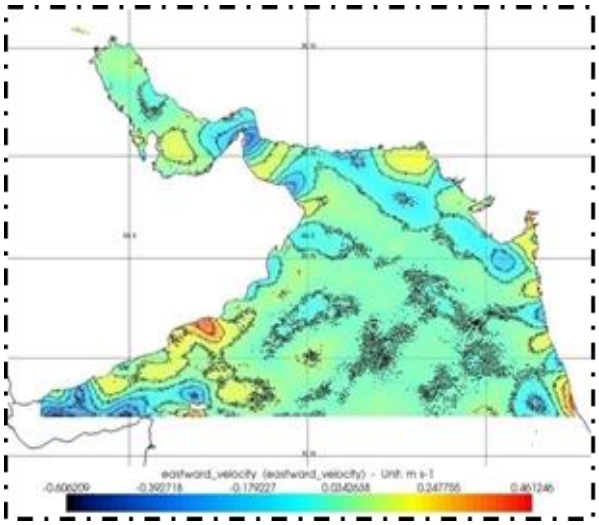

b)

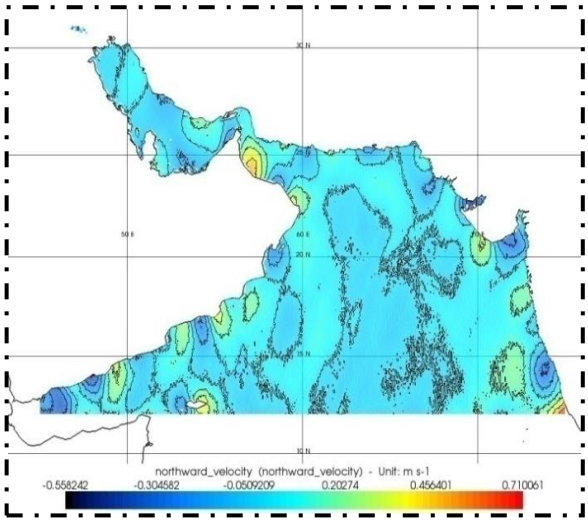

d)

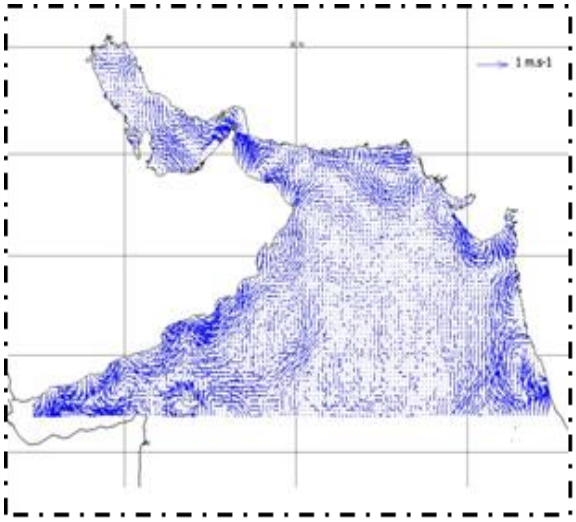

Fig. 3. a) MDT_IAU_TN_2014 east-west components, b) MDT_IAU_TN_2014 north-south components, c) Geostrophic values, d) Geostrophic currents.

At last, the mean Ekman currents calculated from 22 years of surface wind stress components, Fig. 4 a), in the Eq. 3 are added to the MDT_IAU_TN_2014 Geostrophic currents components to derive the total steady state currents, Fig. 4 b).

$$[u(z)^2+v(z)^2]^{\frac{1}{2}}=V_0e^{az} \qquad (3)$$

u and *v* here are the Ekman current components in the east-west and north-south directions,

$a = \sqrt{\frac{f}{2A_z}}, V_0 = \frac{T}{\sqrt{\rho_w^2 f A_z}}$, which $T = T_{yz}$ when wind blows to north direction (T is wind stress).

a)

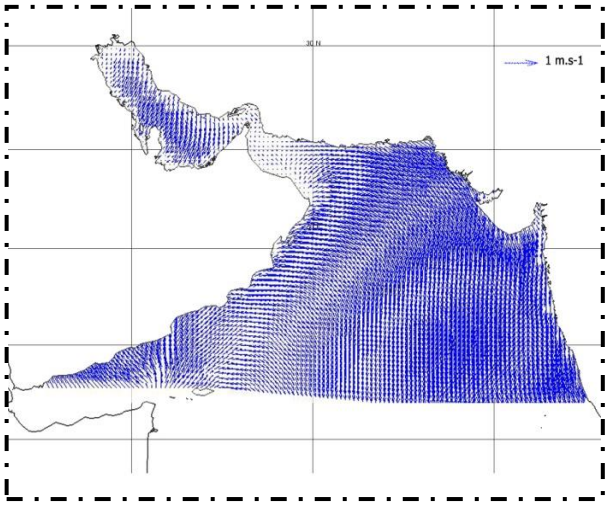

b)

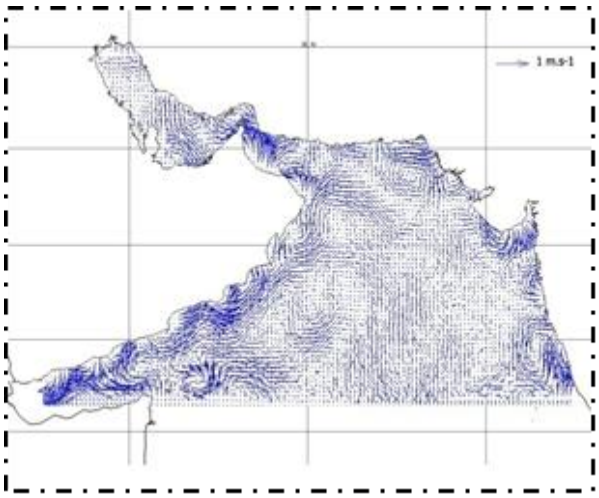

Fig. 4. a) Ekman current from 22 years wind stress data, b) Steady state currents form MDT_IAU_TN_2014 and Ekman currents.

OSCAR data is used to validate global coverage [19], which can be measured at 1 degree over time. Of course, only in the south of the study area does this data cover. OSCAR is a product of satellite data that shows marine surface currents in Ref. [20].

4.Conclusions

Among altimetry satellites used in this research, J2 and GFO satellites have ability to measure shallow water altimetry's. Hence, the data provided by these satellites in shallow waters, i.e. Persian Gulf are valuable. MHs differences between E1 and T/P are larger than the MHs of other satellites in comparison with the T/P, because there are differences between the two missions, i.e., there are 8 km distances between E1 sub-tracks at equator but long repeatability period of 35 days of data acquisition time and T/P sub-tracks spacing are 315 km at equator and short repeatability period of 9.9 days. Also, the orbit elevations are different: T/P at altitude of 1336 km and E1 at altitude of 785 km. Inclusion of E1 data in the MSS_IAU_TN_2014 solution would globally decrease the RMS difference of the solution relative to the MSS_CNES_CLS_2011 model from 0.4 m (without E1 data) to 0.1 m. This improvement by the E1 data is probably due to the higher resolution (8 km spacing) of the data in the region of interest. Changing the filtering radius of 1.386 degree down to lower degrees until 1 degree would increase the MDT_IAU_TN_2014 differences (relative to the MDT_DTU_2010) and MDT_CNES_CLS09 from 0.033m and 0.051m RMS up to larger values. At the 1.386 degree, the differences are at least. For filtering radiuses of more than 1.386 degree the MDT surface would become unreasonably much smoother and the RMS difference would increase.

Ekman currents were computed from 22 years of wind stress data. These currents are added to the MDT_IAU_TN_2014 geostrophic currents to come up with total currents. The total currents vary between 0 to 0.61 m/s in the region of interest. Using model MDT_DTU_2010 and applying equations 2 give the range of variations between 0 to 0.70 m/s. The currents from MDT_CNES_CLS09 model show variations between 0.001 to 0.62 m/s. The comparison shows that all three models show almost the same range of variations in the region of interest [21,22,23, 24]. As it is shown in Fig. 4 b), there are currents parallel to Oman coast with an average value of 0.7 m/s, as this is also confirmed by two other models. Some ocean gyres could be seen in Oman Sea in this model, which it could be seen in MDT_DTU_2010 and MDT_CNES_CLS09, too. The MDT_CNES_CLS09 would not show any currents in Persian Gulf but the MDT_IAU_TN_2014 would show very slow currents in this region. The fact that the MDT_IAU_TN_2014 would show Persian Gulf currents is because the J2 and GFO data in this region. Compared to OSCAR data with total currents of MDT_IAU_TN_2014 at 116 common points in 1 degree dimensions, in the east-west direction of RMS

the differences are 0.031 m / s and in the north-south direction of RMS the differences are 0.047 m / s.

Sea Level Anomaly (SLA) an In-Situ data could be used to make the MDT_IAU_TN_2014 independent from any other models. The lack of In-Situ data in the region of interest forced MDT_IAU_TN_2014 to use MDT_DTU_2010 to cover filtered parts. Also using other gravity models with higher Spherical harmonic coefficients degree and orders such as EIGEN-6c and EGM08 would make filtering not needed in the dynamic modeling.

5. References

[1] Knudsen, P., & Andersen, O.B. (2010). A global mean ocean circulation estimation using GOCE gravity models, The DTU12MDT mean dynamic topography model. Technical University of Denmark. DTU Space. Lyngby. Denmark.

[2] Rio. M.H, Guinehut, S. & Larnicol.G. (2011). New CNES-CLS09 global mean dynamic topography computed from the combination of GRACE data, altimetry, and in situ measurements. Journal of Geophysical Research. Vol 116. C07018 doi: 10.1029/2010JC006505

[3] Hernandez, F., & Schaeffer,P. (2001). The CLS01 Mean Sea Surface: A validation with the GSFC00.1 surface.

[4] Bingham, R., Haines, K. & Hughes, C. (2008). Calculating the Ocean's Mean Dynamic Topography from a Mean Sea Surface and a Geoid. Journal of Atmospheric and Oceanic Technology. 25(10): 1808-1822.

[5] Knudsen, P., Bingham, R. Andersen, O.B. Rio. M. (2011). A global mean dynamic topography and ocean circulation estimation using a preliminary GOCE gravity model. Journal of Geodesy. 85(11): 861-879.

[6] GUT User Guide and Algorithm Descriptions. (2011). ESA-GUT-AD-001

[7] Le Traon. P.Y.& Ogor, F. (1998). ERS-1/2 orbit improvement using TOPEX/POSEIDON: The 2 cm challenge. Journal of Geophysical Research. Vol. 103, No. C4, 8045-8057.

[8] RA/ATSR products - User Manual. (2001). Ref. C2-MUT-A-01-IFT, V2.3

[9] AVISO/Altimetry. (1996). AVISO/Altimetry for Merged TOPEX/POSEIDON products. AVI-NT-02-101. Edition 3.0

[10] AVISO and PODAAC user handbook. (2012). IGDR and GDR Jason Products. Edition 4.2

[11] OSTM/Jason-2 Products Handbook. (2001).

[12] GEOSAT Follow-On GDR User's Handbook. (2002).

[13] Vaníček. P & Krakiwsky, E.J. (1986). Geodesy: The Concepts, 2nd rev. ed. North-Holland. Amsterdam. 697 pages. translated into Chinese and Spanish. Reprinted in China and in Iran: 333- 334

[14] ESA SP-1233. (1999). Gravity Field and Steady-State Ocean Circulation Mission. The four Candidate Earth Explorer Core Missions.

[15] Pail. R, Bruinsma, S., Migliaccio, F. Foerste, C. Goiginger,H., Schuh, W.D., Hoeck,E. Reguzzoni, M., Brockmann,J.M, Abrikosov. O., Veicherts. M., Fecher. T., Mayrhofer, R., Krasbutter, I., Sanso, F., & Tscherning. C.C. (2011). First GOCE gravity field models derived by three different approaches. Journal of Geodesy. 85(11): 819-843.

[16] Pavlis. N, Holmes,S., Kenyon, S., & Factor,J. (2012). The development and evaluation of the Earth Gravitational Model 2008 (EGM2008). Journal of Geophysical Research. 117(B4).

[17] Förste, C., Shako,R., Flechtner,F., Dahle, C., Abrykosov, O., Neumayer,K.H.,Barthelmes, F., König, R., Bruinsma, S.L, Marty, J.C., Lemoine,J.M., Balmino,G., & Biancale,R .(2012). A new release for EIGEN-6 - the latest combined global gravity field model including LAGEOS, GRACE and GOCE data from the collaboration of GFZ Potsdam and GRGS Toulouse, (Geophysical Research Abstracts, Vol. 14, Abstract No. EGU2012-2821, 2012). General Assembly European Geosciences Union (Vienna, Austria).

[18] Stewart, R. (2008). Introduction to Physical Oceanography. Department of Oceanography Texas A & M University. Texas: 103-182

[19] Bonjean, F., & Lagerloef, G. (2002). Diagnostic Model and Analysis of the Surface Currents in the Tropical Pacific Ocean, Journal of Physical Oceanography02. 32(10): 2938-2954

[20] Agarvadekar Y., Amol,P., Aparna, S.G., Fernandes,R., Fernando,V., Gaonkar,M.G., Kankonkar,A., Khalap,S.T., Michael,G.S., Mukherjee,A., Satelkar,N.P., Shankar,D., Tari,A.P., & Vernekar, S.P. (2014). Observed intra seasonal and seasonal variability of the West India Coastal Current on the continental slope. Journal of Earth System Science. 123 (5). 1045-1074.

[21] Mehrfar, H, Torabi Azad, M., lari, K. & Bidokhti, A.A. (2020). A numerical simulation case study of the coastal currents and upwelling in the

western Persian Gulf, Journal of Ocean Engineering and Science, Vol 5. Issue 4, 323-332, doi.org/10.1016/j.joes.2019.12.005

[22] Mehrfar,H, Torabi Azad,M., lari,K. & Bidokhti, A.A. (2020). Seasonal variations of the coastal currents and eddies in the Persian Gulf; A Numerical case study, Marine Technology Society Journal, Vol 54, No 1, 44-52, doi.org/10.4031/MTSJ.54.1.4

[23] Sabetahd Jahromi, A., Raisi, A., Torabi Azad, M., & Mehrfar, H. (2017). Field study of changes of Geostrophic currents in the Persian Gulf, Journal of Marine Science and Technology, No. 87, Vol. 22, 37-31(In Persian)

[24] Ghazi, E., Bidokhti, A.A., Ezam, M., Zoljudi, M., Torabi Azad, M. (2019). Study of tidal currents and residual currents in the Persian Gulf, Hydrophysics Journal, Vol. 6, No. 2, 41-51(In Persian)

INTERNATIONAL JOURNAL OF
COASTAL, OFFSHORE & ENVIRONMENTAL ENGINEERING IJCOE Vol.9/No. 4/Autumn 2024 (64-72)

Available online at: www. Ijcoe.org

Prediction of Tidal Current Using FVCOM Hydrodynamic Model in Khuran Strait of Persian Gulf

Hassan Kazemi[1], Abbas Abedini[1*], Bahman Tajfirooz[2]

[1] School of Surveying and Geospatial Engineering, College of Engineering, University of Tehran, Tehran, Iran; aabedeni@ut.ac.ir , hassankazemi@ut.ac.ir*
[2] Darya Tarsim Consulting Engineer Co., Tehran, Iran; bahman.tajfirooz@gmail.com

ARTICLE INFO

Article History:
Received: 5 Feb 2024
Accepted: 16 Oct 2024

Keywords:
FVCOM model
Hydrodynamic
Tidal current
Current direction
Current speed

ABSTRACT

In recent years, the study of tidal currents has gained special importance due to economic, political, and environmental considerations, as well as its implications for maritime transport, navigational safety, and offshore structures. The Khuran Strait, located near the Strait of Hormuz in the Persian Gulf, is one of the most significant maritime areas. Thus, understanding tides, tidal currents, and their predictions is crucial in this region. We utilized the FVCOM model to simulate the speed and direction of tidal currents in the channel. The model's main inputs include the roughness coefficient, salinity, temperature, density, bathymetric data, and tidal information. Additionally, tidal time series were applied to the model using eight harmonic components. To evaluate the hydrodynamic model, we compared simulated current speeds and directions, as well as water levels, with observed data from specific locations. The results indicated a correlation of 75% for speed values and 89% for current direction. The RMSE values were 0.09 m/s for speed and 0.35 degrees for current direction. We used parameters such as RMSE and RV for statistical evaluation. Using the results of the FVCOM model, a Tidal Current Diamond prediction was presented.

1. Introduction

Ocean currents have always been significant for countries, particularly those near coastal areas or located in semi-closed basins. Most oil and gas resources, along with resource exploration, navigation, and power and communication transmission lines between the sea and coastal regions, are influenced by these currents. Additionally, ocean currents impact the geography of coastal areas. In the southern waters of Iran, there are thousands of aquatic species. Due to environmental factors, the presence of transmission and communication lines, as well as tourist resort projects, utilizing these vast resources necessitates the design of structures and infrastructure that can withstand these currents.The presence of major ports such as Shahid Bahonar, Shahid Rajae, and the Persian Gulf Shipyard Complex, along with Qeshm Island, Laft, and Khamir ports, contributes to the channel's importance for hydrodynamic studies. The area features a significant tidal range, with tides measuring approximately 3 meters on the northern coast of Qeshm Island and about 4.5 meters in other areas. Given the strategic and geographical conditions of this channel, it is recognized as a critical region for our country. Ocean currents are driven by various factors, including tidal forces, the gravitational pull of the moon and sun, wind, temperature differences, and thermohaline circulation [1]. This channel is located between the northern shore of Qeshm Island and the southern coasts, in Khuran Strait between 26°44° to 26°58°N latitude and 31°55° to 55°48°E longitude (As has been shown study area in Figure 1).

On the northern, eastern and southern boundaries of the area are located respectively: Pohl, Pir jazireh, Upper and Lower Tashtaqan, the city of Khamir, & old Laft, the port of Laft, Gawarzin & Khuran, Soheili, Tabl, Dorbani and Guran. Mangrove forest was first protected under the name of Mangrove Protected Area in 1972 with an area of 82360 hectares, then by increasing its area to 85686 hectares in 1975, considered as National Park. This area is now protected as Mangrove Protected Area under the management of the General Environment Department of Hormozgan Province.

Based on information obtained from three synoptic stations in Bandar-e Abbas, Bandar-e Lengeh, and Qeshm Island, the studied area exhibits a dry climate

according to De Martonne's climate classification, with an average annual temperature ranging from 25 to 27 degrees Celsius. Geologically, this area is part of the folded Zagros mountain range and has been tectonically influenced by the Arabian Plate throughout geological periods [2].

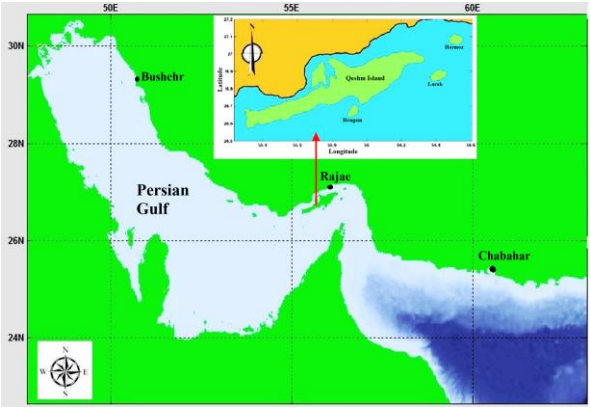

Figure 1. The location of Khuran channel in Persian Gulf

Several studies have focused on hydrodynamic modeling and the simulation of ocean water movement. Notable contributions include Chen, Liu [3], who developed an unstructured grid finite volume three-dimensional ocean model to study oceanic and coastal flows. Building on this, Wu and Tang [4] expanded high-resolution coastal ocean modeling (FVCOM) for Dartmouth Port, near Apponagansett Bay and Clarks Cove. Their series of experiments compared different modeling approaches to evaluate the impacts of sea level rise due to weather conditions, flow patterns, and wave distributions. These evaluations considered various dynamic forces, including wind direction and wave-current interactions. The results indicated that over a period of one hundred years, under easterly storm conditions, the rise in sea level caused by weather could significantly increase the potential flood areas by approximately 60% for each foot of sea level rise [3].

Cowles [5] significantly reduced the running time of the FVCOM model for the Gulf of Maine through parallel processing, leading to lower costs compared to previous years.

Wu and Tang [4] aimed to achieve accurate simulations of small-scale coastal ocean phenomena by integrating a computational fluid dynamics (CFD) model with the finite-volume coastal ocean model (FVCOM).

In the FVCOM model, current values are discretized using a triangulated grid for the horizontal planes and a separate grid for the vertical direction.

Using this method and convection equations, the horizontal speed in the vertical direction is determined, along with the water surface height and average values, which are directly influenced by the horizontal speeds. This process does not affect external forces. Additionally, these grids can optionally overlap, providing optimal flexibility in coupling different models.

To facilitate the coupling of the two models, we need grid nodes at the interface and utilize fixed elements, or intermediate nodes, within the FVCOM grid [4].

Sabatino and Thurlbeck [6] studied the modeling of sea surface waves in Clyde Bay, located in the southwest of Scotland. Water level fluctuations due to tsunami disturbances arising from changes in the climate system (such as very low or high pressure) can result in alterations in water levels. Positive changes can cause flooding, damaging coastal infrastructure and leading to casualties. To mitigate flood damage, they designed a warning system by developing a hydrodynamic model. They simulated water circulation in the Firth of Clyde and the North Channel using the FVCOM model developed by Chen, Liu [3] to simulate flow in estuary areas. Li and Chen [7] studied two major storm systems for flood risk in Massachusetts coast: tropical cyclones and catastrophic tropical cyclones. Coastal flooding occurs when wind-driven waves combine with high tides during storms. They established a northeast coastal ocean forecast system (NECOFS). By applying the FVCOM model to NECOFS, they investigated the impact of rising water levels due to climate change on coastal flooding caused by future hurricanes along the Massachusetts coast. This was evaluated by testing the model to forecast flooding in Boston Harbor and South End coastal areas under different sea level rise (SLR) scenarios over a century or under easterly storm conditions. The results indicated that with rising sea levels, the stability of the northeast coast of the United States will be highly vulnerable to hurricanes driven by wind. This finding is consistent with the observed increase in the intensity of surface waves caused by hurricanes over the last decade. The model also demonstrated that the responses of waves and surface currents to rising sea levels were completely non-linear. The effects of rising sea levels on coastal flooding caused by future hurricanes should be investigated using models that include wave-current interactions. Xu, Canals [8] studied Puerto Rico and the US Virgin Islands (PRVI) using the finite-volume community ocean model (FVCOM). Unlike traditional ocean models based on a grid, FVCOM is composed of staggered prismatic cells with triangular elements on the horizontal plane, providing a more accurate geometric representation of complex coastlines. Modeled sea surface temperature results were confirmed by observational data, showing a clear decrease in the Root Mean Square Error (RMSE). Statistical comparisons with Acoustic Doppler Current Profiler (ADCP) observations and moored current meters indicated significant improvements in ocean current modeling compared to the AMSEAS model, particularly at higher frequencies under strong tidal conditions, where the FVCOM model exhibited superior bathymetric resolution. Bairamzadeh, Siadat

Mousavi [9] employed the FVCOM model for hydrodynamic modeling of the Persian Gulf and the Sea of Oman to simulate current patterns for the first six months of 2013, demonstrating the model's effectiveness in these regions. Razzaghi, Haghshenas [10] designed a current forecast system for the Persian Gulf, and comparisons between flow simulation results and observational data further confirmed the model's success in simulating flow dynamics. Sadrinasab, Einali [11] studied the Arvandrud River plume, the primary source of fresh water entering the Persian Gulf, which holds significant military and environmental importance.

Shariatmadari, Siadat-Mousavi [12] studied renewable energy sources, primarily derived from solar energy, in response to the increasing reliance on non-renewable fuels and their detrimental effects on the survival of numerous species. Sohrabi Athar, Ardalan [13] aimed to develop a two-dimensional hydrodynamic tidal model for the Persian Gulf (PG2017) using 2D-MIKE21 software. They analyzed instantaneous changes in water levels while accounting for variations in the seabed friction coefficient and precise bathymetry, utilizing 23 years of satellite altimetry data. Their results indicated that the seabed friction coefficient significantly influences sea level changes in the Persian Gulf. Notably, the tidal behavior in the northern part of Qeshm Island differs from that of other regions in the Persian Gulf. To enhance the accuracy of the hydrodynamic tidal model, the Persian Gulf was divided into two areas, with the seabed friction coefficient modeled separately for each zone.

2. Theory of Problem

Some of the notable hydrodynamic flow models include MIKE21, ROMS, HYCOM, COHERENS, and PMODynamics [14], along with FVCOM. The FVCOM model is a open-source Finite-Volume Coastal Ocean Model, originally developed by researchers at Dartmouth University and the Woods Hole Oceanographic Institution. It is widely used by researchers around the world. Initially designed for simulating flooding and drying processes in estuarine dynamical systems, FVCOM has since been upgraded to accommodate a spherical coordinate system, making it suitable for both regional and global applications [15-21].

2.1. Governing equations

The governing equations of the FVCOM model in Cartesian coordinates, assuming the absence of snow and ice, include the following components: the equations for momentum, conservation of mass, temperature, salinity, and density, respectively [3]:

$$\frac{\partial u}{\partial t}+u\frac{\partial u}{\partial x}+v\frac{\partial u}{\partial y}+w\frac{\partial u}{\partial z}-fv= -\frac{1}{\rho_0}\frac{\partial(P_H+P_a)}{\partial x}-\frac{1}{\rho_0}\frac{\partial q}{\partial x}+\frac{\partial}{\partial z}\left(K_m\frac{\partial u}{\partial z}\right)+F_u \quad (1)$$

$$\frac{\partial v}{\partial t}+u\frac{\partial v}{\partial x}+v\frac{\partial v}{\partial y}+w\frac{\partial v}{\partial z}+fu= -\frac{1}{\rho_0}\frac{\partial(P_H+P_a)}{\partial y}-\frac{1}{\rho_0}\frac{\partial q}{\partial y}+\frac{\partial}{\partial z}\left(K_m\frac{\partial v}{\partial z}\right)+F_v \quad (2)$$

$$\frac{\partial w}{\partial t}+u\frac{\partial w}{\partial x}+v\frac{\partial w}{\partial y}+w\frac{\partial w}{\partial z}= -\frac{1}{\rho_0}\frac{\partial q}{\partial z}+\frac{\partial}{\partial z}\left(K_m\frac{\partial w}{\partial z}\right)+F_w \quad (3)$$

$$\frac{\partial u}{\partial x}+\frac{\partial v}{\partial y}+\frac{\partial w}{\partial z}=0 \quad (4)$$

$$\frac{\partial T}{\partial t}+u\frac{\partial T}{\partial x}+v\frac{\partial T}{\partial y}+w\frac{\partial T}{\partial z}=\frac{\partial}{\partial z}\left(K_h\frac{\partial T}{\partial z}\right)+F_T \quad (5)$$

$$\frac{\partial S}{\partial t}+u\frac{\partial S}{\partial x}+v\frac{\partial S}{\partial y}+w\frac{\partial S}{\partial z}=\frac{\partial}{\partial z}\left(K_h\frac{\partial S}{\partial z}\right)+F_s \quad (6)$$

$$\rho=\rho(T.S.P) \quad (7)$$

where the speed components x, y, and z are respectively the east, north, and vertical axis components in the Cartesian coordinate system. The $u, v,$ and w parameters are the $x, y,$ and z speed components. T, S, ρ, P_a, P_H, q respectively indicates temperature, salinity, density, sea-level pressure, hydrostatic pressure, non-hydrostatic pressure, and parameters $f, g,$ $K_m,$ K_h respectively, express the effect of Coriolis force, gravitational acceleration, the coefficient of vertical eddy viscosity and vertical eddy diffusion of temperature.

Coefficients $F_u,$ F_v represent horizontal momentum and F_T, F_S are coefficients of temperature and salinity. Total water depth $D = H + \zeta$, where H is the depth below the water surface (relative to $z = 0$) and ζ is the instantaneous water surface height (relative to $z = 0$). $P = Pa + P_H + q$ is the total pressure at which P_H the hydrostatic pressure obtained. C_d, the drag coefficient of a logarithmic lower layer with z_{ab} of the model is determined at a height higher than the lower layer [3]:

$$C_d = max\left(k^2/\ln\left(\frac{z_{ab}}{z_0}\right)^2, 0.0025\right) \quad (8)$$

where $k = 0.4$ is Von Karman's constant and z_0 is the bottom roughness parameter.

2.2. Sigma coordinate system equations

Due to the variability of water depth across different oceanic regions, particularly near coastal areas and channels, simulating ocean parameters can be challenging. Traditional ocean models utilize a Z-coordinate system in which depth is uniform and rectangular across various areas. However, the influence of water turbulence and mixing in shallow waters cannot be overlooked. Therefore, for more accurate forecasting, it is preferable to use a vertical coordinate system that accounts for different layers with equal distances and fully accommodates the

topography of the seabed. This vertical coordinate system, known as sigma, is employed by the FVCOM hydrodynamic model. In this context, ĝ=ĝ(x,y,r,t) represents a generalized Earth coordinate system where x and y denote the east and north axes, respectively, and r is the vertical axis, ranging from -1 to 0. The variable r can be defined as a sigma, composite, or more generalized function [22].

The hydrodynamic model employs s-coordinates in deep water and σ-coordinates in shallow water to resolve the equations. Since the Khuran channel is located in a shallow water region, the model utilizes the σ-coordinate system.

2.3. Time step determination

The sea level height describes fast-moving long surface gravity waves. In the explicit numerical method, the time step selection criterion is inversely proportional to the phase speed of the waves, represented as ($\sqrt{gd}$).

Since the sea level height is proportional to the water transport gradient, it can be calculated using vertically integrated equations. Subsequently, the three-dimensional equations can be solved with a specified sea level height. In this numerical method, known as "mode splitting," the currents are divided into external and internal currents, which can be calculated using two separate time steps. This method is also successfully implemented in models such as POM1 and ROMS2.

3. Experimental investigations

3.1. Input data

There are two common current measurement methods including Eulerian and Lagrangian approaches. The point Acoustic Current Meter, RCM9, employs the Eulerian method for current measurement. One of the input data sets for the FVCOM hydrodynamic model is the bathymetric data obtained from hydrographic operations in the Khuran Strait. These bathymetric data, collected using a single beam echo sounder, were gridded using Surface Water Modelling System (SMS) software.As an integrated grid on the horizontal surface of the fluid, tidal components at open border points on both sides of the Khuran channel were extracted as a time series using the Tidal Model Driver (TMD) tidal model. This extraction ensured that the required inputs could be formatted according to the specifications in the FVCOM user manual. Additional data, such as depth, salinity, density, and temperature, were also introduced to the model, considering the physics of the sea. The program was then run in a Linux environment. Finally, using MATLAB and other software, we processed the resulting data from the output file and compared and analyzed it with direct observations obtained from the RCM9 current meter installed near Shahid Rajae Port.

3.2. Mesh grid

The SMS software, within the Aqua module, was used to produce bathymetry grinding taken in the Quran Strait. Following the standards of the International Hydrographic Organization (IHO), these measurements were conducted using a single-beam system to create bathymetric charts. Node spacing was designated based on proximity to the coastline as follows: 100 meters near coastlines, 200 meters in central grid points, and 400 meters in distant regions. The model's bathymetry is illustrated in Figure 2. A large grid comprising 50,161 node points fully covered the study area, with region-specific spacing for enhanced accuracy. A finer mesh was applied along closed (dry) boundaries where the coastline's shape and complexity increased, whereas larger cells in central regions were used to enhance grid conformity to the coastline. Coastal boundary points were derived from field surveys (as shown in Figure 3).

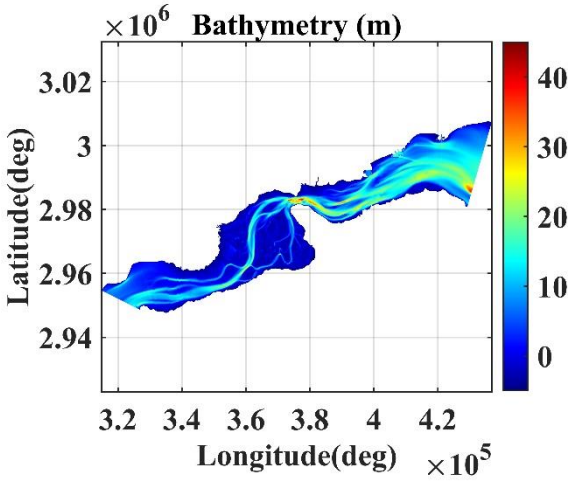

Figure 2. Bathymetric map of the Khuran Channel

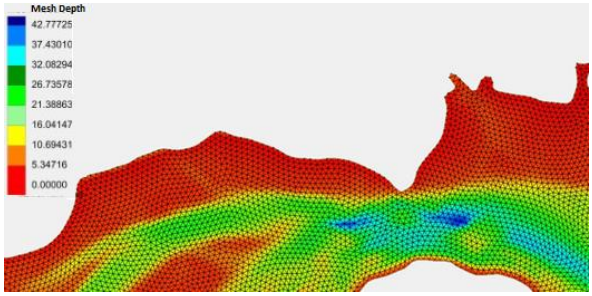

Figure 3. Mesh grid of case study derived by FVCOM model

3.3. Boundary conditions, open and closed boundaries

The Khuran channel, situated between Qeshm Island to the south and the mainland coastline to the north, was represented in the model with closed land boundaries on the northern and southern sides and open boundaries on the eastern and western sides. The TMD, a MATLAB code, was utilized to access

[1] Princeton Ocean Model
[2]Regional Ocean Modelling System

harmonic tidal model components essential for predicting tidal heights and currents. The model incorporated eight tidal components (M_2, S_2, K_2, N_2, K_1, P_1, O_1, and Q_2) based on latitude and longitude coordinates.

To run the FVCOM program, 85 open boundary points were introduced, and tidal time series data generated from TMD tidal model components were processed in parallel on a Linux environment. The output file, saved in NetCDF (NC) format, was subsequently analyzed using MATLAB to extract parameters such as instantaneous water level height, amplitude, phase, current speed, and direction. These values were computed across 98,282 elements and 50,161 nodes at seven sigma levels, with a focus on the middle layer of the third sigma level. Data outputs—documented in Julian day, UTC local time, speed (in meters per second), and direction (in degrees)—were obtained from the FVCOM hydrodynamic model. The accuracy of this data was validated against observations from Shahid Rajaee station using statistical methods including Root Mean Square Error (RMSE), Q-Q plots, and scatter plots.

For sensitivity calibration, the model was initially run with varying roughness values, eventually identifying an optimal roughness value of 0.0066 based on a comparison of estimated results. Calibration was conducted at a temperature of 23°C and a salinity of 36.5, with calculations performed in 10-minute time steps. The model used a sigma coordinate system to divide the water column into seven levels, with a middle layer flanked by three levels above and three levels below, thus forming a 7-sigma level structure.

Tidal currents in this model are influenced by factors such as temperature, salinity, wind, seabed topography, and water depth, resulting in complex and dynamic coastal water movement patterns. These factors significantly impact coastal climate, sediment transport, organic and chemical substance distribution, environmental health, marine transportation, fisheries, marine energy generation, coastal structures, and infrastructure, including oil installations and pipelines. Tidal component data were integrated into the model as a continuous time series applied to open boundary points on both the eastern and western sides of the study area, spanning from the Bandar Abbas old port to the Bahman port in the east, and from Hameyran to Basaidu in the west. Tidal current observations at the Shahid Rajaee and Pohl stations include three main data columns: time, current speed, and direction, with a sampling rate of 10 minutes. These datasets, prepared by Darya Tarsim Consulting Engineers Company, were collected at a sampling rate of ten minutes over a three-month period as shown in Table 1.

Table 1. Stations of tidal current observation

Station	φ	λ	period of observation	year	Sample rate (minutes)
Shahid Rajae	27.11	56.06	3 months	2009	10
Pohl	26.96	55.37	3 months	2009-2010	10

The model's simulated results were then compared with direct measurements from the Shahid Rajaee and Pohl stations, and the findings are summarized as follows.

3.4. Sensitivity analysis

Accurate calibration of the hydrodynamic model requires an effective bed roughness parameter, as bed roughness introduces friction that affects bed shear stress, resulting in resistance and delay in current flow. This parameter is quantified by the drag coefficient, which impacts the amplitude and phase of the tidal model's harmonic components. In the Khuran area, no direct measurements of bed roughness have been conducted to date.

Bed roughness represents resistance to flow and includes the shear stress exerted by the seabed. This parameter depends on the seabed's relief and particle size (e.g., sand, clay, and sediments). Although the seabed is dynamic, bed roughness is assumed to remain constant over time, as average changes in seabed shape are considered stable.

To assess model sensitivity, we ran the hydrodynamic model with Manning values of 0.0037, 0.0044, 0.0066, and 0.0088 over three-day intervals from October to January, a period capturing the highest variability. A Manning value of 0.0066 was identified as the optimal bed roughness coefficient, as it minimized the difference between model outputs and tidal observations.

3.5. Statistical reliability and model validity

The model's accuracy is assessed by comparing its results with those from other studies, using statistical methods to evaluate reliability and validity while accounting for variance. Statistical metrics, including Root Mean Square Error (RMSE), Relative Variance (RV), and the Coefficient of Determination (R^2), are applied to evaluate the model's performance, as defined by the following mathematical equations.

The RMSE equation is as follow:

$$RMSE = \sqrt{\frac{[h_t - h(t)]^2}{N}} \tag{9}$$

In the RMSE equation, $h(t)$ is the predicted value and h_t is observed values and N is the number of observations. The closer the answer is to zero, the better the accuracy of the model.

RV is the reduction of variance that expresses the ratio of the variance of the predicted values to the variance of the observed values according to the following equation:

$$RV = \frac{\sum[h(t) - h_0]^2}{\sum\ [h_t - h_0]^2} \quad (10)$$

where h_0 is the average value of observations and h_t is the value of observation, and $h(t)$ is the predicted values. If RV is equal to one, it indicates the agreement of observations and predictions. The Coefficient of Determination (R-squared or R^2) is as follow:

$$R^2 = 1 - \frac{\sum\left(h_t - h(t)\right)^2}{\sum(h_t - h_0)^2} \quad (11)$$

3.6. Current speed

The statistical evaluation of the FVCOM hydrodynamic model for current speed at the Port of Shahid Rajaee showed strong agreement between observed and predicted values. The Root Mean Square Error (RMSE) was 0.095 m/s, and the Relative Variance (RV) was 1.078, indicating high accuracy. Moreover, the Coefficient of Determination (R^2) of 0.756 confirmed a strong correlation between model results and observations, further validating the model's reliability in predicting tidal current speed. If the bed roughness parameter had not been optimized and calibrated, the model could have overestimated or underestimated flow velocities. However, as expected, this did not occur in our modeling study.

Figure 4 presents a comparison between observed current speed data and FVCOM hydrodynamic model results, sampled at 10-minute intervals. A moving average filter was applied to the observed data to reduce random noise. The strong agreement between the simulated and observed data, as shown in the figure, demonstrates the ability of the model to simulate the flow velocity.

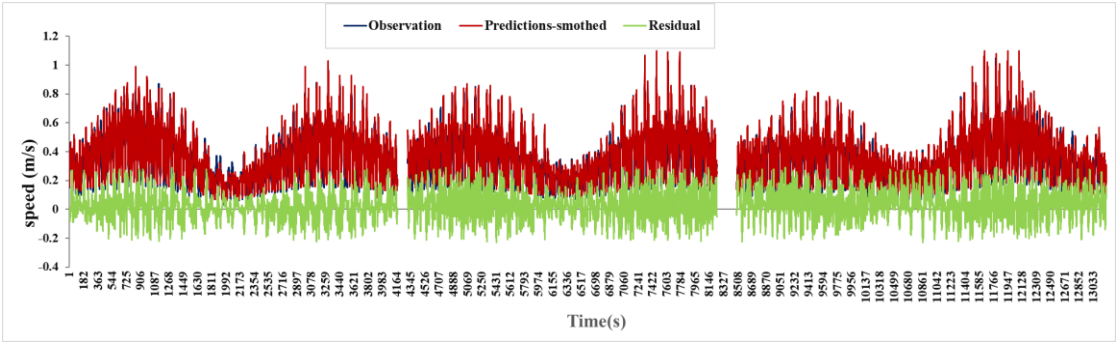

Figure 4. Comparison of the speed values of the measured observations with the results obtained of the model

Tidal flow simulations were conducted for Shahid Rajae station, where current meter observations were collected at 10-minute intervals over a three-month period, encompassing both low and high tide cycles. For a more detailed analysis, Figures 5a and 5b show a scatter plot comparing observed and predicted current speed and direction at the station.

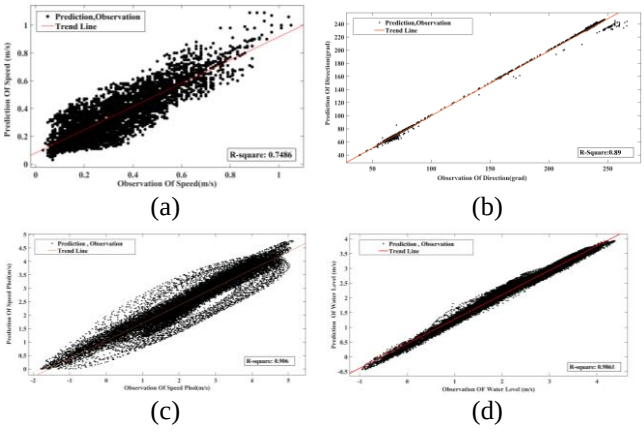

Figure 5. Scatter plots: (a) comparison of predicted and observed speeds in Rajae port (b) predicted vs observed for current directions in Rajae port (c) comparison of predicted and observed of current speeds in Pohl port (d) water level of Shahid Rajae port observed vs. predicted

The data presented indicates that the observations and predictions from the FVCOM model at Shahid Rajae port station demonstrate a strong correlation between model data and actual observations, with negligible residual values.

The Q-Q plot in Figure 6a indicates a good agreement between the model-predicted and observed data, with a high density of points along the diagonal line. While there are some deviations in the initial and final values, these discrepancies are relatively small compared to the overall dataset.

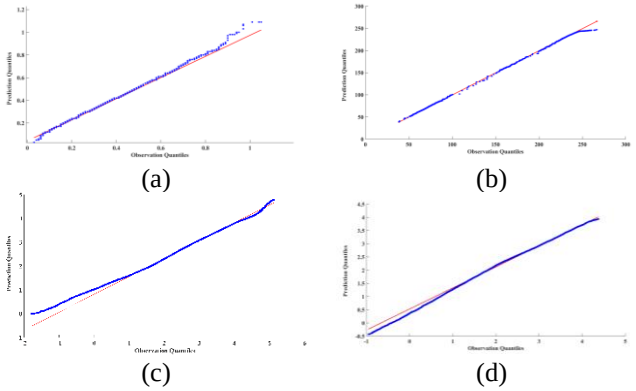

Figure 6. Q-Q plots: (a) for comparison of predicted and observed speeds in Rajae port, (b) comparison of predicted and observed directions in Rajae port, (c)

comparison of predicted and observed current speeds in Pohl port, (d) water level of Shahid Rajae port observed vs. predicted

3.7. Current direction

The model-predicted flow directions, expressed in degrees, align well with the observed directions at Shahid Rajae station. The relatively low values of Relative Variance (RV = 1.02) and Root Mean Square Error (RMSE = 0.8417 m/s) indicate a strong correlation between observed and predicted speed values, with a correlation coefficient of 89%.

Instances of rapid changes in direction, which can lead to high-angle rotations, were excluded from the analysis. The statistical metrics and visual comparisons (Figure 7) demonstrate excellent agreement between the model-predicted and observed directions at Shahid Rajae port.

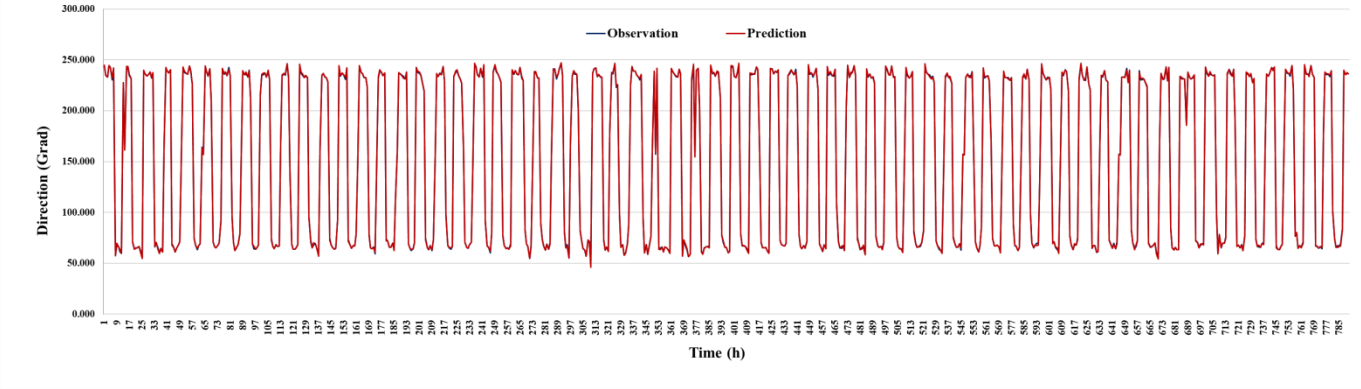

Figure 7. Agreement of the observations of the predicted and observed directions

3.8. Water level

Using the output of the information obtained from the FVCOM hydrodynamic model, the water level has been shown in Figure 8.

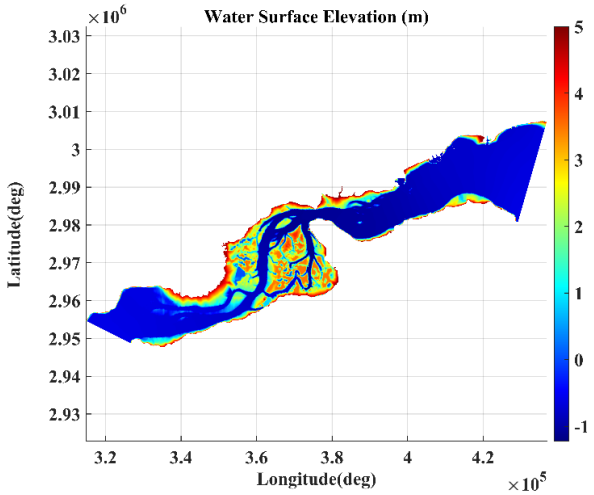

Figure 8. Water level plot in the Khuran Channel area

The model simulations were conducted using a roughness coefficient of 0.0066 and a vertical discretization of 7 sigma levels. To further validate the model's performance, additional simulations were carried out for the Port of Pohl station.

Comparisons of simulated and observed water levels at both the Port of Pohl and Shahid Rajae stations demonstrate excellent agreement (Figures 9a and 9b).

The statistical results of this modelling for water level prediction are shown in the table 2. below.

Table 2. Comparison of the values of the analysis accuracy indices

Station	RMSE (m/s)	RV	R^2	Sample rate(minutes)
Shahid Rajae	0.22	1.22	0.89	10
pohl	0.58	1.11	0.75	10

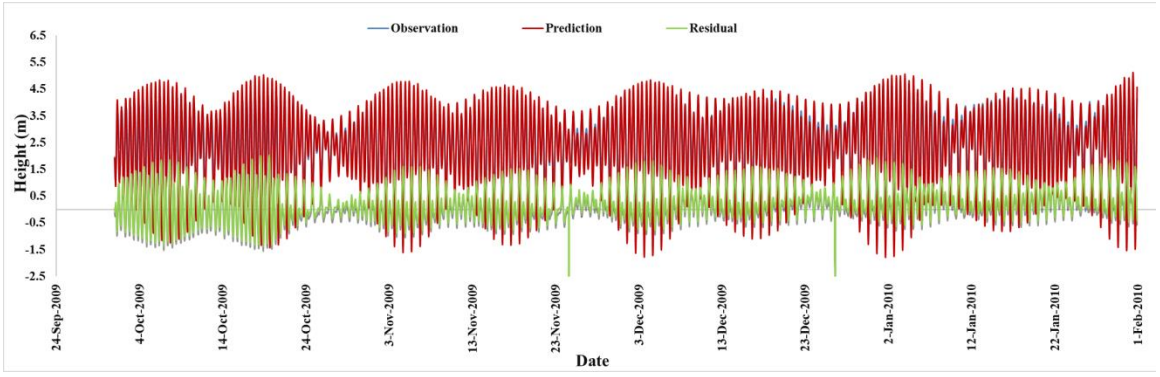

(a)

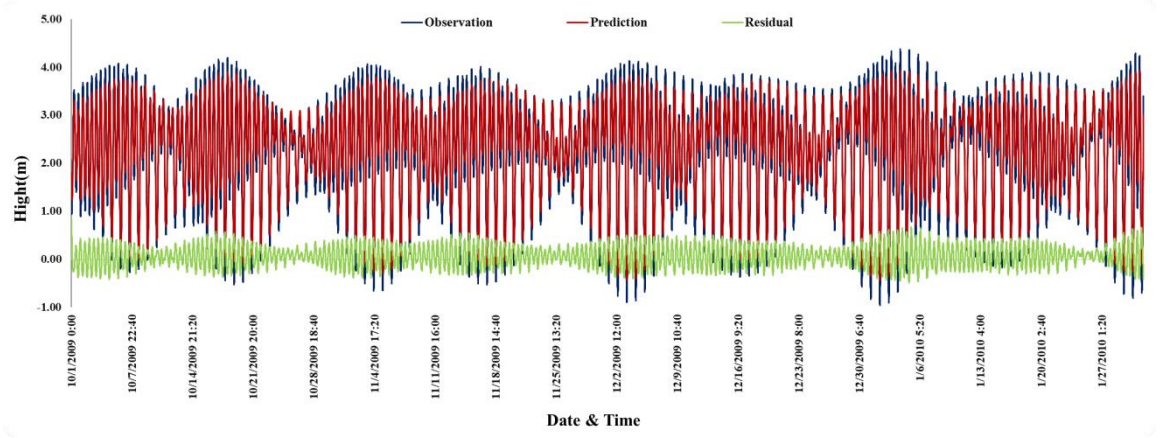

(b)

Figure 9. Comparison of height observations the water level: (a) in Port of Pohl vs the model results, (b) in Port of Shahid Rajae vs model results

3.9. Tidal Current Diamond

One of the goals of simulating the speed and flow in Khuran is to produce a tidal current diamond tables that can be inserted in nautical charts. Tidal Current Diamonds are symbols on British and international nautical charts that indicate the direction and speed of tidal currents relative to High Water times as specified in the Admiralty Tide Tables.

These tables are typically found on nautical charts and consist of a grid with 13 rows and 3 columns for each diamond. The first column indicates the time relative to High Water, ranging from 6 hours before to 6 hours after. The remaining columns provide the mean direction and speed of tidal currents during spring and neap tides at specific locations. While Tidal Current Diamonds provide valuable information, Tidal Atlases, when available, often offer more accurate and user-friendly representations of tidal currents.

Table 3 compares the values of the speeds and directions of the simulated tidal current with the values published in the Iranian navigation chart of Khuran region.

4. Conclusions

FVCOM hydrodynamic model was utilized in the Khuran Channel of the Persian Gulf to simulate tidal currents and water levels.The model's performance was evaluated by comparing simulated and observed data for current speed, direction, and water level.

The results indicate a strong agreement between simulated and observed values. The model accurately captured the spatial and temporal variability of tidal currents, with a Root Mean Square Error (RMSE) of 0.095 m/s for current speed and a high correlation coefficient (R^2) between observed and predicted values.

The Q-Q plots further confirmed the good agreement between simulated and observed distributions.

The sensitivity analysis revealed that the model's performance is influenced by the bed roughness coefficient. However, with appropriate calibration, the model can provide reliable predictions. Overall, the FVCOM hydrodynamic model demonstrated its ability to accurately simulate tidal hydrodynamics in the study area, providing valuable insights for coastal engineering and environmental management.

Table 3. Tidal Current Diamond around Shahid Rajaee port

TIDAL STTREM	DIR.(DEG.)	RATE (KNOT)		DIR.(DEG.) FVCOM MODEL	RATE (KNOT) FVCOM MODEL	
		SPRING	NEAP		SPRING	NEAP
6hours before H.W	75	0.7	0.3	60	0.4	0.2
5hours before H.W	45	0.3	0.1	29	0.6	0.3
4hours before H.W	300	0.5	0.2	304	0.6	0.5
3hours before H.W	263	1.0	0.5	265	1.0	0.6
2hours before H.W	250	1.5	0.7	257	1.4	0.4
1hours before H.W	246	1.2	0.6	249	1.1	0.2
H.W	247	0.7	0.3	247	0.7	0.3
1hours after H.W	342	0.2	0.1	243	0.5	0.4
2hours after H.W	65	0.3	0.1	231	0.7	0.5
3hours after H.W	89	0.7	0.3	75	0.7	0.5
4hours after H.W	70	1.1	0.5	60	1.2	0.5
5hours after H.W	79	1.3	0.6	60	1.1	0.4
6hours after H.W	76	1.0	0.5	67	0.7	0.3

From the results of the model, we were able to extract a prediction of the necessary tidal current speeds and directions in the form of a Tidal Current Diamond for inclusion in navigational charts.

Acknowledgment

The authors are thankful to Geospatial-based Hydrologic Laboratory (School of Surveying and Geospatial Engineering, College of Engineering, University of Tehran) for supporting this research.

8. References

1. Foreman, M.G.G., *Manual for tidal heights analysis and prediction*. 1977: Institute of Ocean Sciences, Patricia Bay.
2. ZANGANEH, A.M., M.E. TAGHAVI, and E. AKBARI, *Evaluation and assessment of changes in forest area Harra (mangrove) Using remote sensing techniques Case Study: Bandar Abbas.* 2017.
3. Chen, C., H. Liu, and R.C. Beardsley, *An unstructured grid, finite-volume, three-dimensional, primitive equations ocean model: application to coastal ocean and estuaries.* Journal of atmospheric and oceanic technology, 2003. **20**(1): p. 159-186.
4. Wu, X.-g. and H.-s. Tang, *Coupling of CFD model and FVCOM to predict small-scale coastal flows.* Journal of Hydrodynamics, Ser. B, 2010. **22**(5): p. 284-289.
5. Cowles, G.W., *Parallelization of the FVCOM coastal ocean model.* The International Journal of High Performance Computing Applications, 2008. **22**(2): p. 177-193.
6. Sabatino, A.D. and I. Thurlbeck, *FVCOM Clyde Sea Hydrodynamic Model User Guide and Technical Report.* 2016.
7. Li, S. and C. Chen, *Air-sea interaction processes during hurricane Sandy: Coupled WRF-FVCOM model simulations.* Progress in Oceanography, 2022. **206**: p. 102855.
8. Xu, H., M. Canals, and A. Rivera. *High Resolution Modeling of Coastal Circulation Using FVCOM in Puerto Rico and the US Virgin Islands*. in *OCEANS 2022-Chennai*. 2022. IEEE.
9. Bairamzadeh, M., S.M. Siadat Mousavi, and M. Majidi, *Modeling the current pattern of Persian Gulf and Sea of Oman using FVCOM model*, in *16 th Iranian Hydraulics Conference papers*. 2018: Ardabil, Iran.
10. Razzaghi, S., et al., *3D Numerical Modelling of Shallow and Deep Water Currents in the Persian Gulf.* Iranian Journal of Geophysics, 2019. **13**(3): p. 69-85.
11. Sadrinasab, M., et al., *Numerical Modelling of Arvandrud River Plume and the impact of wind and River Discharge on the plume structure By Three Dimensional and Hydro dynamical Model (FVCOM).* Journal of Marine Science and Technology, 2021. **20**(3): p. 12-30.
12. Shariatmadari, D., M. Siadat-Mousavi, and C. Ershadi, *Evaluation of extractable energy from tidal farm in the Qeshm canal using numerical flow simulation.* Journal of Oceanography, 2021. **12**(46): p. 1-12.
13. Sohrabi Athar, M., A.A. Ardalan, and R. Karimi, *Hydrodynamic tidal model of the Persian Gulf based on spatially variable bed friction coefficient.* Marine Geodesy, 2019. **42**(1): p. 25-45.
14. Bakhtiari, A., et al., *An Investigation on PMO Dynamic Model in Bushehr Bay, Persian Gulf, Iran.* Journal of Oceanography, 2013. **4**(14): p. 13-18.
15. Chen, C., R. Beardsley, and G. Cowles, *An unstructured grid, finite-volume coastal ocean model (FVCOM) system.* Oceanography, 2006. **19**(1): p. 78-89.
16. Darya Tarsim Company, D.B.T.F. 2023.
17. DHI, *MIKE 21 Toolbox - Global Tide Model – Tidal prediction*.
18. Fossette, S., et al., *A biologist's guide to assessing ocean currents: a review.* Marine Ecology Progress Series, 2012. **457**: p. 285-301.
19. John, B., et al., *COHERENS: a hydrodynamic model validated for the west coast of India.* Current Science, 2015: p. 288-300.
20. Lyard, F.H., et al., *FES2014 global ocean tide atlas: design and performance.* Ocean Science, 2021. **17**(3): p. 615-649.
21. Shchepetkin, A.F. and J.C. McWilliams, *The regional oceanic modeling system (ROMS): a split-explicit, free-surface, topography-following-coordinate oceanic model.* Ocean modelling, 2005. **9**(4): p. 347-404.
22. Chen, C., et al., *An unstructured-grid, finite-volume community ocean model: FVCOM user manual*. 2012: Sea Grant College Program, Massachusetts Institute of Technology Cambridge ….